Wide Band-Gap Metamaterials as Seismic Shields

A Dissertation

By

Ashraf Mohammed Daradkeh

Submitted to the Graduate School of
The University of Texas at Arlington in partial fulfillment
of the requirements for the degree of

DOCTOR OF PHILOSOPHY

The University of Texas at Arlington
August 2023

UNIVERSITY OF
TEXAS
ARLINGTON

ACKNOWLEDGMENTS

I want to acknowledge and give my sincere gratitude to my supervisor, Dr. Himan Hojat Jalali, who made this work possible. His guidance, support, and advice carried me through all phases of my research. I thank my doctoral committee members, Dr. Shih-Ho Chao, Dr. Juan Balderrama, and Dr. Amir Ameri, for their time, guidance, and supportive suggestions.

Without my family, I would be nowhere, so I thank my loving wife, Dr. Salar Bani-Hani, for her unconditional love, support, and motivation throughout my studies, my two lovely daughters, Emma and Lara, for the cries, candies, and spirit they add to the family.

Finally, I am grateful to my father, Mohammed, Mother, Afaf, and Brothers Eng. Anas, Eng. Adham, Dr. Abdullah, and sisters Dr. Ashjan and Dr. Eman for their endless love, encouragement, and support.

August 15, 2023

ABSTRACT

Wide Band-Gap Metamaterials as Seismic Shields

Ashraf Mohammed Daradkeh, Ph.D.

The University of Texas at Arlington, 2023

Supervising Professor: Himan Hojat Jalali

In the past decade, a new paradigm has gained popularity among researchers aiming to protect structures from low-frequency seismic vibrations using metamaterials. However, developing a workable design for metamaterials is still challenging, given the various factors such as material availability, size, and shape of its components. This dissertation proposes a new configuration that can widen the attenuation frequency of metamaterials and evaluates the attenuation capability of graded metamaterials. The project investigates unit cell parameters such as but not limited to size, density, and modulus of elasticity to finalize a unit cell with the broadest possible bandgap by using common construction material such as concrete, steel, carbon fiber reinforced polymer (CFRP), and rubber. Moreover, the project investigates multi-layered unit cells with two, three, and four-layered metamaterials and evaluates its effects on the bandgap limits.

Furthermore, to broaden the bandgap a double-graded configuration is proposed and evaluated by modeling the real-world application of metamaterial, with unit cells periodically embedded in soil medium and subjected to low-harmonic amplitude with low-frequency waves. The evaluation included both surface and body waves. Moreover, the performance of the proposed configuration is evaluated for a Single Degrees of Freedom Structure (SDOF) by investigating the peak amplitude of the responses. Finally, the performance of the proposed double-graded metabarriers was assessed in the time domain, in which the configuration is subjected to two artificial wavelets, i.e., Ormsby and Ricker, and a time history record of the 1975 Oroville dam earthquake, California 1940 (PEER, accessed 2023). Moreover, a new double-graded configuration is presented to help reduce the SDOF peak frequency amplification. The result shows that a 4.5-15.3 Hz bandgap can be achieved using a 2 m two-layered unit cell made of rubber matrix and steel core.

Moreover, the upper bound of the attenuation zone can be increased up to 29 Hz by using the proposed configuration (double-graded configuration), and the lower bound can be decreased to 3.5 Hz, where the double-graded meta-barriers can block 88% of the most destructive seismic frequencies. Furthermore, the double-graded configuration is shown to reduce the amplification of SDOF at the peak frequency, which is not located in the attenuation zone of the unit cell. Finally, the configuration is evaluated using a triangle-like double-graded design with fewer unit cells and more wave absorption. Results of the time domain show great match with the dynamic response results and the proposed design can absorb most of the applied waves. Moreover, the triangular-like design showed that it’s capable of diverting the wave direction towards the ground rather than reflecting it to the surroundings of the protected structure.

DISSERTATION ORGANIZATION

The topic of this dissertation is covered in five chapters: chapter 1 presents an overview of seismic hazards, types of seismic waves, and traditional seismic protection methods in addition to the objectives and gaps to be covered in this topic. Chapter 2 presents a summary of the literature progress in the field of seismic protection using metamaterials. Chapter 3 introduces the theory behind seismic metamaterial and the numerical evaluation of metamaterial unit cells. Moreover, a simplified mass-spring model is presented in chapter 3 that simplifies the methodology of finding the attenuation zone. Additionally, the method of evaluating a metamaterial unit cell and the bandgap verification process is presented in chapter 3 as well, including the frequency response (Frequency domain) and time domain analyses. Finally, the parametric study plan is also presented in this chapter. Chapter 4 discusses the results of the parametric studies explained in chapter 3 and investigates their relation to the bandgap. Moreover, the verification results and the development of wide-bandgap seismic shields are presented in chapter 4, as well as an evaluation of the performance of double-graded configuration in frequency and time domains and their effects on the structure peak responses. Finally, chapter 5 contains a summary and concludes the dissertation.

TABLE OF CONTENTS

LIST OF FIGURES

LIST OF TABLES

ACRONYMS AND ABBREVIATIONS

λ	Wavelength
λ_s	Shortest wavelength
3D-3C	3-dimensional 3-axis periodicity unit cell
A	Amplitude
BGW	Bandgap width
CFRP	Carbon fiber reinforced polymer
DGA	Double graded array
DGP	Double graded pyramid
f	Frequency
FIBZ	First Irreducible Brillouin Zone
FRF	Frequency response function
LCFBG	Linear chirped configuration
LBGL	lower bandgap limit
LBR	low-reflecting boundaries
PML	perfectly matched layers
PBC	Periodic boundary conditions
RMS	square root of the mean of squares
SDOF	Single degree of freedom
T	Period
TMD	Tuned mass damper
TMDI	Tuned mass damper with inerter
UBGL	Upper bandgap limit
V	Velocity

CHAPTER 1 : INTRODUCTION TO SEISMIC METAMATERIALS

This chapter presents an overview of seismic hazards, the most destructive waves, types of seismic waves, characteristics of waves, and traditional seismic resistance methods. Additionally, it introduces seismic metamaterials, presents the problem statement, and goals and objectives of this research.

1.1. Introduction to Earthquakes

Earthquakes are one of the most disastrous natural hazards due to damages they cause to structures, infrastructure, and due to loss of lives. A recent earthquake that hit south Turkey-north Syria caused a humanitarian disaster; more than 41,000 lives were lost, other than the economic impact on the region (worldvision.org). According to the US geological survey, the world's deadliest earthquake occurred in China in 1976 and caused 830,000 casualties. Earthquake side-damages, such as but not limited to fires, can cause more harm than the earthquake itself. Earthquakes occur due to sudden slip on a fault. The tectonic plates are connected by friction and are always moving. However, when the stress on the connected edge exceeds the friction, slippage occurs, and the energy is released as seismic waves. The waves travel through the earth's crust into the surface, causing all the vibrations and damage we feel.

The most disastrous wave frequencies fall within 0-30 Hz, where 0-20 Hz are seismic wave frequencies, and 20-30 Hz are transportation-induced frequencies. Figures 1-1, 1-2, and 1-3 show multiple types of destructive waves from different sources, such as earthquakes, transportation-induced waves, and explosions (0-100 kHz, Yang et al., 2018), respectively.

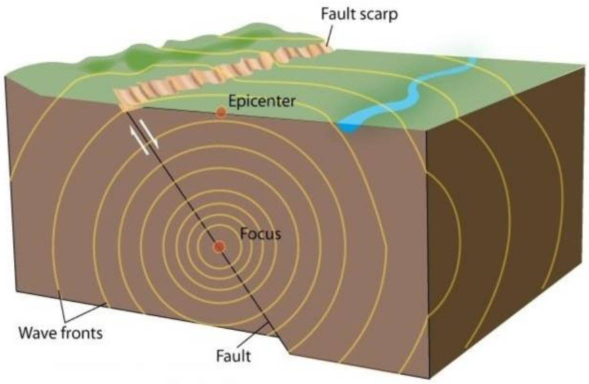

Figure 1-1: Earthquake waves (University of Waikato, accessed 2023).

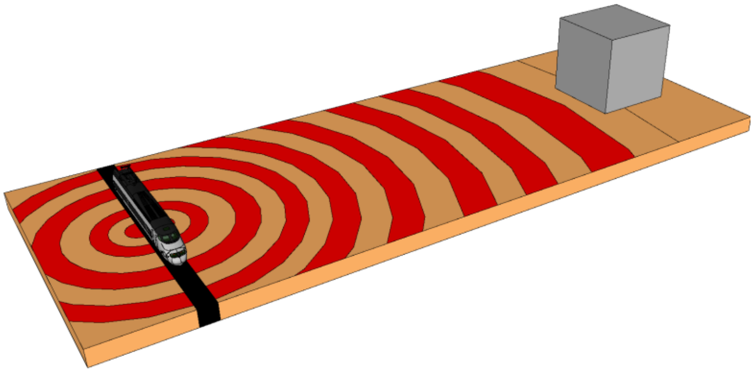

Figure 1-2: Transportation-induced waves.

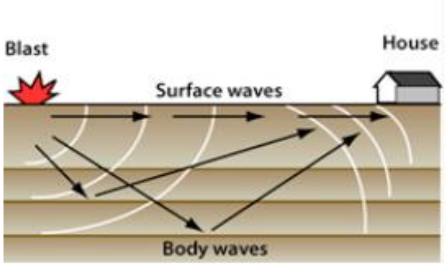

Figure 1-3: Explosion waves (explosives.org, accessed 2023).

1.2. Types and Characteristics of Seismic Waves

Earthquakes generally release energy in the form of waves, i.e., seismic waves. There are two types of movement with each seismic wave: propagation and oscillation directions. While all wave types can propagate in any direction, they can oscillate in one direction only, leading to earth particle movement, which is used to recognize the kind of waves. There are two main types of seismic waves: body and surface waves (Chong and Lee, 2021). By definition, body waves occur in the earth's body and are reflected, diverted, and transmitted through various earth layers where density and seismic wave velocity change.

Furthermore, body waves can be divided into P and S waves. Each type can be recognized by the earth's particle movement (oscillation direction). P-waves (Primary or pressure waves) are longitudinal waves that compress earth particles during propagation. P-waves are the fastest waves, and they appear first on seismograms. S-waves (Secondary or shear waves) are transverse waves, as they propagate the earth particles oscillating perpendicular to the propagation direction. They are slower than P-waves.

Surface waves, on the other hand, occur along and near the earth's surface. They cannot travel in the earth's body and are usually generated by shallow earthquakes. Surface waves are slower than body waves and have higher amplitude and longer duration than body waves. They can be divided into two types: Rayleigh waves, in which the oscillation direction is elliptical, the movement of the particles is greatest at the surface and decrease as the depth increases. The speed of Rayleigh waves is related to their wavelength. The second surface wave type is Love waves, where the oscillation direction parallels the earth's surface. Figures 1-4 and 1-5 show body and surface wave types, respectively.

Figures 1-4 and 1-5 show that all waves propagate in the same direction. However, each wave is recognized by the earth particle movement (displacement) direction.

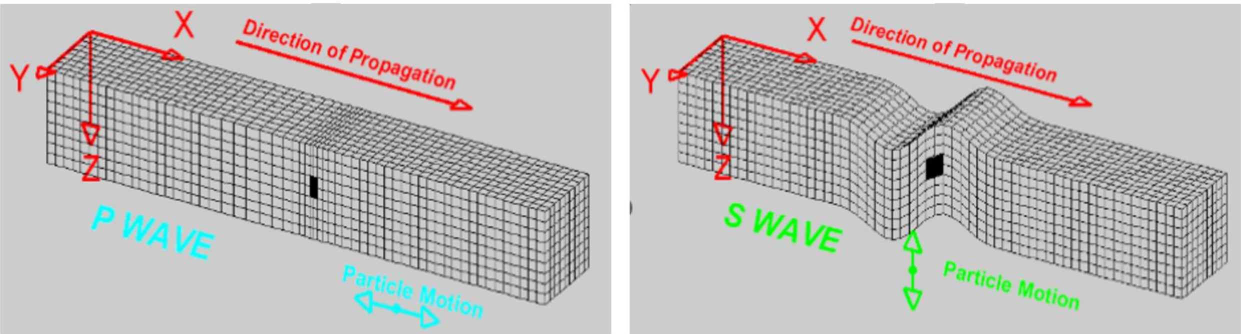

Figure 1-4: Two types of body waves (Braille, Purdue University, 2010).

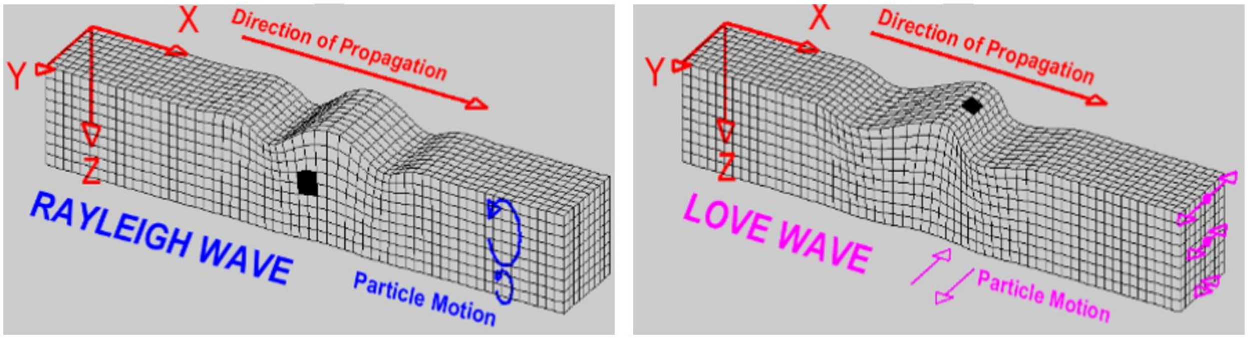

Figure 1-5: Two types of surface waves (Braille, Purdue University, 2010).

Waves are defined using several characteristics:

1. Wavelength (λ): The distance between points with similar amplitudes. One wavelength is the distance between consecutive peaks.
2. Amplitude (A): The maximum displacement of the earth's particle motion, or the peak displacement of a wave.
3. Period (T): The time for two consecutive waves to pass a reference point. Alternatively, the duration to complete one wave cycle.

4. Frequency (*f*): The number of wave repetitions in a given unit of time, or cycle of seismic waves.
5. Velocity (V): The distance a wave covers in a given unit of time.

The relationships between different wave characteristics are given in equations 1-1 and 1-2, and Figure 1-6 shows the wave characteristics on imaginary seismogram plots.

$$f = \frac{1}{T}\ (Hz\ or\ {}^{1}\!/_{s}) \qquad \text{Eq. 1-1}$$

$$V = \frac{Distance}{Time} = f\lambda \qquad \text{Eq. 1-2}$$

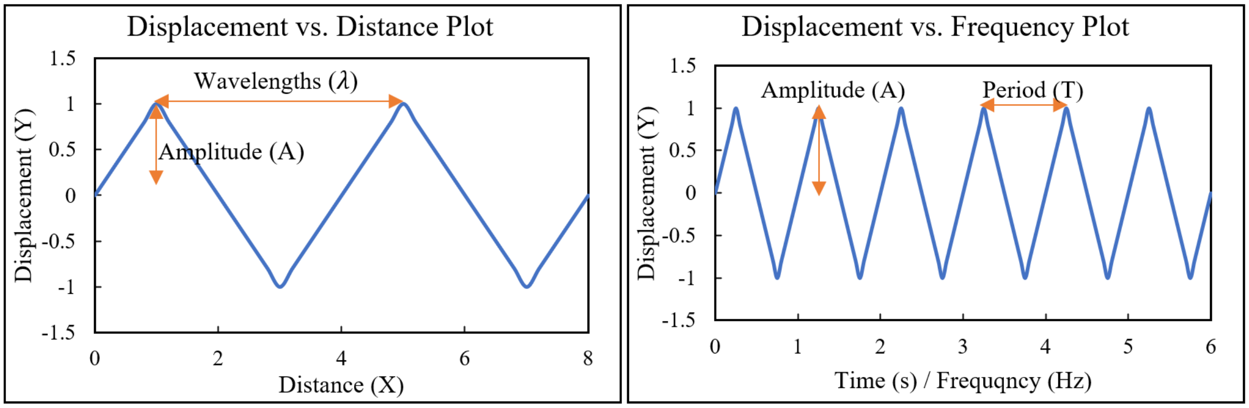

Figure 1-6: Seismic wave characteristics placed on imaginary seismogram data.

1.3. Traditional Seismic Protection Methods

Due to the damage and disasters caused by disastrous waves, researchers developed methods for seismic protection. Such methods are being used widely, including but not limited to shear walls, moment frames, and braced frames. Figure 1-7 shows different types of traditional seismic protection methods. Moment frames are a conventional seismic protection method made of typical steel beams and columns connected by welds or bolts; in some cases, frames can be made of standard concrete beams and columns. They can absorb wave energy through the rigid connections by bending the beams or columns. Shear walls are structural members typically located at elevators and stairs walls constructed by reinforced concrete. They can be rectangular, L-shaped, C-shaped, or a closed core wall. Lateral movement enters the building, and shear walls absorb this movement by transmitting it to the ground. Braced frames use crosses, V-shaped, diagonal, or eccentric-shaped steel structural elements such as beams and cables. Lateral resistance is provided by vertical or horizontal bracing.

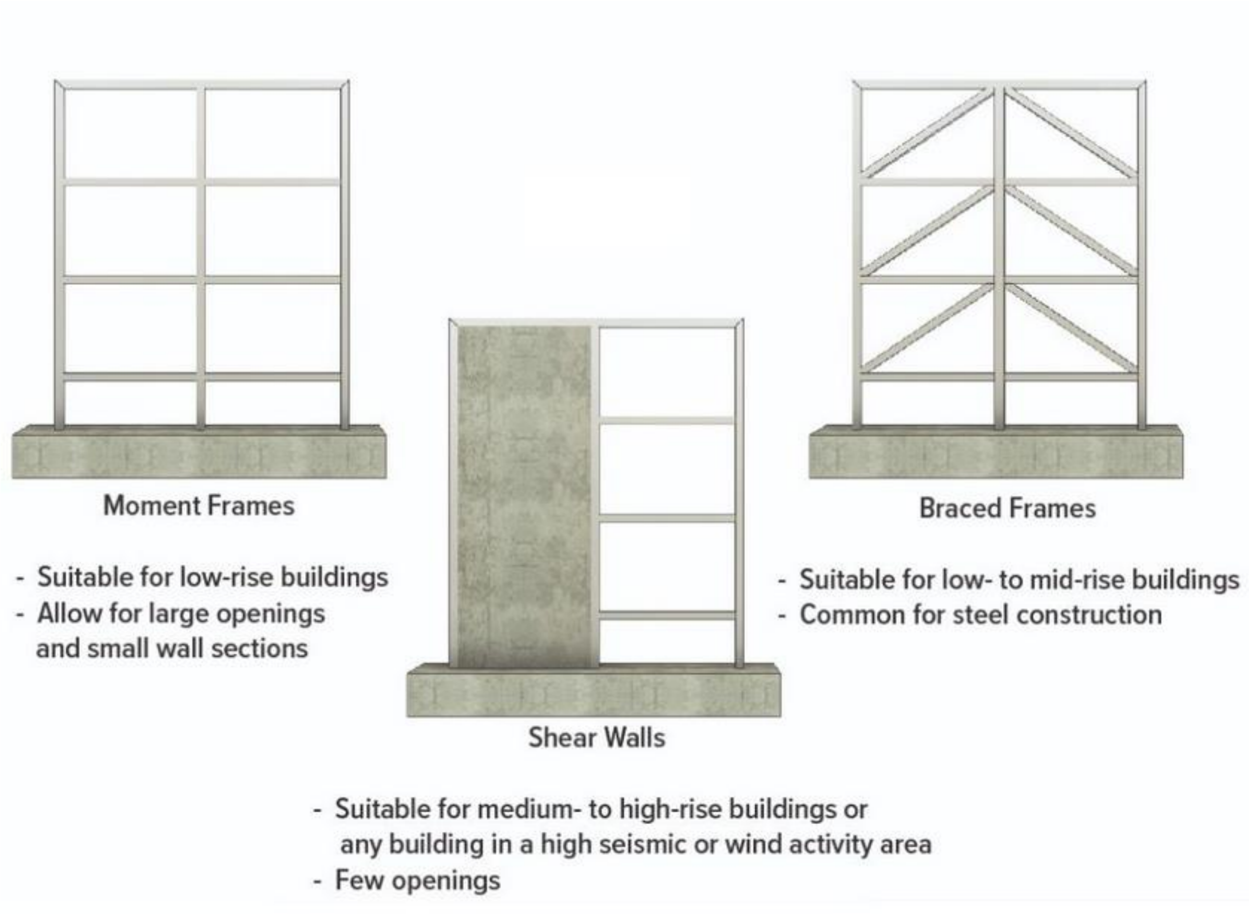

Figure 1-7: Traditional seismic protection methods (https://ccpia.org).

Additionally, there are more advanced techniques to protect or increase the seismic resistance of a structure. There are mainly three seismic resistance systems: passive, active and semi-active. A passive seismic control system utilizes passive techniques that do not require additional energy sources to function. Instead, the earthquake’s input motion activates the seismic control system. Passive seismic control systems commonly use energy dissipation devices, base isolation systems, and dynamic oscillators. Energy dissipation systems are mechanical systems affixed to a building structure and designed to absorb a significant portion of earthquake input energy by undergoing deformation and yielding, ultimately guarding the building structure. There are several energy dissipation devices (dampers), including but not limited to friction dampers and viscous dampers. These devices work by absorbing the energy generated by an earthquake and dissipating it through mechanical processes, thereby reducing the energy transmitted to the building structure. Friction dampers utilize the force of friction to dissipate energy. They typically consist of a sliding interface that is placed between two plates, which are clamped together. When an earthquake occurs, the plates slide against each other, generating heat and dissipating the earthquake's energy. Viscous dampers, on the other hand, utilize the force of viscosity to dissipate energy. They typically consist of a cylinder filled with fluid connected to the building structure.

When an earthquake occurs, the cylinder moves, causing the fluid to move through several valves, generating resistance and dissipating the earthquake energy. Figure 1-8 shows examples of viscous and friction dampers.

Base isolation systems are a structural engineering technique used to protect buildings and other structures from the effects of earthquakes and different ground vibrations. The method separates the structure from its foundation by inserting flexible bearings, such as rubber or lead, between the two. These bearings allow the structure to move freely during an earthquake, effectively decoupling it from the ground and reducing the transmission of seismic forces. Base isolation systems can be used in various structures, from bridges and dams to skyscrapers and nuclear power plants and are essential in mitigating the damage caused by seismic activity. Figure 1-9 shows how base isolation systems are implemented. While it offers significant advantages in reducing the transmission of seismic forces to structures, there are several limitations to consider. Firstly, the cost of implementing base isolation systems can be substantial, making it financially challenging for certain projects. Another drawback is the increased complexity of the structural system. Base isolation introduces additional components and interfaces, which need to be properly integrated with the overall design. This complexity can lead to potential complications during construction and may require specialized expertise. Furthermore, while base isolation can significantly reduce the impact of ground motion on buildings, it does not eliminate the structural response entirely. Large amplitude, long-duration ground motions or near-field earthquakes may still pose challenges even with base isolation (Xiong et al., 2012).

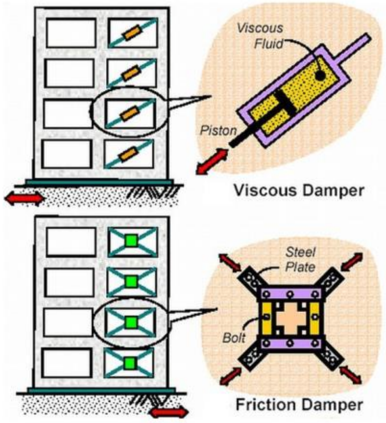

Figure 1-8: Viscous damper example (mathspig.wordpress.com, accessed 2023).

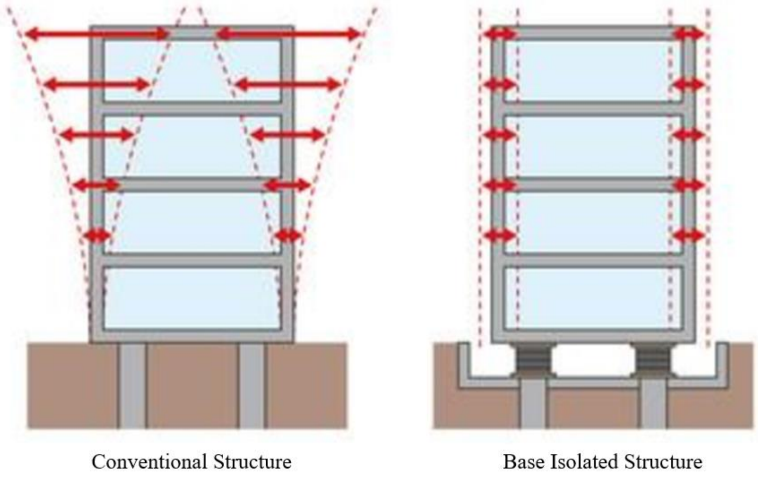

Figure 1-9: Base isolation system implementation (Verma et al., 2017).

Another passive seismic control system is the tuned mass dampers (TMD). It works by adding a mass-spring-damper system to the structure, which is tuned to the natural frequency of the structure. When the structure vibrates, the TMD moves in the opposite direction, reducing the amplitude of the vibrations. TMDs are often used in tall buildings and bridges to minimize the effects of wind and seismic activity, which can cause undesirable vibrations that affect the comfort of occupants and the structure's safety. They can also be used to control the vibrations of machinery and equipment. A TMD's effectiveness depends on the structure's properties and the mass-spring-damper system. Proper design and installation are crucial to ensure the TMD operates as intended. TMDs are a cost-effective solution for controlling vibrations in structures, and they have been used in many iconic buildings and bridges worldwide. One of the most famous buildings where the TMD system is implemented is Taipei 101 building located in China and uses 660 tons of TMD affixed at the top of the building, as shown in Figure 1-10.

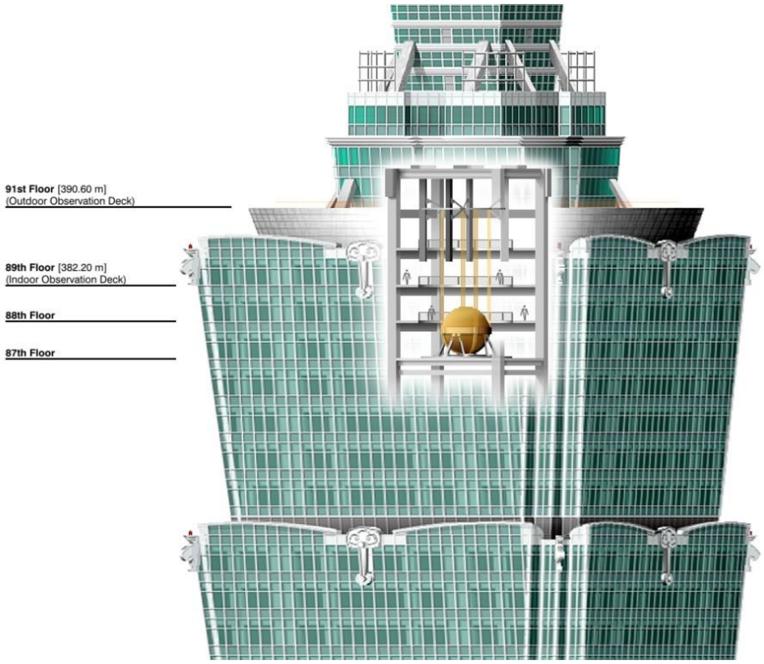

Figure 1-10: Taipei 101 building TMD (https://www.slate.com, accessed 2023).

On the other hand, active seismic control systems require external energy source, sensors, actuators, and computer algorithms to minimize the effects of seismic activity on buildings and other structures. When an earthquake occurs, these systems work by applying forces to counteract the movements caused by seismic waves. Active seismic control systems can be complex and expensive, requiring a continuous energy source and sophisticated control mechanisms. On the other hand, semi-active control is extensively utilized in the field of structural control due to its ability to combine the benefits of passive and active control methods, while avoiding their respective drawbacks. In essence, semi-active control represents an advanced form of passive control system, with the key distinction that the parameters of the semi-active control system can be adjusted based on the input excitation. This approach offers numerous advantages, including but not limited to a high level of robustness (Pourzeynali et al., 2016) and the utilization of a small power source (Alhan et al., 2006). Among the commonly employed devices in semi-active control, the magneto-rheological (MR) damper stands out, as it consists of magnetic fluid containing liquid magnetic particles. By subjecting the magnetic fluid to a magnetic field, the viscosity of the fluid can be precisely modified in a controlled manner (Jung et al., 2004).

Moreover, a more recent option that has emerged is the TMD with inerter (TMDI) as illustrated in Figure 1-11. The inerter is a lightweight component with negligible mass. It generates a reaction force that depends on the relative acceleration between its two terminals, with a proportionality coefficient, i.e. inertance (b). This inertance, also referred to as apparent mass, has the same units as mass and has the ability to greatly magnify the physical mass. Consequently, the inerter can effectively reduce the effects of vibration by simultaneously reducing the peak amplitude and expanding the frequency range over which vibration suppression occurs (Kaveh et al. 2020a, b; Hojat Jalali and Farzam 2022; Farzam and Hojat Jalali 2022.

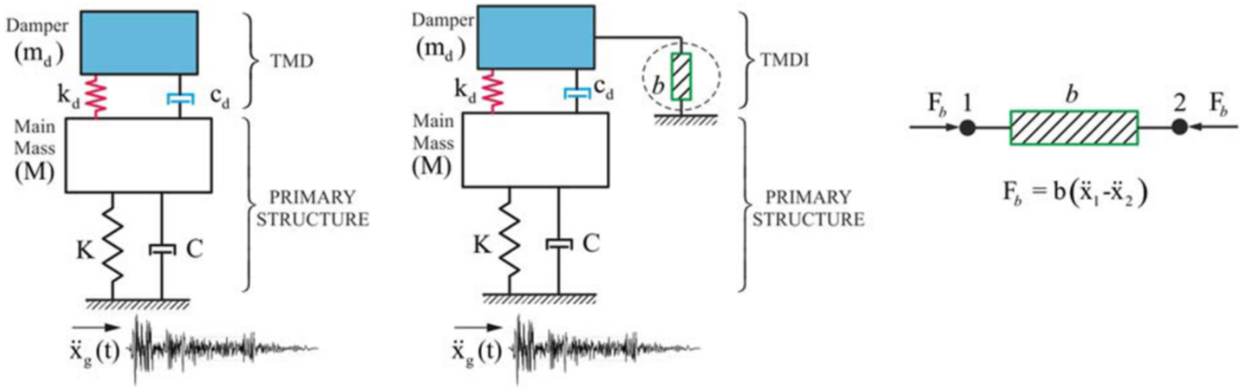

Figure 1-111: Basic concept of TMD (Right), TMDI (Mid), and ideal inerter. (Kaveh et al. 2020a)

1.4. Introduction to Seismic Metamaterials

Metamaterials are artificially engineered material that exhibit extraordinary properties that are not found naturally. They are made up of repeating units or patterns called periodicity. This unique structure allows metamaterials to manipulate waves in ways that cannot be achieved with conventional materials. The first metamaterial models were created in the 1980s, where the models focused on electromagnetic fields. After that, it expanded to include mode fields such as but not limited to aerospace engineering to reduce the weight of space rockets, lenses, mechanical engineering as vibro-acoustics to isolate machinery vibrations, and automobiles to reduce their weight.

One of the most significant advantages of metamaterials is their ability to control the flow of electromagnetic radiation. They can be designed to bend, reflect, and absorb light in specific ways, making them ideal for use in optical devices such as lenses, sensors, and filters. They can also be used to create cloaking devices that make objects invisible to specific wavelengths of light. Metamaterials also have a wide range of potential applications in the field of telecommunications. They can be used to create ultra-high-speed communication networks by controlling the propagation of electromagnetic waves in new ways. Metamaterials can also be used to develop materials that are much lighter and stronger than conventional materials, making them ideal for use in aerospace and defense applications. Another promising application of metamaterials is in the field of energy.

Metamaterials can create more efficient solar cells by trapping light in the cell for extended periods, increasing the amount of energy that can be harvested (Liu et al. 2012). They can also be used to create more efficient thermal insulation, reducing energy losses in buildings and other structures. Moreover, metamaterials can be made using extreme (irregular) geometry. They are called, in this case, auxetic materials. Due to their complex geometry, extraordinary properties are created, such as negative Poisson’s ratio, where the material contracts when compressed and vice versa. Figures 1-12 through 1-15 show some metamaterial applications.

Figure 1-12: Auxetic metamaterial application in running shoes.

Figure 1-13: Metamaterial application in aerospace engineering (https://matlack.mechanical.illinois.edu/research/655-2/).

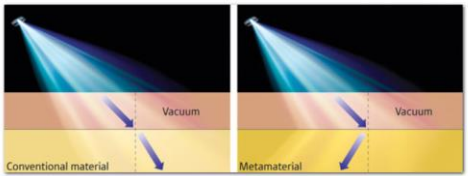

Figure 1-14: Metamaterial application in optical (https://www.nanowerk.com/what-are-metamaterials.php).

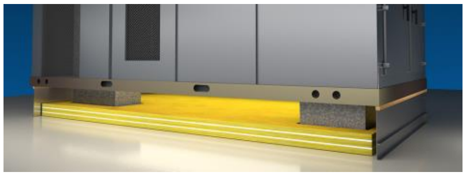

Figure 1-15: Metamaterial application in mechanical engineering (https://kineticsnoise.com/esr/vibration-isolation-curb).

Seismic metamaterials are a class of materials that have been developed to withstand the destructive forces of earthquakes. These materials are designed with specific properties that allow them to absorb and dissipate seismic energy, reducing the damage that can occur during an earthquake. Moreover, due to the unique mechanical properties, such as negative Poisson's ratio and negative bulk modulus, it can be exploited to manipulate the propagation of seismic waves. These materials comprise small building blocks or unit cells that are arranged periodically. Recent research has demonstrated that metamaterials can effectively block low-frequency seismic vibrations by tailoring the mechanical properties of the metamaterial to the frequency range of the incoming seismic wave (Achaoui et al., 2017; Gomez-Leon and Platero, 2013; Shi and Huang, 2013). In other words, the metamaterial can act as a seismic filter, attenuating the wave's amplitude and preventing it from propagating further. This has potential applications in earthquake engineering, where the ability to protect buildings and other structures from seismic waves can be crucial. One of the key advantages of seismic metamaterials is their ability to manipulate the propagation of seismic waves. By carefully controlling how seismic waves travel through a material, it is possible to reduce the amplitude of these waves and prevent them from causing damage. This is achieved by altering the material's mechanical properties on a small scale, using techniques such as micro-structuring or adding small-scale inclusions. The result is a material that behaves differently from conventional materials when subjected to seismic forces, with enhanced resilience and excellent damage resistance. Metamaterials usage in seismic protection has emerged with the first applications in electromagnetics, optics, and acoustics (Achaoui et al., 2017). Seismic resistance metamaterials (seismic shields, meta-barriers, or photonic crystals) are metamaterials with repeated patterns (periodicity). This periodicity can be in one, two, or three dimensions, as shown in Figure 1-16, where each color represents a unique material with unique properties. When combined, both materials represent a metamaterial unit cell.

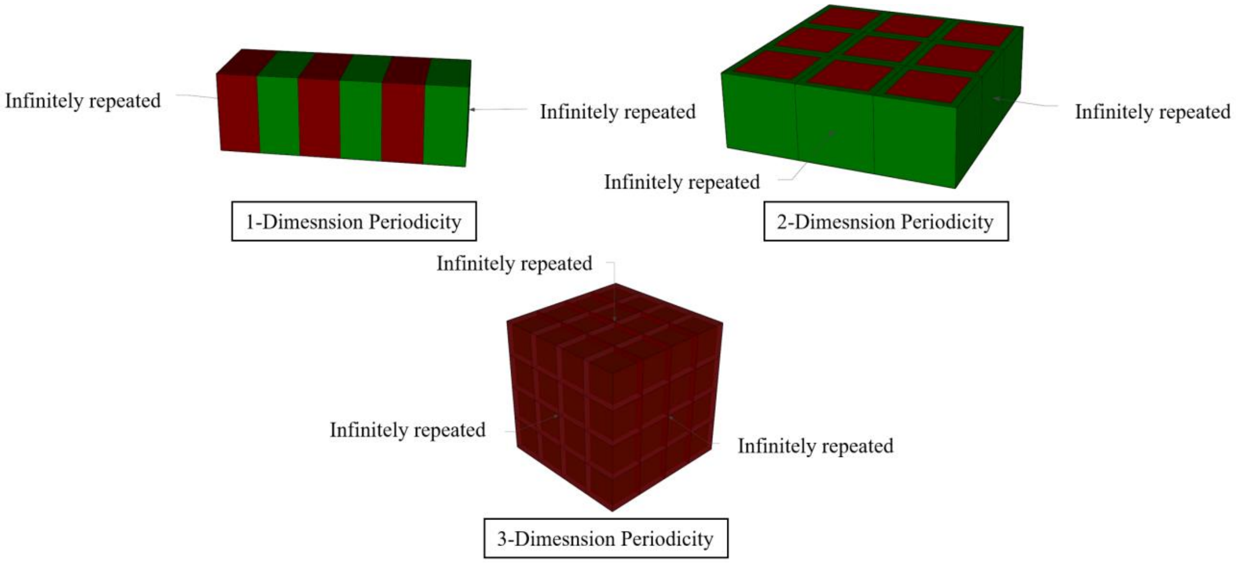

Figure 1-16: Seismic resistance metamaterial periodicity.

Figure 1-17 shows a typical 3-dimensional 3-axis periodicity unit cell (3D-3C) made of concrete matrix, rubber coating, and steel core.

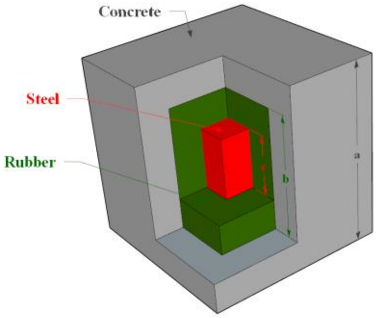

Figure 1-17: Typical 3D-3C unit cell.

Seismic metamaterial can be a combination of two or more unique materials with different sizes. This combination, along with periodicity, is capable of manipulating wave energy which leads to a significant reduction to complete stop of the wave. This is known as the attenuation zone (bandgap). Bandgap is a set of frequencies that cannot propagate through the material, and it exists due to the exceptional properties of metamaterials and their periodicity. They can be seen when solving the wave equation for a single unit cell and plotting the solution against the wave vector (wave number). The solution for the wave vector is known as the dispersion relation (Achaoui et al., 2017; Gomez-Leon and Platero, 2013; Shi and Huang, 2013). These bandgaps mainly depend on the material shape, size, and mechanical properties. Figure 1-18 shows a typical dispersion relation. The grey shaded area is the attenuation zone (bandgap) which has two limits: upper bandgap limit (UBGL) and lower bandgap limit (LBGL).

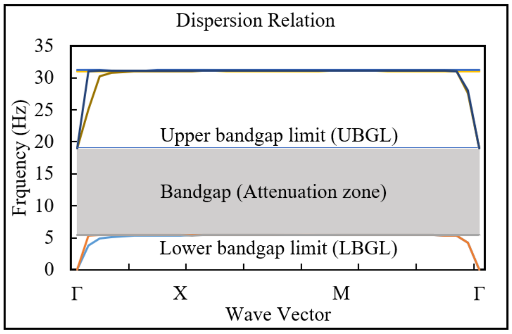

Figure 1-18: Typical dispersion relation for metamaterial unit cell.

Figure 1-19 shows a 3-dimensional 2-axis periodicity unit cell (3D-2C) along with the dispersion relation and the existing bandgaps in this unit cell. The unit cell is made of rubber matrix and steel core, and it has a cubic shape with 2 m side length (a, and h) and matrix thickness (b) of 0.1 m. The mechanical properties for rubber and steel are as follows: The modulus of elasticity, Poisson's ratio and density of the steel is considered as 210 GPa, 0.275 and 7890 kg/m^3, respectively; while those of rubber are 0.14 MPa, 0.463 and 1300 kg/m^3, respectively. After solving the wave equation for this unit cell, it yields four different bandgaps: the first one is between 4.5-12.5 Hz, the second bandgap is 12.7-13.0 Hz, the third is 13.1-14.1 Hz, and finally 14.2-15.3 Hz.

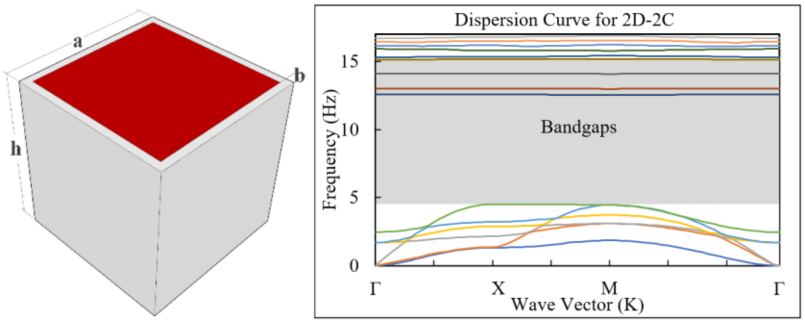

Figure 1-19: Dispersion relation and bandgaps for 3D-2C metamaterial unit cell.

Figure 1-20 shows the concept of meta-barriers to protect a structure from train-induced vibrations.

As the train passes, it generates waves ranging from 20-30 Hz; highways and heavy machinery generate the same wave frequencies. When the waves hit the building, it causes lateral displacement, which may lead to cracks, structural failure, and damage. Metabarriers can be engineered to block this range of frequencies. They would be arranged periodically and placed between the vibration source and the target building where the wave energy will dissipate, protecting the building from damage, as shown in Figures 1-20 and 1-21. In conclusion, meta-barriers can protect structures, infrastructures (bridges and railways), or sensitive buildings from seismic waves. It can be used on a large scale to cover a block, district or a new city by surrounding the target structure with metamaterials. Moreover, meta-barriers can be used to protect historical structures, sites, and remote sensitive buildings (such as but not limited to nuclear power plants).

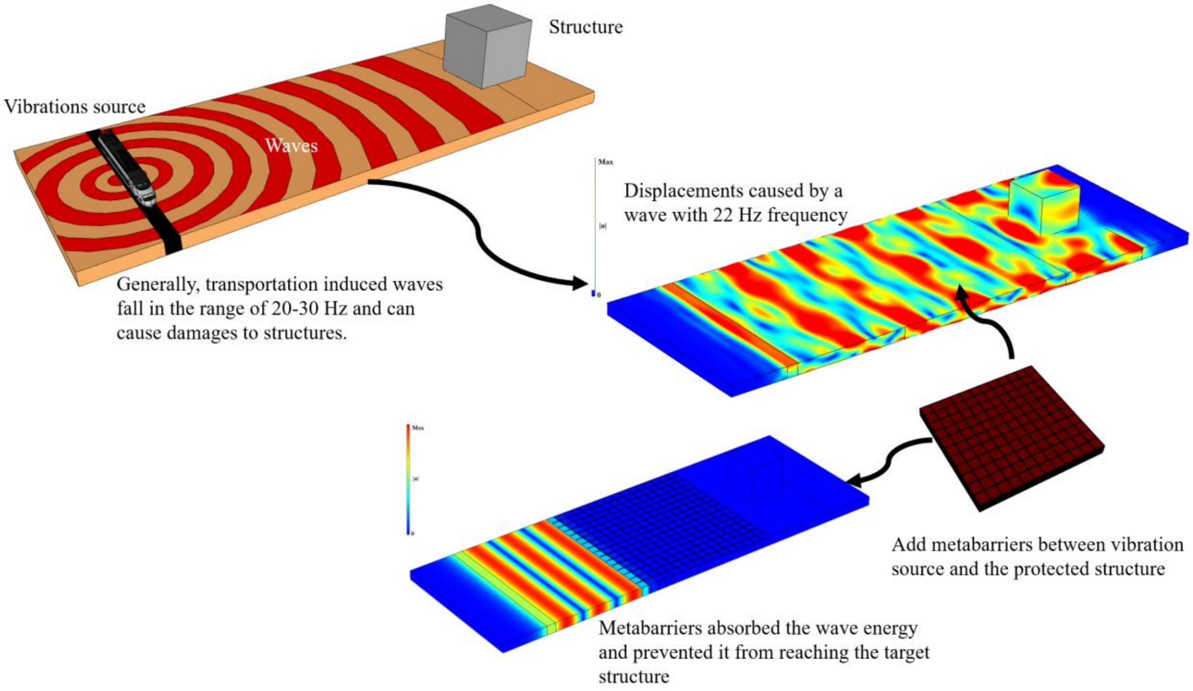

Figure 1-20: Protecting a structure from train-induced vibrations using meta-barriers.

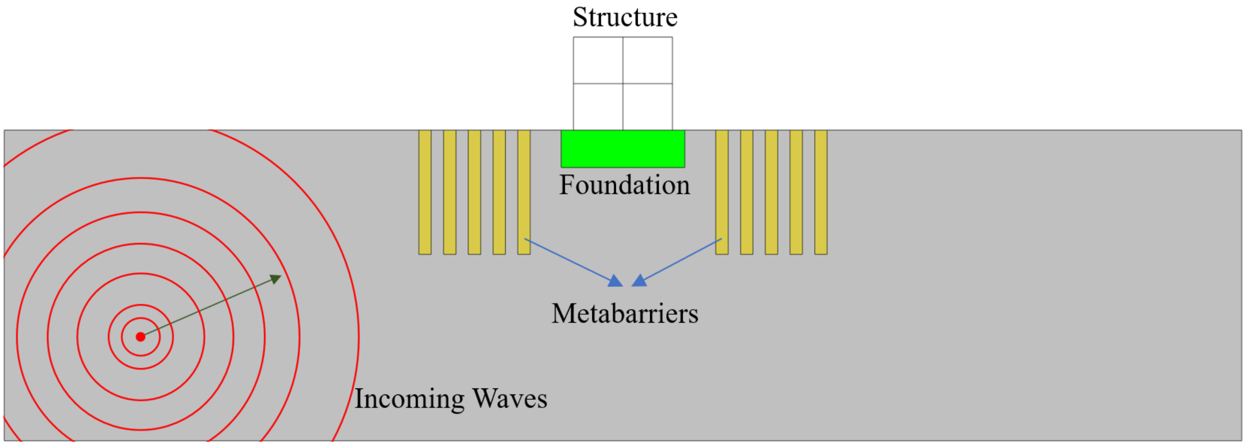

Figure 1-21: Typical meta-barriers protecting a structure.

1.5. Problem Statement

Traditional seismic protection techniques have certain limitations. For instance, yielding, overturn, and slippage may occur when base isolation is used, in addition to architectural complexities (Xiong et al., 2012). Moreover, base isolation systems can be expensive to install and maintain.

Additionally, while base isolation can reduce the damage a building sustains during an earthquake, it does not eliminate the risk and may not be effective in extreme seismic events (Xiong et al., 2012; Shi et al., 2013). Additionally, Friction dampers can be prone to wear and require regular maintenance to ensure their effectiveness. Viscous dampers, on the other hand, are more complex and expensive to install than friction dampers.

The recently proposed meta-barrier designs proved that such techniques could protect structures from seismic waves without making any change to the structure. However, many proposed techniques were composed of extra-large size unit cells (~10 m), making the design extremely challenging. Furthermore, having hollow unit cells makes it difficult to maintain the shape. Finally, clamping piles to bedrock might not seem feasible due to the depth at which bedrock is located and the possibility of having a perfect bond between the pile and the bedrock. Moreover, many of the proposed designs focused on the attenuation zones of the unit cell itself without any attempt to manipulate the unit cell array configuration to widen the bandgap.

Additionally, some metamaterial assumptions are difficult to implement and use uncommon construction materials. In addition, most of the research that has been performed focuses on analyzing the soil-meta-structure system in the frequency domain. Therefore, more research is needed to fill gaps not addressed in the literature.

1.6. Objectives and Study Parameters

This research focuses on blocking waves in the range of destructive seismic waves (0-30 Hz) using common construction materials and relatively reasonable size. Moreover, the frequency blocking range is manipulated without changing the unit cell design. The objectives of this research are summarized as follows:

1. To develop a practical metamaterial unit cell configuration using common construction materials.
2. To evaluate metamaterial geometrical and mechanical properties and their effects on the attenuation zone.
3. To develop and optimize the unit cell configuration.
4. To validate the unit cell capability for seismic protection in frequency domain analysis and obtain a wide bandgap.
5. To analyze the performance of meta-materials in the time domain

The parameters that will be covered in the research are as follow:

1. Metamaterial unit cell size and geometry (block, sphere, cylinder, honeycomb, and array of unit cells).
2. Metamaterial unit cell outer layer (matrix) and interior layer (core) properties such as density and Young's modulus.
3. The number of unit cell layers/materials.
4. Effects of grading the unit cells on wave propagation
5. Number of unit cells in grading configuration.
6. Type of wave (bulk vs. surface)

This study aims to introduce a new configuration using common construction materials such as concrete, steel, and rubber and to increase the attenuation zone as much as possible. To this end, unit cells with different shapes are investigated, and the effect of the mechanical properties of the matrix and core on the bandgap are evaluated. Furthermore, the unit cell is placed in a simplified FEA model and is analyzed to evaluate the performance of grading the design under bulk waves. Moreover, the double grading configuration is evaluated when embedded in a larger soil medium subjected to low-amplitude harmonic bulk and surface waves, and its effects on the response of a single degree of freedom structure (SDOF) are evaluated. Finally, the performance of the configuration has been tested in the time domain under three different wavelets Ormsby wavelet, Ricker wavelet, and the 1975 Oroville dam earthquake.

CHAPTER 2 : LITERATURE REVIEW

This chapter summarizes the proposed seismic- meta-barriers and in-depth details of some of the most promising configurations.

2.1. Introduction

Traditionally, structures are designed to withstand earthquakes using different methods such as but not limited to shear walls, moment frames, braced frames, base isolation systems, and structural control systems. Such systems are designed to absorb and dampen the earthquake energy by shifting the structure's natural frequency by adding bearings to the foundation (Xiang et al., 2012) or by changing the structural parameters by adding mass or damping devices (Shi et al., 2013). Metamaterials were first implemented in the field of electromagnetics in the 1980s. In the past two decades, seismic metamaterials gained the attention of researchers from different areas, and several configurations were proposed to resist the most disastrous waves (waves with frequencies between 0-30 Hz). Metamaterials are artificially engineered materials (i.e., unit cells) that exhibit extraordinary properties that cannot be found naturally. Due to these properties, they can block a specific range of wave frequencies (bandgap) and protect the structure from waves (John, 1987; Sukhovich et al., 2009; cheng et al., 2013; Zhang et al., 2019; Daradkeh et al., 2022). The bandgaps can be found by assuming that every two opposite sides of the unit cell are repeated infinitely (periodic boundary conditions) using the Floquet-Bloch theory (Achaoui et al., 2017; Gomez-Leon and Platero, 2013; Shi and Huang, 2013). The bandgaps depend solely on the unit cell size, shape, and material properties (Shi and Hunag, 2013; Huang and Shi, 2013; Zhang et al., 2021). The challenge with the most disastrous waves is that they have very long wavelengths that can extend to thousands of meters, depending on the nature of the soil. Such wavelengths can be controlled using relatively small-scale metabarriers with local resonance (Khelif et al., 2010; Brule et al., 2017; Colombi et al., 2016). Shi and Huang (2013), Miniaci et al. (2016), Zhang et al. (2021), and Daradkeh et al. (2022) proposed 3D large-scale metabarriers designs and tested them for blocking ultra-low-frequency waves.

Ultra-low-frequency blocking has been developed using circular piles clamped to deep bedrock layers (Chen et al., 2019). Colombi et al. (2016) and Liu et al. (2019) investigated resonance metamaterials such as natural forests in uniform and random configurations and concluded that they could attenuate low-frequency waves. Several other designs have emerged recently, such as but not limited to iron spheres (Achaoui et al., 2017), cubes, hollow structures, and circular piles (Huang and Shi, 2013; Miniaci et al., 2016; Chen et al., 2019; and Zeng et al., 2019). Shi and Hunag (2013) were the first to propose a 3D-3C unit cell made of concrete matrix, rubber coating, and steel core. The shape is a cube with a matrix size of 1.2 m, a thickness of 0.2 m, and a core size of 0.8 m. Figure 2-1 shows the proposed unit cell, and Table 2-1 shows the mechanical properties of the used materials.

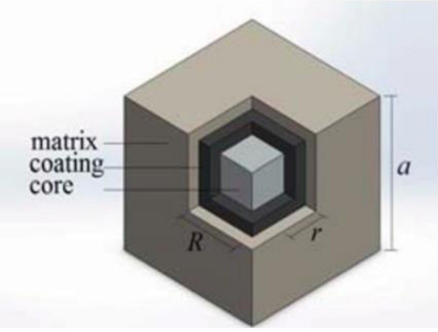

a	**1.2m**
R	**1.0m**
r	**0.8m**

Figure 2-1: 3D-3C unit cell (Shi and Huang, 2013).

Table 2-1: Material properties of 3D-3C (Shi and Huang, 2013).

Material	Young's Modulus E (Pa)	Poisson's Ratio (v)	Density ρ (kg/m^3)
Concrete	30.0×10^9	0.200	2500
Rubber	1.37×10^5	0.463	1300
Steel	210×10^9	0.275	7890

They investigated the existence of bandgap in this unit cell using periodicity, Floquet-Bloch Theorem (Madelung, 1978), in which every two opposite sides of the unit cell, along the X, Y, and Z-axis are infinitely repeated, that can be done by equating the displacement on one side to the displacement on the parallel side on the unit cell.

Thereafter, the governing equation (wave equation) can be solved using the First Irreducible Brillouin Zone (Brillouin, 1930), which is symmetry regions on the body of the unit cell. The solution of the wave equation is repeated along each one of these symmetry regions. Therefore, solving the wave equation using only the First Irreducible Brillouin Zone (FIBZ) is sufficient. Results showed that the proposed unit cell could block frequencies in the 8.09-14.14 Hz range, as shown in Figure 2-2.

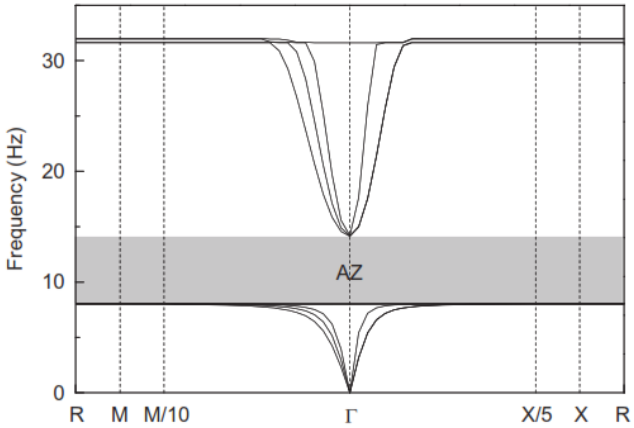

Figure 2-2: Dispersion relation of 3D-3C (Shi and Huang, 2013).

Colombi et al. (2016) investigated the potential of natural forests to act as metamaterial and block seismic waves due to local resonance. They used FEA to simulate a natural forest with various tree heights and radii distributed at different spaces, as shown in Figure 2-3.

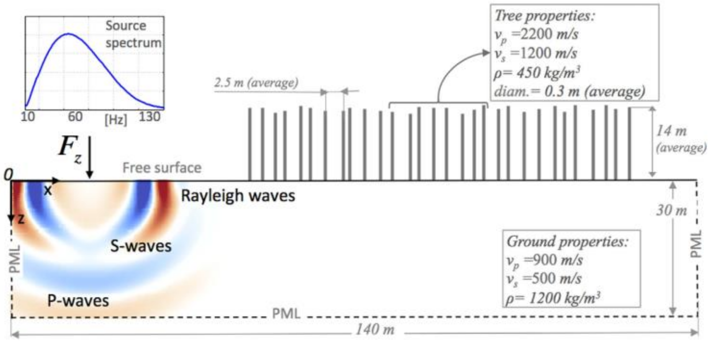

Figure 2-3: FEA of natural forests in seismic protection (Colombi et al., 2016).

They applied low-harmonic displacement and recorded the displacement from different frequencies at different locations along the model. They found that natural forests can block frequencies in 25-40 Hz and 90-110 Hz. Figure 2-4 Shows the dispersion relation of the investigated natural forest.

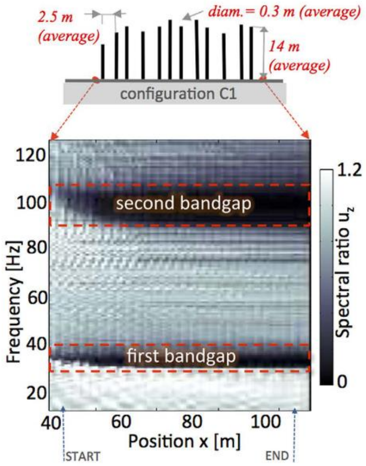

Figure 2-4: Dispersion relation of the investigated natural forest (Colombi et al., 2016).

Liu et al. (2019) studied the bandgap of 2D-2C using 2D FEA simulations and included the effects of vertical loads imposed on the foundations by the upper structure. The size of the proposed unit cell was 2m with three materials layers concrete, rubber, and steel. They found out that the attenuation zones are affected by any additional loads imposed on the metabarriers.

More recently, Zhang et al. (2021) proposed a unit cell with different configurations of a cube matrix with hollow cross core, solid cross core, hollow cube core, and solid cube core. The unit cell size is 10 m, and steel was the core material surrounded by soil. Figure 2-5 shows the proposed unit cells and each corresponding dispersion relation where the grey shaded areas represent the bandgap of each configuration. The widest bandgap was between 6.2-15.8 Hz when the unit cell was a 10 m cube with a solid steel core.

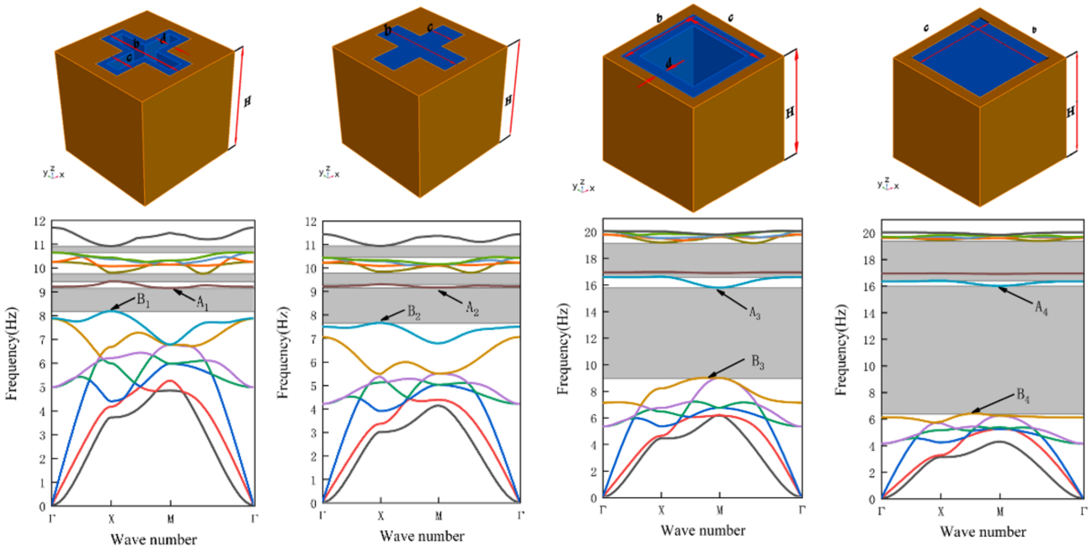

Type 1 Type 2 Type 3 Type 4

Figure 2-5: Types of proposed unit cells and their corresponding dispersion relation (Zhang et al., 2021).

2.2. Literature Progress

Multiple studies proposed different unit cell designs and investigated unit cell parameters and their effects on the attenuation zones. Table 2-2 shows the literature progress in seismic metamaterials, including proposed unit cell description, size, materials used, and the obtained bandgap.

Table 2-2: Summary of literature progress in seismic resistance metamaterials.

Year	Author	Setup Description	Material Used	Lattice Width	Band Gap
2011	Xiong et al.	2D Concrete lattice with Rubber ring in the middle stacked	Concrete and rubber	0.4m	14.8-24.3 Hz
2013	Cheng et al.	Cube with cylinder rubber and steel core	Concrete, rubber, and steel	2m cell, 0.2 coating thickness, and 0.7 core radius	7.22, 10.10Hz
2012	Xiang et al.	1D Structure along the Z-direction	Concrete and rubber	0.2m	6.6–15.0Hz 17.8–30.0Hz 31.6–45.0Hz 46.1–60Hz 25.0 to 57.2Hz 67.9–114.3Hz
2013	Shi et al.	Three cubes	Concrete, rubber, and steel	1.2m	8.9-14.14 Hz
2016	Miniaci et al.	Block cell and cross and cylinder core	Soil, rubber, and concrete/steel	10m cross 10m hollow cylinder 2m coated cylinder	2-3 Hz cross 5.5-6.5 Hz hollow cylinder 3.5-4Hz coated cylinder
2017	Achaoui et al.	Circular piles	Steel	0.15 to 0.6 m	0-30 Hz

2017	Du et al.	1. Hollow cylinder core 2. hollow rectangular 3. hollow square block core 4. blocks	Soil, concrete, and steel	10m	1. 10-12Hz 2. 9-20Hz 3. 8-24Hz 4. 8-23Hz
2018	Geng et al.	1D Structure along the X-direction	Concrete and rubber	0.2m	9-15Hz 20-30Hz 31-45Hz
2018	Du et al.	Composite steel H-section	Steel	2.5m	8-14 Hz
2019	Liu et al.	2D squares	Concrete, rubber, and steel	2m cell, 0.2 coating thickness, and one core radius	4.69-7.49 Hz
2019	Chang et al.	1. square cell, rectangular core 2. square cell, circular core 3. square cell with star-shaped core	Concrete and steel	0.8m	multiple band gaps with the lowest limit is 250Hz
2019	Xu et al.	Honeycomb shape	-	-	0.077 to 0.174 Hz
2020	Li et al.	Square and cylinder	Soil and concrete/steel	0.3m	26–29Hz concrete 0–4.5Hz steel
2021	Miniaci et al.	Hollow Cross	Soil	5m	2.2 to 2.7 Hz
2021	Zhang et al.	Blocks	Steel and soil	10m	6-16 Hz
2021 (C)	Fiore et al.	Circular Steel Connected with concrete plate via rubber bearings	concrete, rubber, and steel	-	2.8-5.8 Hz
2022	Checn et al.	Square with a cut along the sides	Soil, rubber, and steel	Varies (lowest 2.5m)	Varies (Highest 7.8-20.6 Hz)

2021	Muhammad et al.	1. Concrete block and rubber 2. Steel cylinder	Concrete, rubber, and steel	1.5m	8-18 Hz 3-18 Hz (Descending configuration) 3-18 Hz (Ascending configuration)

CHAPTER 3 : BANDGAP THEORY, METHODOLOGY, AND PARAMETRIC STUDIES

This chapter presents the bandgap theory, periodic boundary condition (PBC), the first irreducible Brillouin zone (FIBZ), and the methodology for numerically solving the theoretical problem. Furthermore, the proposed plan for the parametric study performed in this research is presented.

3.1. Theories and Computational Methods

This section will present the bandgap theory, numerical solution, PBC, FIBZ, and structure natural frequency.

To have a clear picture of the attenuation zones, the following are assumed:

1. All materials are assumed to be linear elastic, and homogenous.
2. The layers of the unit cells are perfectly bonded.
3. Each unit cell is assumed to be infinitely repeated (periodicity).

3.1.1. Bandgap Theory

To evaluate the bandgap of any material, considering an elastic wave along X-axis, the equation of motion (Equation 3-1) can be utilized together with the periodicity to produce a proper solution. Equation 3-1 is derived from Newton's second law of motion.

$$\frac{\partial^2 u_i}{\partial t^2} = C_i^2 \frac{\partial^2 u_i}{\partial x^2} \qquad \text{Eq. 3-1}$$

Where i is the layer number, u_i is the displacement in each layer, and C_i is the wave velocity in each layer. To simplify the wave equation solution, the unit cell is assumed to consist of two materials A and B. Furthermore, the unit cell is repeated in one direction (Along the X-axis), as shown in Figure 3-1. a_1 and a_2 are the size of each layer of the unit cell, and the unit cell size is a_1+a_2. The wave is assumed to be perpendicular to the Y-Z plane and along the X-axis.

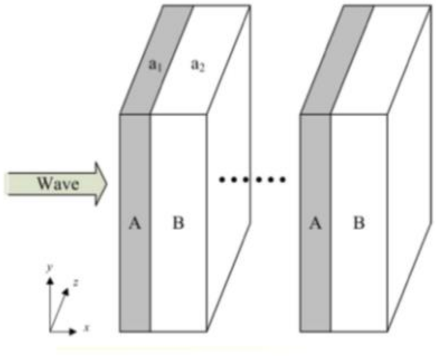

Figure 3-1: Used unit cell for numerical evaluation (Geng et al., 2018).

Equation of motion can be written in the form shown in Equation 3-1. This equation was introduced in the early 1800s.The wave velocity for longitudinal waves (P-wave) is given by Equation 3-2, and for transverse waves (S-waves) is given by Equation 3-3, where $\lambda, \mu,$ and ρ are the two Lamé constants and density, respectively.

$$C_i = \sqrt{\frac{\lambda_i + 2\mu_i}{\rho_i}} \qquad \text{Eq. 3-2}$$

$$C_i = \sqrt{\frac{\mu_i}{\rho_i}} \qquad \text{Eq.3-3}$$

To solve the equation of motion (Equation 3-1), the forward and backward propagating waves must be added in each layer. Hence, the solution becomes as shown in Equation 3-4.

$$u_i(x,t) = A_i e^{j(k_{ix} - \omega t)} + B_i e^{j(-k_{ix} - \omega t)} \qquad \text{Eq. 3-4}$$

Where ω is the angular frequency, j is the imaginary unit, k_i is the wave number = $\frac{\omega}{c_i}$, and A_i, B_i are the displacements at each layer, noting that each layer has two displacements, A_1, A_2, and B_1, B_2. Thereafter, to find a solution for Equation 3-4, the Floquet-Bloch theory must be implemented using periodicity (Equation 3-5).

$$u_1(0,t) = u_2(0,t) \qquad \text{Eq. 3-5}$$

Equation 3-5 reflects that the displacements on each two opposite sides of each layer are equal. Thereafter, Equation 3-5 can be written in steady-state wave expression with the wave number to Equation 3-6.

$$u_i(x,t) = U_i(x)e^{j(kx-\omega t)} \qquad \text{Eq. 3-6}$$

Where $U_i(x) = A_i e^{j(k_t-k)x} + B_i e^{j(-k_t-k)x}$ represent the displacement on one side of the unit cell, considering 1D periodicity with a lattice constant = a. Equation 3-7 can be written using Floquet-Bloch Theory. With the same approach described above, the equation of motion can be written in terms of stress using the Floquet-Bloch theory, as shown in Equation 3-8.

$$U_1(-a_1) = U_2(a_2) \qquad \text{Eq. 3-7}$$

$$\sum\nolimits_1 (-a_1) = \sum\nolimits_2 (a_2) \qquad \text{Eq. 3-8}$$

Thereafter, displacement and stress components will be assembled into matrix form, including the forward and backward propagating waves. Equation 3-9 can be written, which is a linear equation of a homogenous system.

$$\begin{bmatrix} 1 & 1 & 2 & 2 \\ \rho_1\, C_1 & -\rho_1\, C_1 & \rho_2\, C_2 & -\rho_2\, C_2 \\ e^{-j(k_1-k)a_1} & e^{j(k_1+k)a_1} & e^{j(k_2-k)a_2} & e^{-j(k_2+k)a_2} \\ \rho_1\, C_1 e^{-j(k_1-k)a_1} & -\rho_1\, C_1 e^{j(k_1+k)a_1} & \rho_2\, C_2 e^{j(k_2-k)a_2} & -\rho_2\, C_2 e^{-j(k_2+k)a_2} \end{bmatrix} \begin{bmatrix} A_1 \\ B_1 \\ -A_2 \\ -B_2 \end{bmatrix} \qquad \text{Eq. 3-9}$$

$$= 0$$

To solve Equation 3-9, the determinant of the coefficient matrix must equal zero. Otherwise, the solution will include trivial solution sets. Equating the determinant to zero, the dispersion relation for the unit cell can be obtained (Equation 3-10).

$$\cos(ka) = cos\frac{\omega a_1}{C_1}cos\frac{\omega a_2}{C_2} - 0.5\,sin\frac{\omega a_1}{C_1}sin\frac{\omega a_2}{C_2}\left(\frac{\rho_1 C_1}{\rho_2 C_2} + \frac{\rho_2 C_2}{\rho_1 C_1}\right) \qquad \text{Eq. 3-10}$$

Since $\cos(ka)$ equals or less than 1, Equation 3-10 can be solved when the right-hand part of the equation is in the range of (-1 to 1). The bandgaps of the unit cell are the values of frequency (ω) and wave vector (**k**) when $\cos(\boldsymbol{k}a)$ falls outside the range of (-1 to 1). The combination of frequency and wave vectors when $\cos(\boldsymbol{k}a)$ falls in the range of (-1 to 1) is known as the dispersion relation. When the values are plotted, gaps will be present (Solutions to Equation 3-10 when $\cos(\boldsymbol{k}a)$ is outside the range (-1 to 1)); these gaps are a range of frequencies that cannot propagate through the unit cell (attenuation zones or bandgaps). When individual material is considered, and the bandgap equation is solved, $C_1 = C_2$ and $\rho_1 = \rho_2$, then by solving Equation 3-10 for any value of k, the frequency ω can be found. Therefore, for homogenous material, there will be no bandgap. Generally, the dispersion equation can be solved to find the values of $\omega\ and\ k$. However, the wave vector ***k*** is unlimited and can be any number. Therefore, it is sufficient to solve the dispersion equation along the FIBZ (Kittel, 2005; and Xiang et al., 2012).

3.1.2. First Irreducible Brillouin Zone

As introduced previously, the FIBZ is sufficient to solve the dispersion relation and find the attenuation zone of a unit cell. After the FIBZ, the dispersion relation will keep repeated infinitely. To find the FIBZ on any unit cell geometry, it is required to find the symmetry points that define the FIBZ (Brillouin, 1930).

Figure 3-2 shows the symmetry points for a 3D cube unit cell that defines the FIBZ. Where points X, M, R, and Γ are the bounds that define the FIBZ.

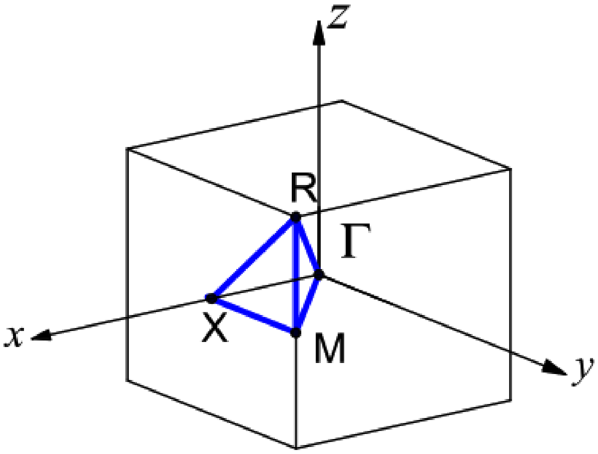

Figure 3-2: First irreducible Brillouin zone.

Table 3-1 shows the coordinates of the symmetry points on the FIBZ.

Table 3-1: Coordinates of the symmetry points along the FIBZ.

Point	Coordinates (u, v, w)	Wave vector (k_x, k_y, k_z)
Γ	(0, 0, 0)	(0, 0, 0)
X	(1, 0, 0)	$(\frac{\pi}{a}, 0, 0)$
M	(1, 1, 0)	$(\frac{\pi}{a}, \frac{\pi}{a}, 0)$
R	(1, 1, 1)	$(\frac{\pi}{a}, \frac{\pi}{a}, \frac{\pi}{a})$

where a is the length of the unit cell in the respective axis (lattice constant). Thereafter, the lengths of the vectors that represent the outer surface of the FIBZ can be calculated, $\overrightarrow{RM} = 1, \overrightarrow{M\Gamma} = \sqrt{2}$ $\overrightarrow{\Gamma X} = 1, and\ \overrightarrow{XR} = \sqrt{2}$.

Another solution is calculating the reciprocal base vectors as shown in Equations 3-11, 3-12, and 3-13.

$$b_1 = 2\pi \frac{R_2 \times R_3}{R_1 . (R_2 \times R_3)} \qquad \text{Eq. 3-11}$$

$$b_2 = 2\pi \frac{R_3 \times R_1}{R_1 . (R_2 \times R_3)} \qquad \text{Eq. 3-12}$$

$$b_3 = 2\pi \frac{R_1 \times R_2}{R_1 . (R_2 \times R_3)} \qquad \text{Eq. 3-13}$$

Where R_1 = (a, 0, 0), R_2 = (0, a, 0), and R_3 = (0, 0, a) are the unit vector along each axis, and a is the lattice constant. Solving equations 3-11 through 3-13 will yield the reciprocal base vectors that will be used to find the components of the wave vector.

$$b_1 = \frac{2\pi}{a}(1,0,0), b_2 = \frac{2\pi}{a}(0,1,0), and\ b_3 = \frac{2\pi}{a}(0,0,1)$$

The wave vector ***k*** can be calculated using Equation 3-14.

$$\boldsymbol{k} = c_1 k_x + c_2 k_y + c_3 k_z \qquad \text{Eq. 3-14}$$

Where c_1, c_2, and c_3 are wave number constants equal to half the reciprocal base vectors. Finally, to solve the dispersion equation (Equation 3-10), the FIBZ will be limited to the wave vectors $\overrightarrow{RM}, \overrightarrow{M\Gamma}, \overrightarrow{\Gamma X}, and\ \overrightarrow{XR}$. As a result, the wave vector ***k*** would range from 0 to 4.414. The wave vector components can be linearly interpolated, as shown in Figures 3-3.

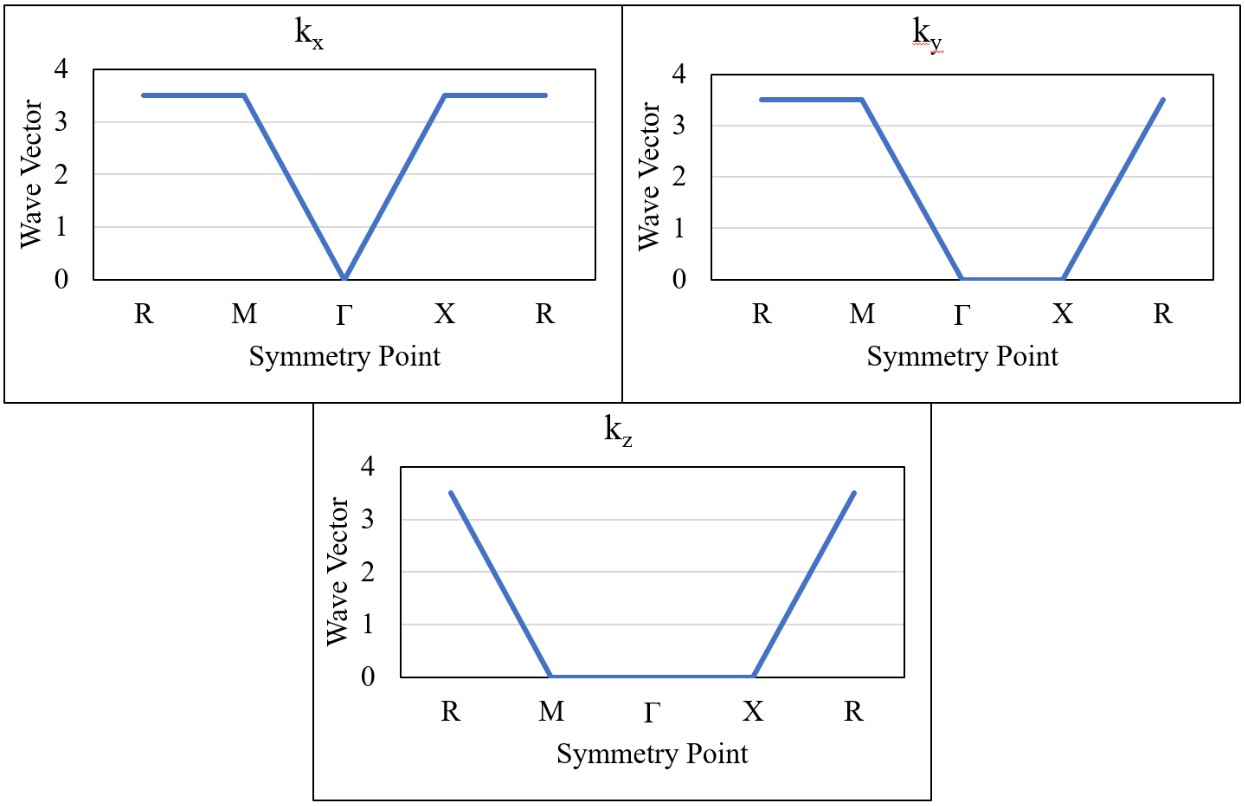

Figure 3-3: Relationship between wave vector value and symmetry points along FIBZ.

For 3-dimensional periodic metamaterial, the dispersion relation can be written considering that the displacement, stress, and wave vector have three components, X, Y, and Z, and the same approach in section 3.1.1 as shown in Equation 3-15 (Mei et al., 2003).

$$\frac{E}{2(1+v)}\nabla^2 \boldsymbol{u} + \frac{E}{2(1+v)(1-2v)}\nabla(\nabla.\boldsymbol{u}) = -\rho\omega^2\boldsymbol{u} \qquad \text{Eq. 3-15}$$

Where **u**: displacement vector, ω: angular frequency, and E, v, and ρ are the material properties, the periodic boundary conditions can be written in Equation 3-16 (Gomez-Leon et al., 2013).

$$u_i(\boldsymbol{r} + \boldsymbol{a}) = e^{i\boldsymbol{k}.\boldsymbol{a}}\, u_i(\boldsymbol{r}) \qquad \text{Eq. 3-16}$$

where **r**: position vector (x, y, z) along the boundary of the unit cell, **k**: Bloch wave vector (k_x, k_y, k_z) which is limited to the first Brillouin zone, and a: lattice translation vector. Combining Equations 3-15 and 3-16, considering that each variable has three components in each axis, the dispersion equation can be written as Equation 3-17, which is an eigenfrequency problem.

$$(\boldsymbol{K} - \omega^2 \boldsymbol{M})\boldsymbol{u} = 0 \qquad \text{Eq. 3-17}$$

where **u**: displacement vector at all nodes, **K**: stiffness matrix, and **M**: mass matrix of the unit cell. Manually solving this equation will take significant time since the unit cell has to be discretized (meshed) into smaller pieces, and every two opposite nodes must be related using periodic conditions. Therefore, employment of FEA programs such as but not limited to COMSOL Multiphysics, and ABAQUS/CAE will help numerically solve such a system of equations.

3.1.3. Natural Frequency of the Structure

The natural frequency of a structure (resonance frequency) is the frequency at which the structure oscillates indefinitely in the absence of any driving forces under the idealized condition of no damping (Paz et al. 2004). The natural frequency depends on the mass and the stiffness distributed within the structure. When the structure is subjected to external forces, the structure tends to amplify the response as the frequency moves towards the natural frequency, and the structure tends to de-amplify the displacement as the frequency moves away from the natural frequency. The structure vibration response can be significant at any small force or displacement at the natural frequency. The natural frequency of a structure can be calculated using Equation 3-18.

$$f = \sqrt{\frac{K}{M}} \times \frac{1}{2\pi} \qquad \text{Eq. 3-18}$$

where f, K and M are the natural frequency (Hz), stiffness of structure (N/m), and mass (kg) of the structure. The governing equation of motion must be employed to calculate the displacement/acceleration transmission from the foundation to the top of the structure assuming zero damping (Equation 3-19).

$$T_r = \left|\frac{1}{1 - r^2}\right| \qquad \text{Eq. 3-19}$$

where *r* is the amplification factor and is given by equation 3-20.

$$r = \frac{2\pi f}{\omega_n} \qquad \text{Eq. 3-20}$$

where *f* is the excitation frequency, and ω_n is the natural frequency rad/sec.

3.2. Methodology of Solving Dispersion Equation (Eigenfrequency Problem)

This section presents the methodology used to solve the dispersion equation (Equation 3-17) to find the dispersion relation of the proposed unit cell. As explained in section 3.1, to find the dispersion relation of a unit cell, the governing wave equation must be established along with the periodic pattern of the unit cell. The resulting equation (Equation 3-10, or Equation 3-17) is then solved to find the frequency (ω) and wave vector ($\boldsymbol{k}$), which represent the dispersion relation of a unit cell.

Since each term in the equation (**u**: displacement vector at all nodes, ***K***: stiffness matrix, and ***M***: mass matrix of the unit cell) has three different components, and every two opposite points on the unit cell must be related through displacement to achieve the periodicity, it becomes computationally challenging to solve the dispersion equation manually, in addition to the time required to assemble the matrices.

To this end, the finite element analyses (FEA) method will be used to solve the equation. COMOSL Multiphysics was selected to perform the numerical solution due to its ability to solve elastic wave equations and because the periodicity conditions can be automatically defined without manually identifying and matching every two opposite nodes on the surfaces of the unit cell. The first step in solving the dispersion equation is to verify the methodology used. To this end, two-unit cells proposed in the literature (Shi and Huang, 2013; and Chen et al., 2019) were selected to be regenerated, and the dispersion relation was verified against the published work.

The first unit cell was a 3D-3C unit cell, proposed by Shi and Huang, 2013, where the shape of the unit cell is a cube matrix, cube coating, and cube core, as shown in Figure 3-4.

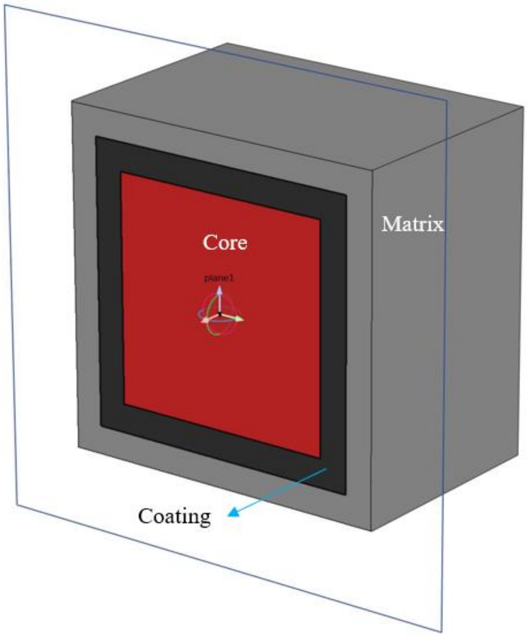

Figure 3-4: First 3D-3C unit cell used for verification.

The size of the matrix and coating side is 1.2 m and 0.2 m thickness; the coating side size is 1.0 m and 0.2 m thickness, and the core side size is 0.8 m. Periodic boundary conditions (PBC) were assigned to every two opposite sides along the unit cell, which translates to that the displacement on one surface of the unit cell equals the displacement on the parallel surface or that the unit cell is infinitely repeated in all directions as shown in Figure 3-5. It is worth mentioning that the PBC is only required to be assigned to the outer surfaces of the matrix.

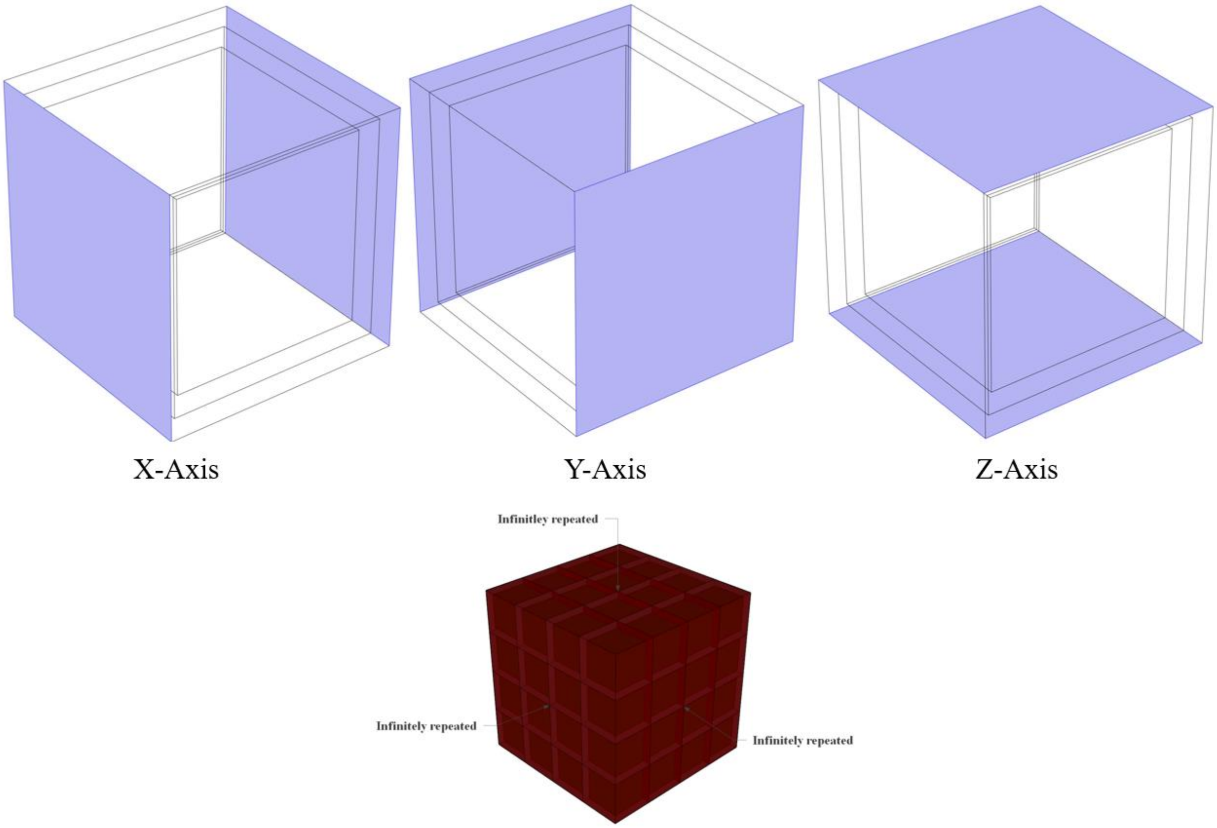

Figure 3-5: Assigned periodic boundary conditions along the unit cell - 1.

The unit cell materials were concrete, rubber, and steel for the matrix, coating, and core, respectively. Material properties are shown in Table 3-2.

Table 3-2: Material properties of the verified unit cell.

Material	Young's Modulus E (Pa)	Poisson's Ratio (v)	Density ρ (kg/m^3)
Concrete	30.0×10^9	0.200	2500
Rubber	1.37×10^5	0.463	1300
Steel	210×10^9	0.275	7890

In FEA, discretizing the unit cell and meshing it is an essential part, as it significantly affects the accuracy of the results. Therefore, quadratic Lagrange discretization with 3D tetrahedron elements was used to employ more than ten nodes per smallest wavelength (Moser et al., 1999; Yan et al., 2015; and Colquitt et al., 2017). The maximum mesh size can be calculated using Equation 3-21. In this dissertation, a typical mesh size used is 0.20m. The number of elements varies by the model size, however, an average of 225,000 elements were used in a typical model. ;.

$$Maximum\ Mesh\ Size = \frac{\lambda_s}{10} = \frac{v/f_m}{10} \qquad \text{Eq. 3-21}$$

Where λ_s is the smallest wavelength = shear wave velocity (v) / maximum frequency (f_m).

The solution to the dispersion equation can be found using the FIBZ, where the wave vector ***k*** is known (0 - 4.414), as explained in section 3.1.2. Thereafter, the FEA software will assemble the matrices and try to find a real solution at each wave vector ***k*** value (Sweeping wave vector values to find a solution).

Figure 3-6 shows the result from Shi and Huang, 2013, against the reproduced work (Current work). The resultant bandgap was identical in the reproduced work to the published work, with a slight variation in the smoothness of the curve due to some scaling along the wave vector that the authors implemented.

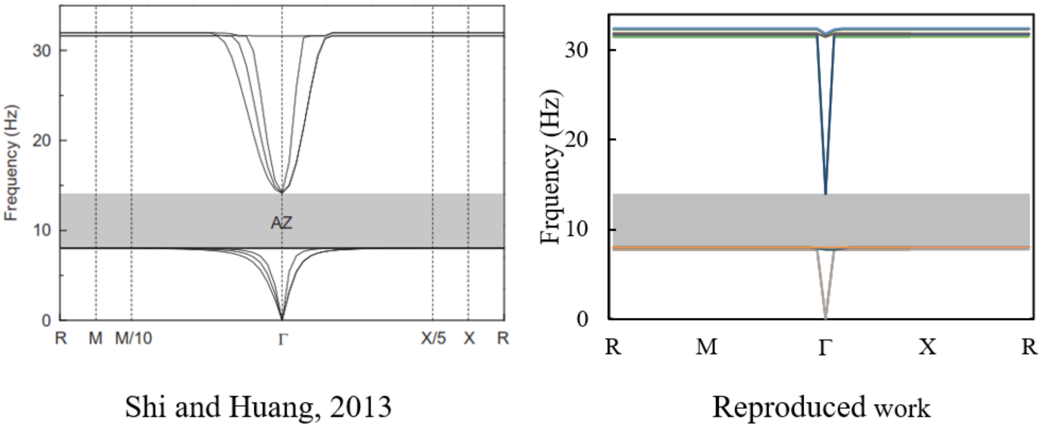

Figure 3-6: Verification of dispersion relation solution against published work - 1.

Furthermore, the work of Chen et al. (2019) was reproduced with the same approach. The difference is that the unit cell was made of a concrete pile core surrounded by a soil matrix. The radius of the pile is 1.2 m, the matrix side size is 3m, and an overall height of 6 m. The PBC was only assigned on the two vertical surfaces, as shown in Figure 3-7.

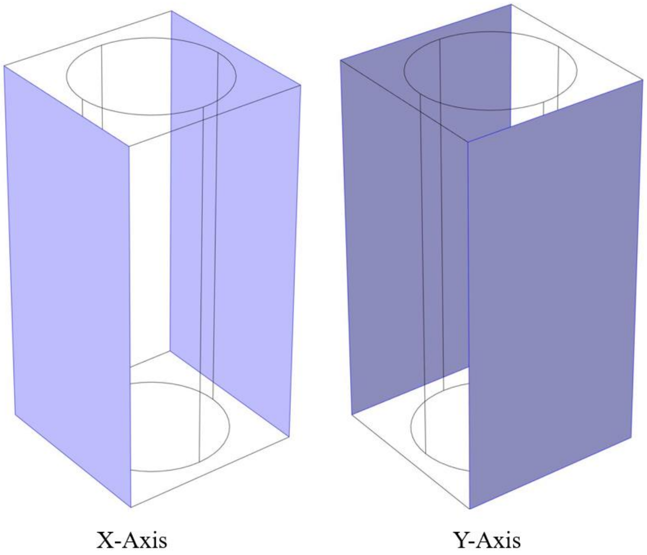

Figure 3-7: Assigned periodic boundary conditions along the unit cell - 2.

Figure 3-6 shows the results reported by Chen et al. (2019) against the reproduced work for methodological verification, where the results were identical. Furthermore, Figure 3-6 shows the global vibrational shapes at the symmetry points on the bandgap. The global vibrational modes correspond to guided lamb waves. Those modes are examined to prove that the destructive interferences are responsible for wave attenuation (Martincek, 1995; Zeng et al., 2019; and Zhang et al., 2021). The relative displacement (modal values obtained by vibrational modes) is maximum at the vertical edges of the unit cell and minimal elsewhere, while at the LBGL, the relative displacement is maximum at the corners and extends along the horizontal edges of the unit cell.

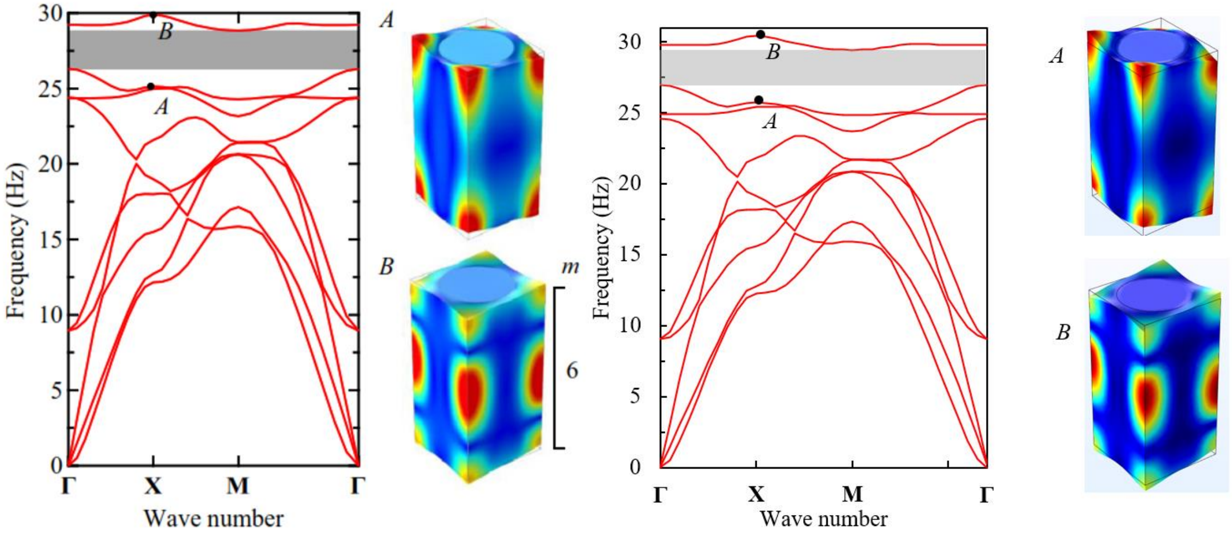

Chen et al., 2019

Reproduced work

Figure 3-8: Verification of dispersion relation solution against published work - 2.

3.3. Methodology for Identifying Bandgaps in the Frequency Domain-Reduced Model

After the unit cell is finalized, verifying that the bandgap can block the wave is necessary. In other words, the bandgap exists when limited number of unit cells are employed. To this end, a simplified FEA has been developed, which has been widely used in the literature (Chen et al., 2019; Zhang et al., 2021). Figure 3-9 shows a schematic of the developed simplified dynamic response model.

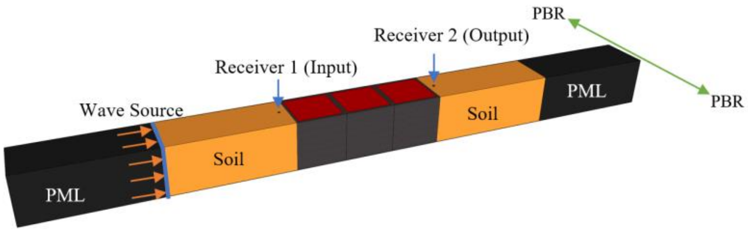

Figure 3-9: Simplified dynamic response model.

The benefit of using such a reduced model is to reduce the analysis cost and run as many models as possible with reduced cost. Although such a model is considered an ideal case, as the waves might travel underneath the unit cells, it will be sufficient to compare several unit cell configurations in a short period, and the most successful model will be evaluated using the full frequency domain mode (Section 3.4.). The model consists of two homogenous soils divided into two parts, homogenous soil and perfectly matched layers (PML). Both parts will use the same material (soft sand) with the same length, width, and depth; the only difference is the mesh type. Unit cells are arranged at the center of the soil medium with different configurations so that the number of cells in the X-direction represents the periodic condition in that direction.

Furthermore, PBC was assigned at the vertical edges of the model (in the out-of-plane direction). Quadratic Lagrange discretization with 3D tetrahedron elements was used to employ more than ten nodes per smallest wavelength (Moser et al., 1999; Yan et al., 2015; and Colquitt et al., 2017). The maximum mesh size can be calculated using Equation 3-22. Figure 3-10 shows the model mesh with an average of 0.3m maximum size, resulting in a total number of 190,000 elements.

$$Maximum\ Mesh\ Size = \frac{\lambda_s}{10} = \frac{v/f_m}{10} \qquad \text{Eq. 3-22}$$

Where λ_s is the smallest wavelength = shear wave velocity (v) / maximum frequency (f_m).

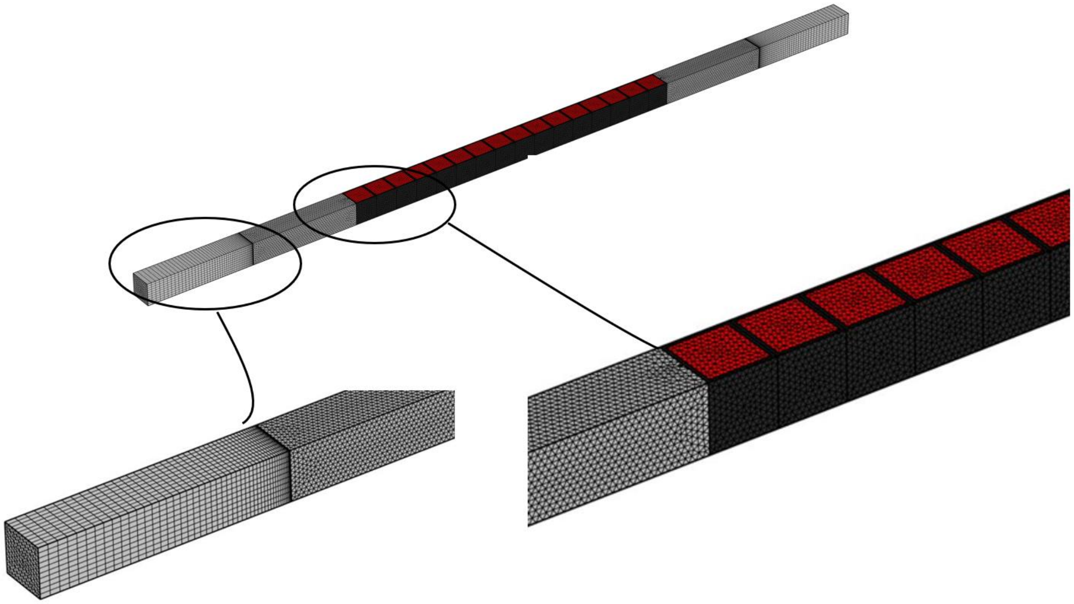

Figure 3-10: Dynamic response model mesh.

Low-amplitude harmonic displacement is applied at the interface between the homogeneous soil and the PML. Two receiver points are defined in the mode to determine the transmission of the unit cell configurations. Receiver 1 (input node) records the input energy, displacement, velocity, or acceleration of the seismic waves, and receiver 2 (output node) records the transmitted displacement, energy, velocity, or acceleration through the unit cell. Thereafter, the transmission can be calculated using Equation 3-23.

$$Transmission\ (dB) = 20\ x\ log(\frac{Output}{Input}) \qquad \text{Eq. 3-23}$$

where input and output can be energy, displacement, velocity, or acceleration at the two receiver points. Equation 3-15 is the governing equation along with the Floquet-Bloch periodic conditions (Equation 3-16). In COMSOL Multiphysics, there are two options for wave equations boundary conditions: low-reflecting boundaries (LRB) and perfectly matched layers (PML). Both conditions can absorb the incoming waves and prevent unnecessary wave reflection from the boundaries. PML is an imaginary boundary with a thickness that extends depending on the wavelength (COMSOL documentation). For instance, if the frequency is 1 Hz, the physical depth of the PML would remain constant; however, the scaling factor equals the wavelength that extends the depth of the PML to that wavelength. PML allows the wave to propagate within its layers; as the waves propagate, they decay and disappear due to the density of the PML mesh in the first layers preventing it from reaching the edge and reflecting back to the domain.

LRB serves the same purpose as the PML. However, LRB takes the material properties as defined and creates a perfect impedance match for pressure and shear waves. LRB effectiveness depends on the direction of the incoming waves, and they work best when the waves are perpendicular to the LRB. LRB uses damping to prevent any unnecessary wave reflection from the FEA boundaries.

To verify the dynamic response methodology used in this research, it is necessary to validate the results with existing published work. To this end, the work of Zhang et al. (2021), has been reproduced using the methodology explained above.

Figure 3-11 shows the selected unit cell by the authors where the unit cell is 2D-2D with soil matrix and steel core and a size of 10 m. The modulus of elasticity, density and Poisson’s ratio for the soil was considered as 30 MPa, 1800 kg/m^3 and 0.3, respectively; while those of steel are , 210 × GPa, , 7850 kg/m^3, and 0.3, respectively.

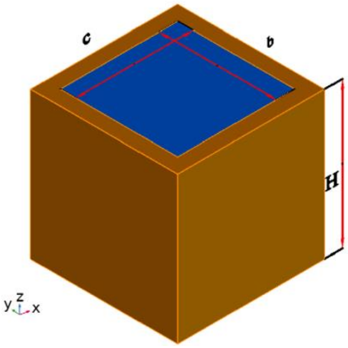

Figure 3-11: The unit cell from the literature (Zhang et al., 2021) used for verification of the reduced model methodology.

Thereafter, the dynamic response (Transmission curve) is obtained using the methodology explained above. Figure 3-12 shows the dynamic response (Displacement response) at 9 Hz taken from the literature and the reproduced work, which shows a great match between the literature and the reproduced work. Furthermore, Figure 3-13 shows the published and reproduced work transmission, which shows a great match with the published work, and therefore the methodology proposed in the section is valid and can be used for further development of the unit cell configurations.

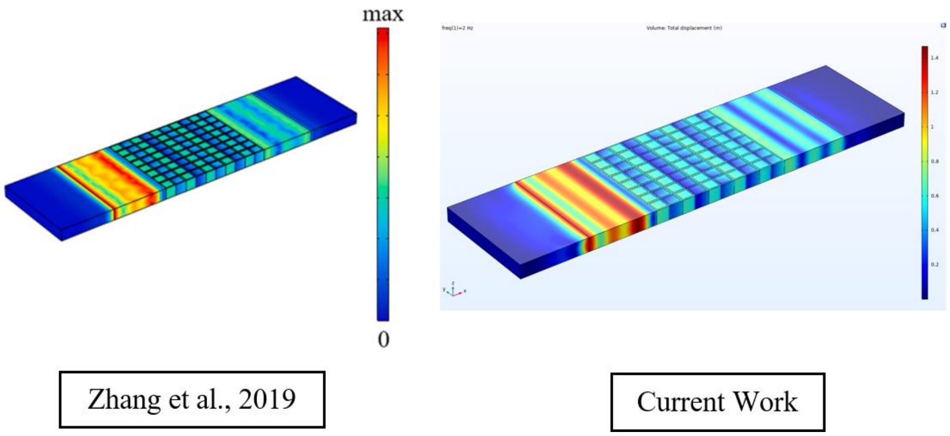

Zhang et al., 2019

Current Work

Figure 3-12: Verification of dynamic response of the soil medium at 9 Hz frequency.

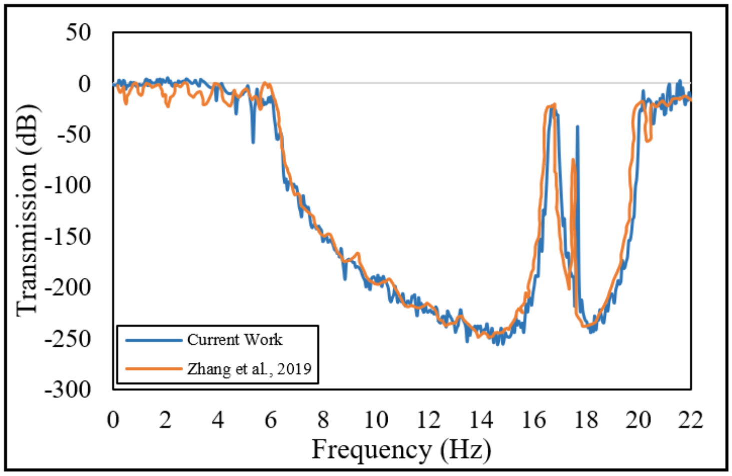

Figure 3-13: Verification of transmission of the proposed methodology.

It is worth mentioning that the transmission is obtained by recording the incoming and outgoing wave energy, displacement, velocity, or acceleration at receiver points 1 and 2. Using Equation 3-22, the transmission can be found at each frequency.

3.4. Methodology for Identifying Bandgaps in the Frequency Domain-Full Model

In a similar manner to section 3.3., The dynamic response of a structure can be evaluated in FEA using a large soil medium where the unit cells are embedded in this medium. It is also necessary to evaluate the performance of unit cell configuration in such a large model since the unit cells will eventually be buried and embedded within the soil.

Figure 3-14 shows the full model for the analyses in the frequency domain, where the model consists of a large soil medium surrounded by PML on two vertical sides and at the bottom. Additionally, LRBs were assigned to the external interfaces of the PML to ensure that no waves were reflected to the medium from the boundaries. The unit cells are arranged and embedded in the soil, and two receiver points are assigned to capture the incoming and outgoing energy, displacement, velocity, or acceleration.

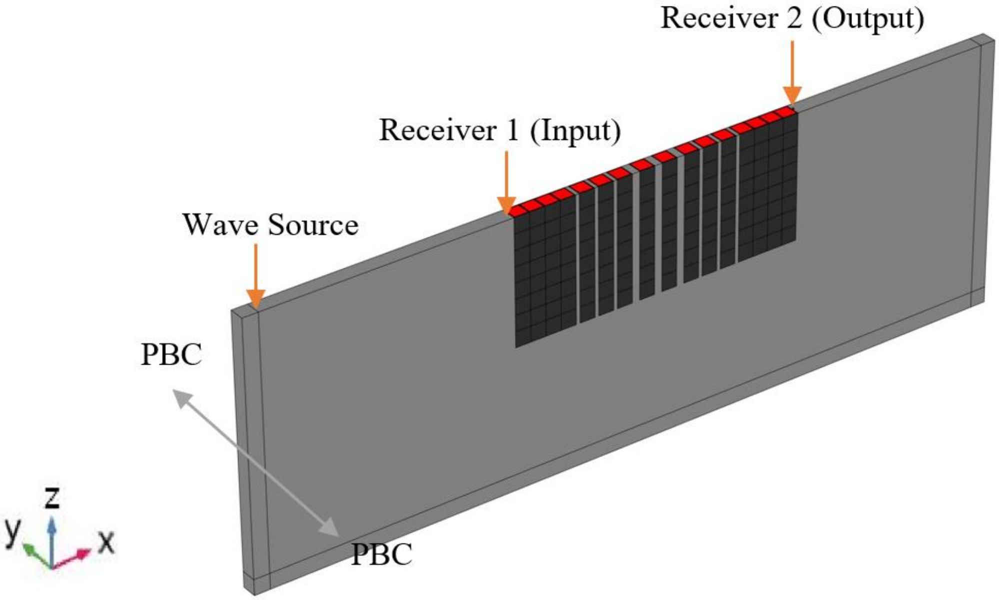

Figure 3-14: Dynamic response full model.

PBC was assigned to the vertical surfaces of the soil medium and the unit cells along the Y-axis. The dimensions and size of the unit cell were related to the lattice constant (a) of the unit cell, where the length of the model, the thickness out of plane and height of is 48a, and 16a, respectively. The maximum wavelength for the selected soil is 679 m at frequency of 0.1 Hz. However, the wavelength significantly decreases to 67.9 m at 1 Hz. Since the ultra-low frequencies (0.1-1 Hz) are not the main focal point of this dissertation, 48a soil size is sufficient for the waves to propagate through the soil. The unit cells are arranged and placed at the center of the medium at a distance of 16a away from the vibration source. Figure 3-15 shows the dimensions and configuration of the full model used in the frequency domain analyses.

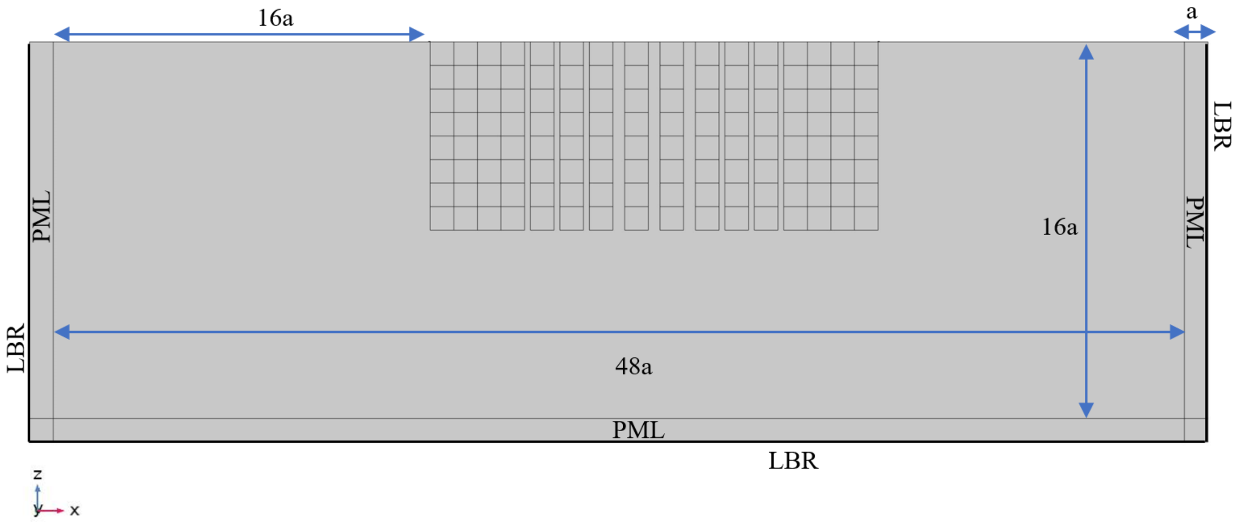

Figure 3-15: Dimensions and configurations of the full-scale dynamic response model.

The PML thickness is set as *a*. However, the PML defined thickness does not play a role in the frequency domain analyses due to the stretching factor assigned, so that the formulation will include a thickness equal to the wavelength of the studied frequency. The wave is applied as a low-amplitude harmonic displacement on the edge between the homogenous soil and the PML at the left side of the model to generate surface waves and applied at the interface between the homogenous soil and the PML to the left side of the model to generate compressional waves.

Like the reduced model, quadratic Lagrange discretization with 3D tetrahedron elements was used to employ more than ten nodes per smallest wavelength (Moser et al., 1999; Yan et al., 2015; and Colquitt et al., 2017). The maximum mesh size can be calculated using Equation 3-24. Figure 3-15 shows the model mesh. The shortest wavelength is 2.26 m at 30 Hz and the average used mesh size is 0.25 m, which allows each frequency to propagate through at least 9 elements.

$$Maximum\ Mesh\ Size = \frac{\lambda_s}{10} = \frac{v/f_m}{10} \qquad \text{Eq. 3-24}$$

where λ_s is the smallest wavelength = shear wave velocity (v) / maximum frequency (f_m).

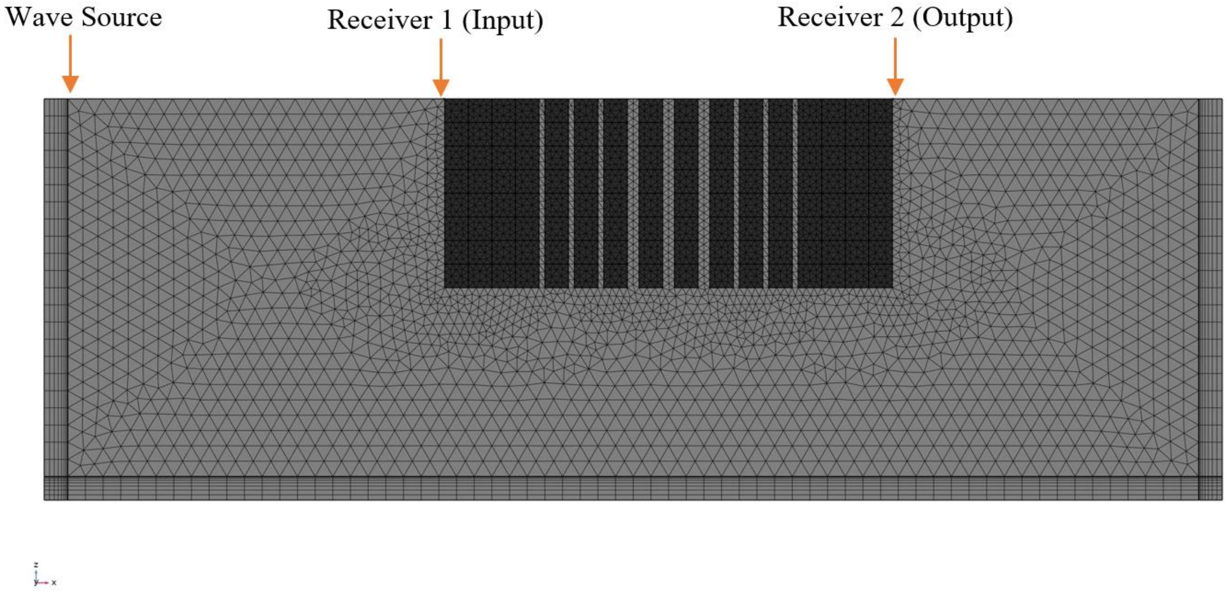

Figure 3-16: Mesh of the full-scale dynamic response analyses.

Finally, the transmission between receivers 1 and 2 will be used to evaluate the performance of the final selected unit cell configurations (Equation 3-23).

3.5. Methodology of Evaluating the Performance of the Unit Cells in the Time Domain

Finally, time domain analysis is the final evaluation step to ensure that the metabarriers can attenuate seismic waves. To this end, a larger soil medium was developed, as shown in Figure 3-17. The model included a single degree of freedom structure (SDOF) to evaluate the peak resonance frequency. The length of the soil medium is 75a, where a is the lattice constant, depth of a, and height of 35a. the SDOF is placed at a distance of 35a. The maximum wavelength for the selected soil is 679 m at frequency of 0.1 Hz. However, the wavelength significantly decreases to 67.9 m at 1 Hz. Since the ultra-low frequencies (0.1-1 Hz) are not the main focal point of this dissertation, 48a soil size is sufficient for the waves to propagate through the soil. The wave source was applied as vertical low-amplitude displacement at a distance of λ_s : the smallest wavelength of the applied frequencies.

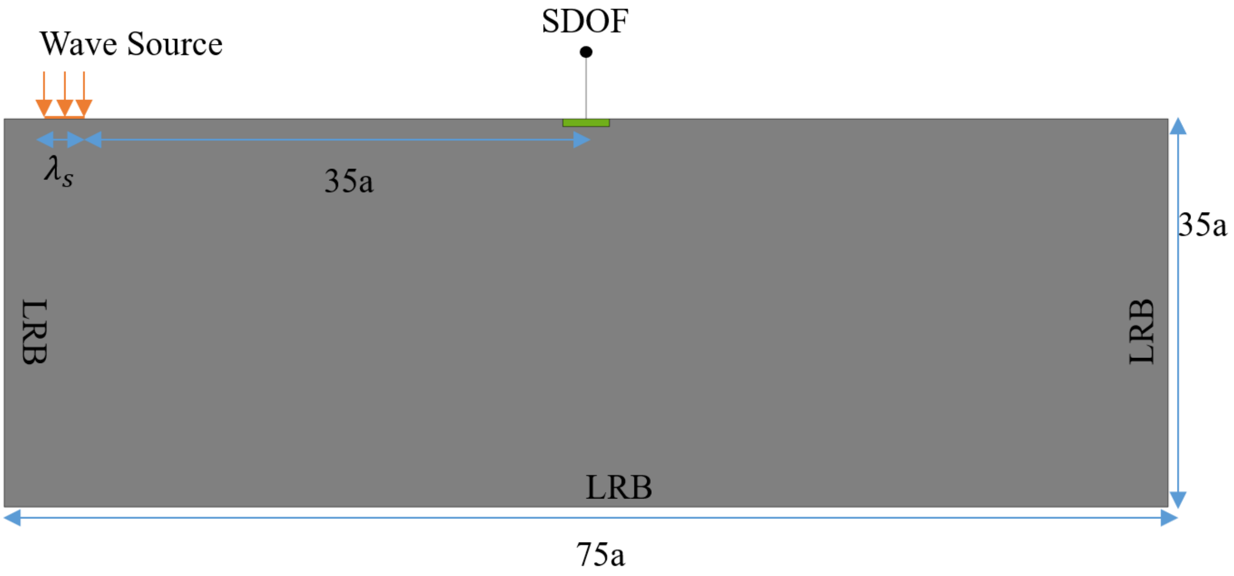

Figure 3-17: Time domain full-scale model.

Free tetrahedral elements were used to mesh the model with maximum mesh size as shown in Equations 3-25, 3-26, and 3-27

$$Max\ mesh\ size = \frac{\lambda_s}{4} = \frac{C_s}{4f_m} \quad \text{Eq. 3-25}$$

$$Shear\ wave\ speed,\ C_s = \sqrt{\frac{G}{\rho}} \quad \text{Eq. 3-26}$$

$$Time\ step\ size = \frac{1}{60f_m} \quad \text{Eq. 3-27}$$

Where λ_s is the minimum wavelength, C_s is the lowest shear wave speed, and f_m is the highest frequency. Such mesh and time step sizes are used to ensure a minimum of 4 elements per wavelength and that no frequency is skipped at any given time step. The literature employs and recommends such limitations (Palermo et al., 2018; Muhammad et al., 2021; and Maheshwari and Rajagopal, 2022). LRB is applied at the soil medium boundaries to prevent wave reflection since PML stretching factor is not implemented in the formulation of FEA in the time domain and for the PML to be effective, its physical length must be the same as the longest wavelength which makes the analysis inefficient, if implemented.

To evaluate the unit cell configurations capabilities, three different time histories were used as wave sources as follows:

1. Ormsby wavelet is given by Equation 3-28, and it can be used to generate multiple frequencies in a short time. It is defined by four frequencies: Low cut-off frequency, low passing frequency, high passing frequency, and high cut-off frequency. Figure 3-18 shows the Ormsby wavelet amplitude, and the Fourier transform functions.

$$Ormsby\ Wavelet = \frac{\pi f_4^2}{f_4 - f_3} sinc^2(\pi f_4 t) - \frac{\pi f_3^2}{f_4 - f_3} sinc^2(\pi f_3 t) - \frac{\pi f_2^2}{f_2 - f_1} sinc^2(\pi f_2 t) + \frac{\pi f_1^2}{f_2 - f_1} sinc^2(\pi f_1 t) \qquad \text{Eq. 3-28}$$

Where f_4, f_3, f_2, and f_1 are 30 Hz, 27.5 Hz, 2.5 Hz, and 0.1 Hz, t is the time.

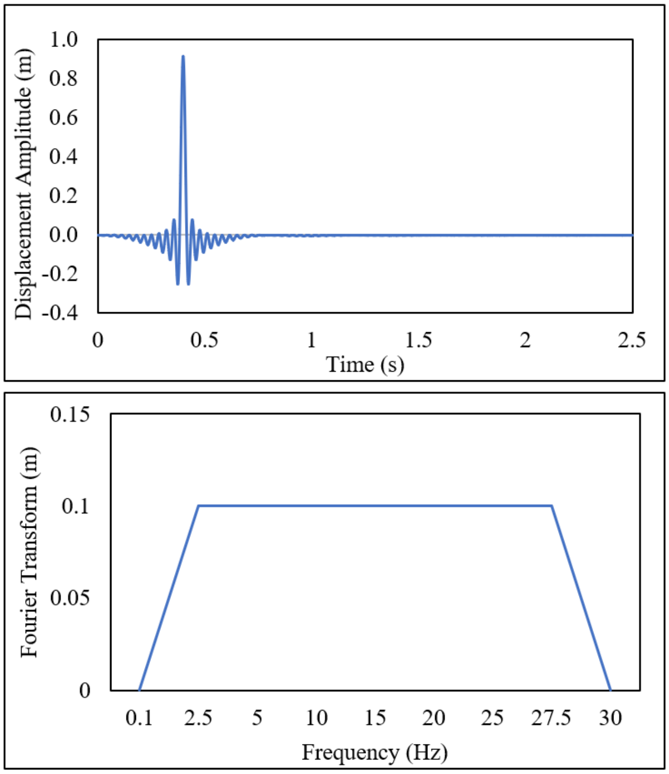

Figure 3-18: Applied Ormsby wavelet and its Fourier transform function.

2. Ricker wavelet is given by Equation 3-29, and it is used because it is focused on a peak frequency that can generate a seismic wave with a peak frequency equal to the structure's peak resonance frequency. It is defined by max frequency (f_m). Figure 3-19 shows the Ricker wavelet amplitude and Fourier transform functions.

$$Ricker\ Wavelet = (1 - 2\pi^2 f_m^2 t^2)e^{-\pi^2 f_m^2 t^2} \qquad \text{Eq. 3-29}$$

Where f_m is the peak frequency, and t is the time.

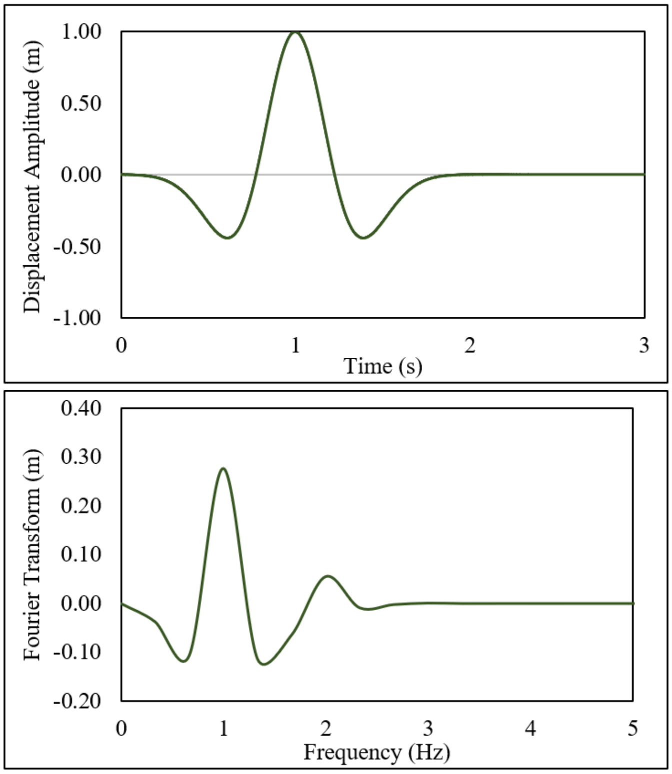

Figure 3-19: Ricker wavelet and its Fourier transform function.

3. Actual seismic event data, at the 1975 Oroville dam earthquake recorded at Johnson Ranch station. Figure 3-20 shows the amplitude of the seismic event wave and Fourier transform function. The data have been extracted from the peer ground motion database and were used in this analysis to evaluate the performance of the unit cell configurations against a real-life recorded seismic event.

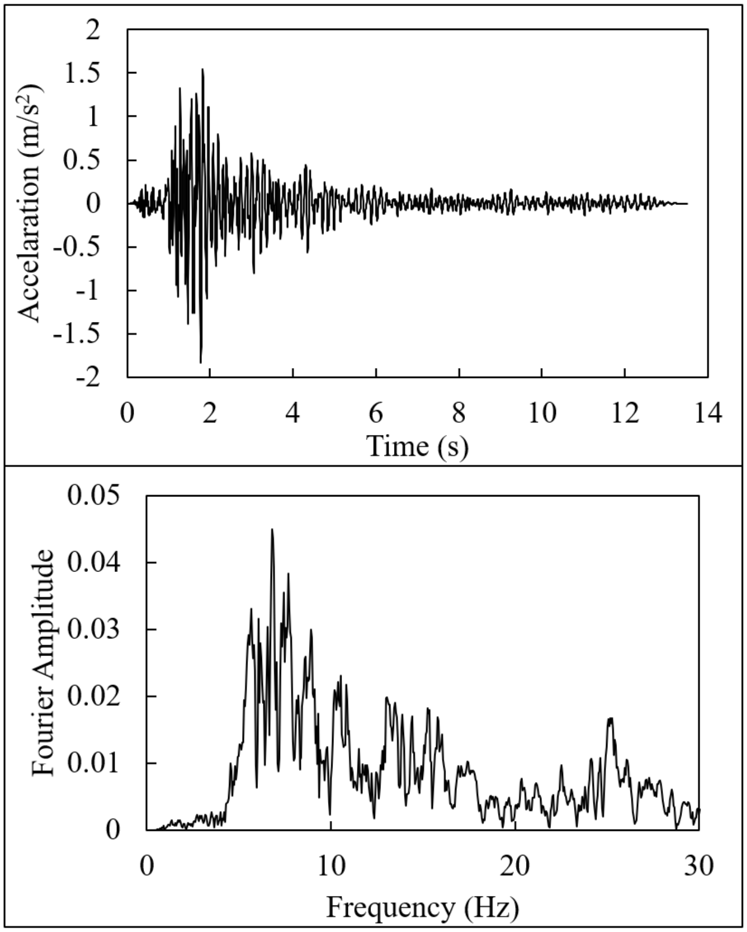

Figure 3-20: 1975 Oroville dam earthquake, California recorded seismic wave acceleration time histories and its Fourier transform function.

The methodology and settings of the time history analysis has been verified with the existing literature, specifically Muhammad et al. (2021). However, due to difficulties obtaining the exact data used in the publication, the reproduced work is slightly different in magnitude, but the overall observations are the same.

Figure 3-21 shows the published work FEA, where a unit cell embedded in the soil is subjected to 1975 Oroville dam earthquake. The model size is approximated to the lattice constant of the unit cell in addition to the minimum wavelength. 1975 Oroville dam earthquake (Shown in Figure 3-

20) is applied in the vertical direction (Z-axis) with the input and output probes to record the wave accelerations. Although the published work evaluated the analysis to 40 seconds, the reproduced work is up to 6 seconds to reduce the analysis cost. Mesh size and time steps are used as shown in Equations 3-25, 3-26, and 3-27.

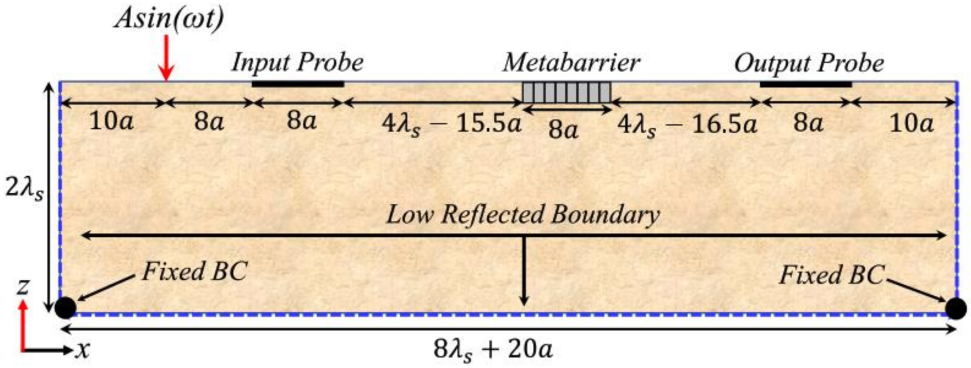

Figure 3-21: Time transient analysis FEA (Muhammad et al., 2021).

Figure 3-22 compares the published work (Right) and the reproduced work (Left). Overall, there is a significant reduction in the wave amplitude between input and output probes, and only the peak amplitudes were different due to data availability.

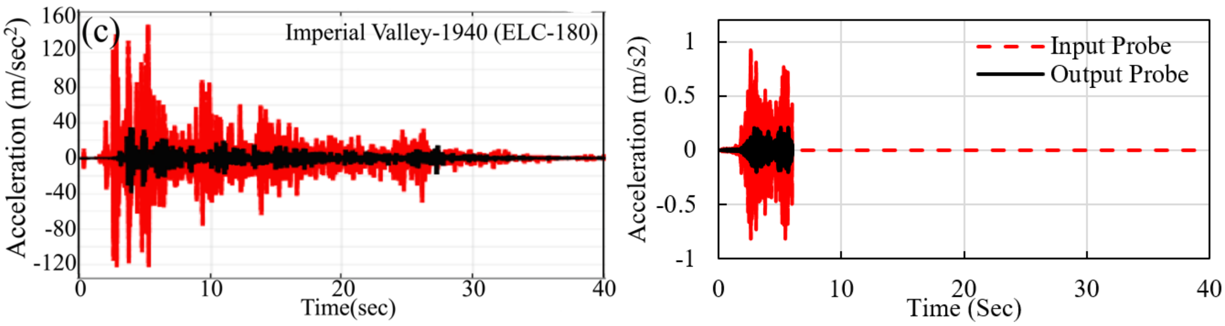

Figure 3-22: Time transient analysis results comparison, published work (Left), and current work (Left).

3.6. Parametric Studies

This section presents the investigated properties and development of unit cells and configurations to manipulate the bandgap without change in the unit cell properties.

3.6.1. Development of Single Unit cell

The first step in developing meta-barriers is to develop a unit cell with the broadest possible bandgap. The dispersion equation will be used to find the dispersion relation of each studied unit cell. To this end, the geometry of the unit cell will be studied. The geometry includes the shape of the unit cell and its components. The study includes 2D and 3D unit cells with various geometric combinations such as but not limited to blocks, spheres, honeycombs, cylinders, and irregular shapes (rectangular). This study will yield the best possible unit cell geometry with the widest bandgap. The only variable parameter in this parametric study is the geometric arrangement of the unit cell. At the same time, the size remains constant in all the studied models. Moreover, common construction materials such as concrete, rubber, and steel will be used and will remain constant across all studied models. This approach should enable a head-to-head comparison between various studied unit cells.

The number of layers a unit cell can be assembled from will be studied thereafter. This parametric study will attempt to widen the bandgap of the selected final geometry without changing any of the material properties and the size of the unit cell. To this end, four types of unit cells will be investigated, as shown in Figure 3-23.

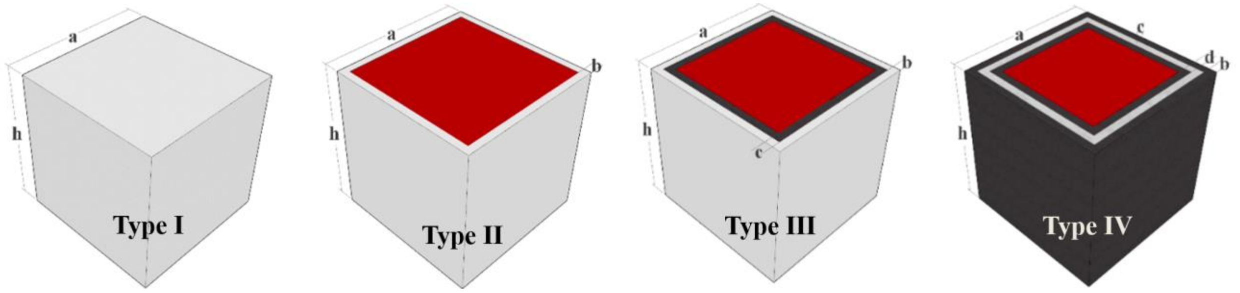

Figure 3-23: Unit cell types used for the number of layers parametric study.

Type I is a single-material unit cell; it represents individual materials that were selected to comprise the unit cell. This type will ensure that no material can block specific frequencies by itself. Type II is a 2D-2C unit cell with two material layers (matrix and core), and PBC is applied at the four vertical sides of the unit cell. Type III is a 2D-3C unit cell, where the unit cell has a matrix, coating, and core with three different material layers. The PBC was applied at the vertical sides of the unit cell while the top and bottom sides remained traction free. Finally, type IV unit cell is a 2D-4C unit cell with four material layers, and the PBC is applied at the four vertical sides while the top and bottom sides are traction free. The lattice constant is 2 m in all cases, and the thickness of each layer remained constant at 0.9a, 0.8a, and 0.7a for layers 2 through 3, respectively. Table 3-3 shows the material properties used in the number of layers parametric studies. All the materials are common construction materials apart from Tungsten which was used due to its extremely high density.

Table 3-3: Material properties for the number of layers parametric study.

Material	Young's Modulus E (Pa)	Poisson's Ratio (v)	Density ρ (kg/m^3)
Concrete	30.0×10^9	0.200	2500
Rubber	1.37×10^5	0.463	1300
Soil	20.0×10^6	0.300	1800
Steel	210×10^9	0.275	7890
CFRP	39.2×10^9	0.200	1900
Tungsten	410×10^9	0.250	17500

Thereafter, the unit cell mechanical properties are investigated, including core modulus of elasticity, E (Pa), density, ρ (kg/m^3), and their effects on the attenuation zone. To this end, type II unit cell is used, and several models are studied where all mechanical properties of the matrix and the core are constants, and with multiple E and ρ, and the results are compared for each case. Tables 3-4 and 3-5 summarize the core properties of parametric studies.

Table 3-4: Modulus of elasticity of the core parametric study for type II unit cell.

Layer	Modulus of Elasticity, E (Pa)	Poisson's Ratio	Density, ρ (kg/m^3)	Size (m)
Matrix	1.37×10^5	0.463	1300	2.0
Core	Variable	0.275	7890	0.9a

Table 3-5: Density of the core parametric study for type II unit cell.

Layer	Modulus of Elasticity, E (Pa)	Poisson's Ratio	Density, ρ (kg/m^3)	Size (m)
Matrix	1.37×10^5	0.463	1300	2.0
Core	210×10^9	0.275	Variable	0.9a

Thereafter, the modulus of elasticity, E (Pa), and the density, ρ (kg/m^3) of the unit cell matrix, have been investigated using four different materials with properties as shown in Table 3-6.

Table 3-6: Materials used for the unit cell-matrix mechanical properties.

Matrix Material	Young's Modulus E (Pa)	Poisson's Ratio (v)	Density ρ (kg/m^3)
Concrete	30.0×10^9	0.200	2500
Steel	210×10^9	0.275	7890
CFRP	39.2×10^9	0.200	1900
Tungsten	410×10^9	0.250	17500

Finally, the size of type II and type III unit cells core have been investigated, and the size of the cores has been related to the overall size of the unit cell. In this parametric study, the effects of the core size on the bandgap are investigated using several sizes starting as low as 0.4a and up to 0.9a. The final unit cell with the lowest-widest possible bandgap will be selected afterward. Moreover, a simplified spring-mass-spring model will be developed to simplify the bandgap bounds calculation process.

3.6.2. Bandgap Manipulation Using Unit Cells Configuration Parametric Study

This section will verify the bandgap existence using the transmission in the reduced-frequency domain (Section 3.3). Furthermore, multiple unit cell arrangements will be studied. Such configurations are inspired by linear chirped configuration (LCFBG) used in microwave photonics (Shahoei et al., 2012). The linear chirped, shown in Figure 3-24, can manipulate the amplitude of microwaves due to their linear arrangement. The same principle will be adopted and scaled to manipulate seismic waves.

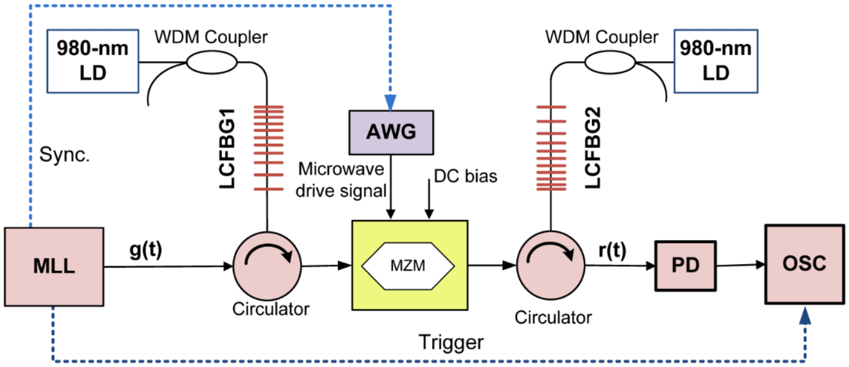

Figure 3-24: Linear chirped configuration used in microwaves (Shahoei et al., 2012).

To this end, several unit cell configurations will be modeled, and their effects on the bandgap will be verified. Figure 3-25 shows the proposed configurations that will be investigated.

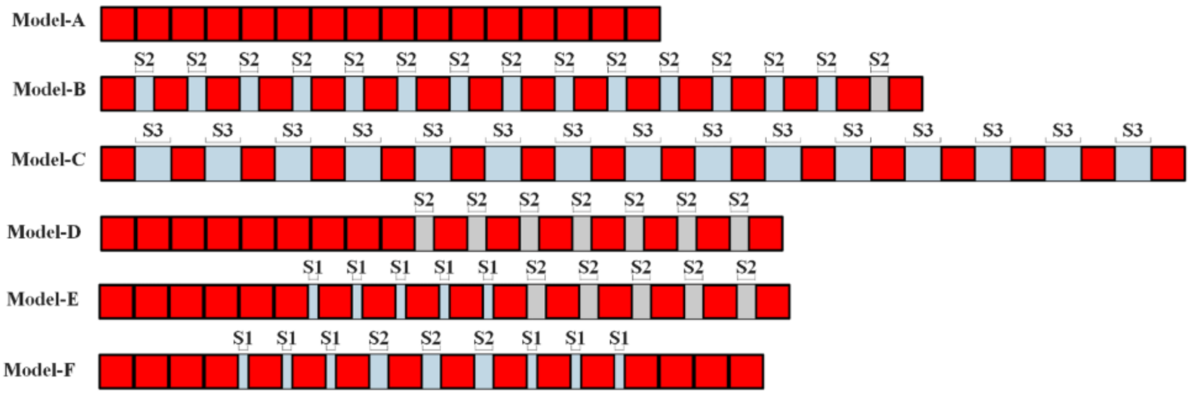

Figure 3-25: Proposed unit cell configurations for bandgap manipulation.

Model-A represents a typical unit cell configuration where the unit cells are arranged back-to-back. This model simulates a periodic unit cell in two directions. Models-B and C have uniformly spaced configurations where the unit cells are arranged uniformly. Models-D and E are a single-graded configuration with the starting unit cells arranged back-to-back, and the remaining are uniformly spaced.

Finally, Model-F represents a double-graded configuration where the starting cells are back-to-back, then uniform spacing, then increased uniform spacing, then decreased spacing, and finally, a back-to-back arranged cell.

Once all the proposed models are analyzed, the one with the broadest bandgap will be selected for verification in the full-scale dynamic response study. Thereafter, the selected configuration will be used to study its effects in the full frequency and time domain studies.

Finally, supplemental studies on the ability of the PML to absorb incoming waves and the size of the soil medium that affect wave propagation are presented to validate and evaluate additional FEA parameters, as shown in Appendix B.

CHAPTER 4 : RESULTS AND DISCUSSION

This chapter will present the results of the parametric studies discussed in Chapter 3 and provide insight on bandgap manipulation without changing the unit cell combination.

4.1. Development of Unit Cell

This section aims to finalize a unit cell configuration with the broadest possible bandgap. To this end, several parametric studies were conducted, including geometry, mechanical properties, and unit cell size. In all parametric studies, some assumptions were kept constant such as:

1. Materials are assumed to be linear elastic materials.
2. Bonds between materials are assumed to be perfect so that the unit cell would act as a single unit.
3. Periodic boundary conditions were assumed on every two opposite sides of the unit cell.

To find the best possible configuration, the shape of the unit cell was analyzed using several shapes and combinations, multiple unit cell materials, and layers combinations. Moreover, the mechanical properties of the unit cell matrix and core were investigated, and the size of the unit cell core was studied. Finally, the final proposed unit cell materials and size combination were presented along with the resultant bandgap, which will be developed to manipulate the bandgap without interfering with the unit cell combinations.

The main objective of this section is to find the best possible unit cell combinations with the broadest possible bandgap.

4.1.1. Unit Cell Geometry Parametric Study

The first step in finding the best possible unit cell configuration is to find the best possible geometry combination. With the same approach, as explained in section 3.2. several geometries were investigated, including cubes, cylinders, spheres, honeycombs, and nonuniform shapes (as shown in Appendix A). A 3D-3C unit cell was selected with a constant overall size. The lattice constant (a) =1 m, 0.8a is the size of the coating, and 0.4a is the size of the core. Common construction materials were used and were kept constant across this study. Table 4-1 shows the selected materials and their properties. PBC was assigned on every two opposite sides of the unit cell. Figure 4-1 shows the PBC for one of the investigated unit cells, and the same approach was used for the remaining investigated geometries. Table 4-2 shows the standard settings used across different investigated geometries. The dispersion equation has been solved by sweeping the wave vector along the FIBZ, as explained in section 3.1.2. The periodic equation, expressed by the wave vector $\boldsymbol{k}$, is swept between the X, Y, and Z directions to cover the edges of the first irreducible Brillouin zone. Therefore, a parametric sweep was defined in COMOSL to sweep the wave vector k from 0 to 4.414 with $\frac{\pi}{a}$ step reflecting the wave number, where a is the lattice constant, and the variables k_x, $k_{y,}$ and k_z were related to K, as shown in Table 4-3.

Table 4-1: Selected materials for the unit cell geometry parametric study.

Layer	Material	Young's Modulus E (Pa)	Poisson's Ratio (v)	Density ρ (kg/m^3)
Matrix	Concrete	30.0×10^9	0.200	2500
Coating	Rubber	1.37×10^5	0.463	1300
Core	Steel	210×10^9	0.275	7890

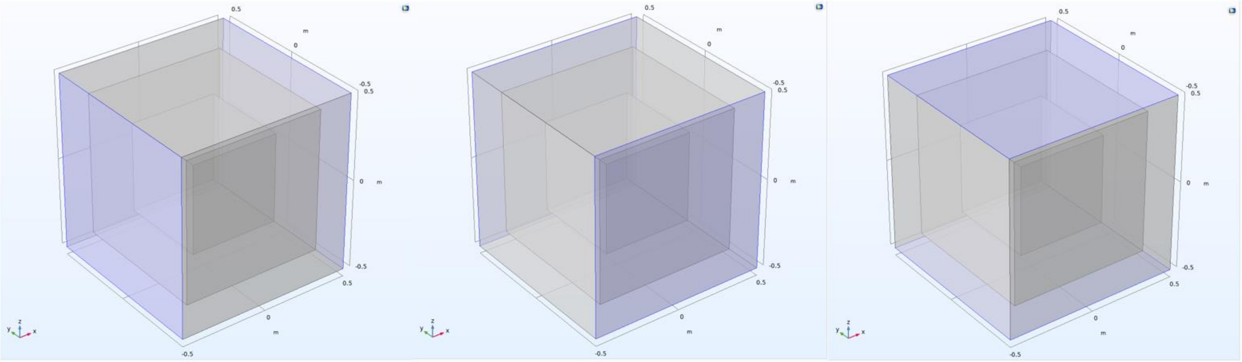

Figure 4-1: Assigned PBC for a 3D-3C unit cell.

Table 4-2: Common settings for the unit cell geometry parametric study.

Layer	Material	Size
Matrix	Concrete	1.0 m
Coating	Rubber	0.8 m
Core	Steel	0.4 m

Table 4-3: Wave vector (**k**) definition using its components.

Wave Number (K)	k_x	k_y	k_z
$0<k<1$	$\frac{\pi}{a}$	$\frac{\pi}{a}$	$(1-k)\times\frac{\pi}{a}$
$1<k<2$	$(2-k)\times\frac{\pi}{a}$	$(2-k)\times\frac{\pi}{a}$	0
$2<k<3$	$(k-2)\times\frac{\pi}{a}$	0	0
$3<k$	$\frac{\pi}{a}$	$(k-3)\times\frac{\pi}{a}$	$(k-3)\times\frac{\pi}{a}$

In this section, only the most suitable unit cell geometries are presented. However, several other geometries were investigated, and their results are shown in Appendix A. Such geometries had 0 to very small bandgap. For instance, a unit cell with two different side lengths (Rectangular shape) was investigated, and the results showed that symmetry along its faces is one of the most important factors in bandgap presence.

Figures 4-2 and 4-3 show the investigated geometries that could be selected as a final unit cell. The unit cells included three cubes (Model-1), two cubes and a cylinder core (Model-2), Two cubes and a sphere core (Model-3), a cube matrix and two spheres (Model-4), and a cube matrix with two cylinders (Model-5). It is worth mentioning that the size of the coating and the matrix have been adjusted with each model so that the weight of the coating and the core is constant across all models. The overall size of the unit cell was constant in all the models.

The observed bandgap for each of the investigated unit cells is shown in Table 4-4. The observed LBGLs were 7.9 Hz, 8.5 Hz, 7.0 Hz, 9.5 Hz, and 9.5 Hz for models 1 through 5, respectively. The observed UBGLs were 11.6 Hz, 11.5 Hz, 9.0 Hz, 11.9 Hz, and 12.5 Hz for models 1 to 5, respectively. Furthermore, the bandgap width (BGW) observed for models 1 to 5 are 3.7 Hz, 3.0 Hz, 2.0 Hz, 2.4 Hz, and 3.0 Hz.

The widest observed bandgap was for a unit cell with cube matrix, cube coating, and cube core (Model-1) with a 3.7 Hz width, Models 2 and 3 bandgap widths were 3.0 Hz. Since the investigated unit cells had identical size and material properties, the unit cell with three cubes (Model-1) is the best possible geometry in terms of bandgap width. Although Model-3 LBGL was lower than Model-1 (7.0 Hz compared to 7.9 Hz), model-1 was selected as a final configuration in terms of geometry because it had the broadest possible bandgap. Figure 4-4 shows the BGW, LBGL, and UBGL for the main investigated models.

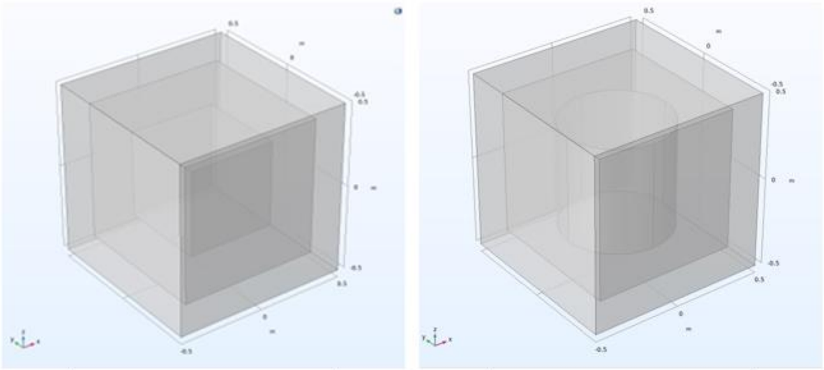

Model-1

Model-2

Figure 4-2: Unit cells selected for geometric properties parametric study.

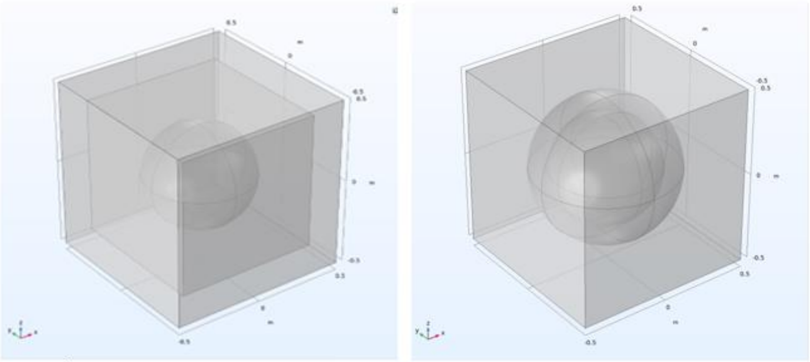

Model-3

Model-4

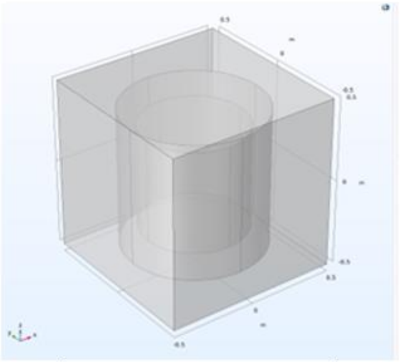

Model-5

Figure 4-3: Unit cells selected for geometric properties parametric study.

Table 4-4: Unit cell geometry parametric study results for the main investigated models.

Model No.	Matrix Shape	Coating Shape	Core Shape	LBGL (Hz)	UBGL (Hz)	BGW (Hz)
1	Cube	Cube	Cube	7.9	11.6	3.7
2	Cube	Cube	Cylinder	8.5	11.5	3.0
3	Cube	Cube	Sphere	7.0	9.0	2.0
4	Cube	Sphere	Sphere	9.5	11.9	2.4
5	Cube	Cylinder	Cylinder	9.5	12.5	3.0

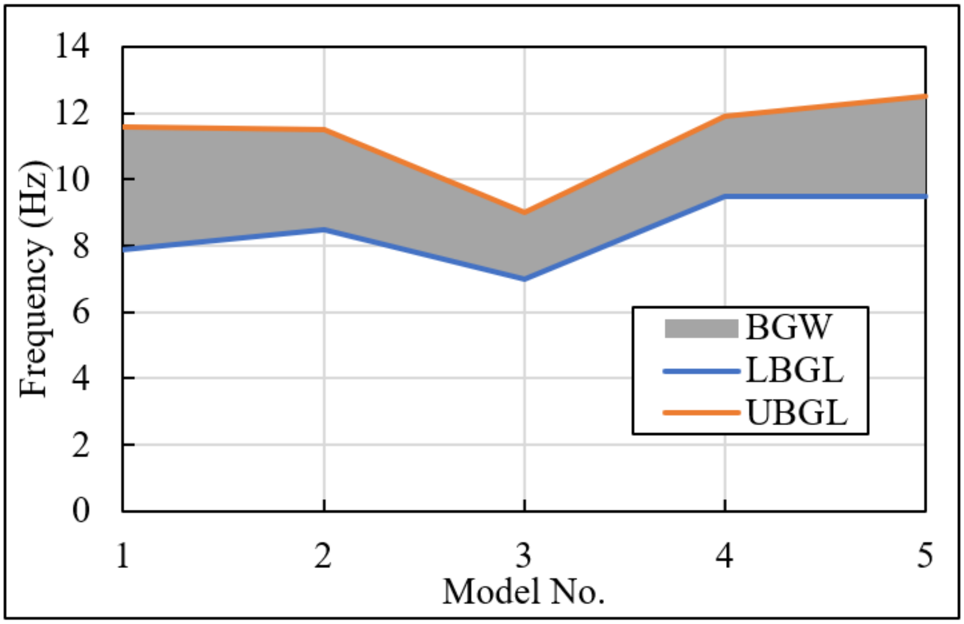

Figure 4-4: Bandgap width versus model number for geometry parametric study.

Figures 4-5 and 4-6 show the dispersion relation for each of the main investigated models in the parametric geometry study.

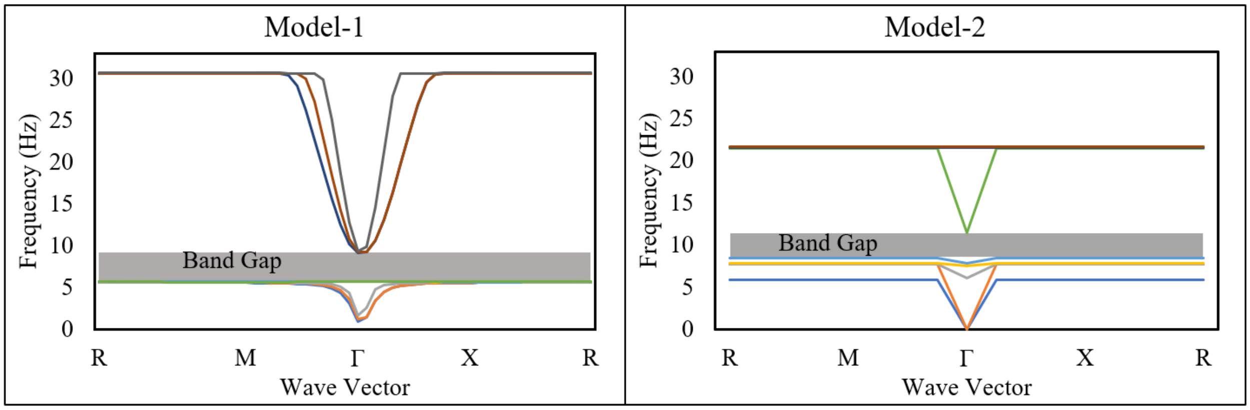

Figure 4-5: Bandgap for models 1 and 2 for parametric geometry study.

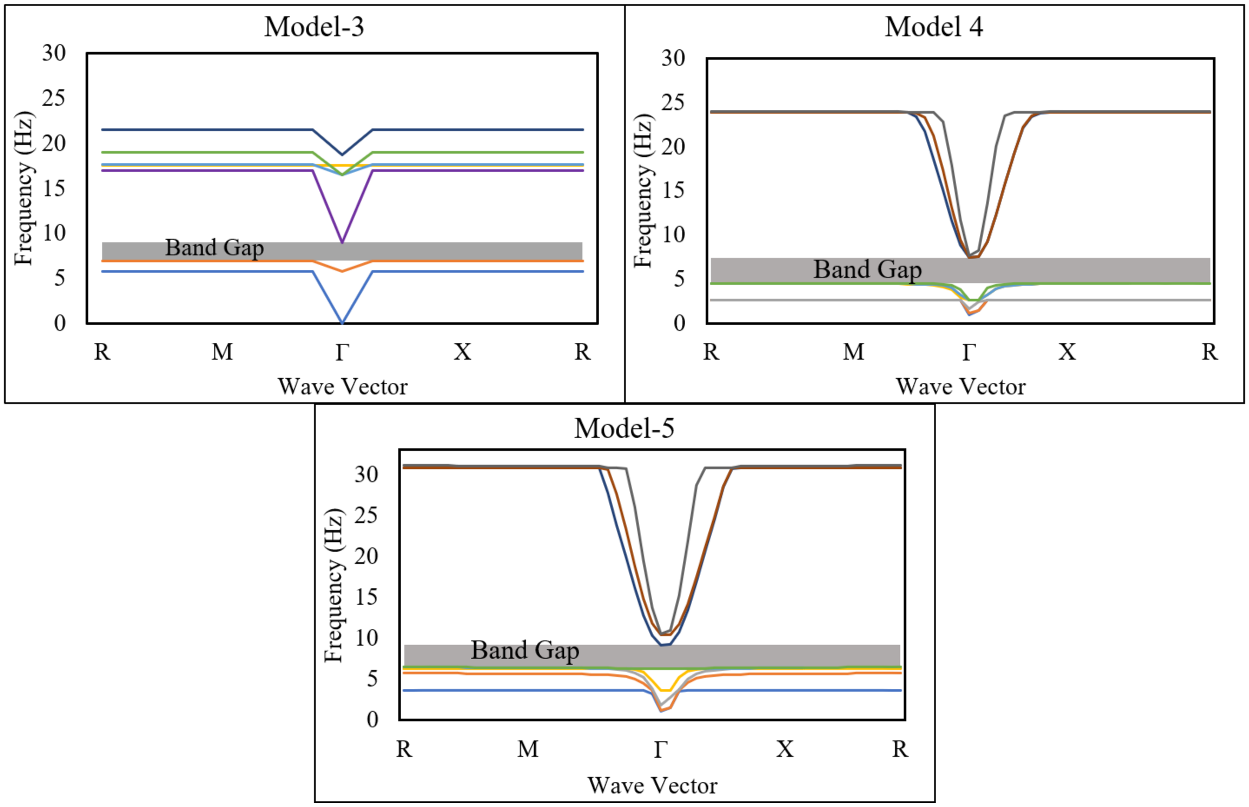

Figure 4-6: Bandgap for models 3, 4, and 5 for geometry parametric study.

4.1.2. Unit Cell Number of Layers and Properties Parametric Study

After finalizing the geometry of the unit cell, the second parametric study is the number of layers that comprise the unit cell. This study aims to find the lowest possible bandgap limit and the broadest possible bandgap. The vertical axis periodicity has been removed from the unit cell since the surface waves are the focus of this research. Therefore, the vertical periodic conditions are necessary and will save the analysis cost. Initially, individual materials were investigated by studying each proposed material block (Type-I unit cell). Thereafter, unit cells with two layers (Type II) including matrix and core, three layers (Type II) including matrix, coating, and core, and four layers (Type IV) including matrix, two coatings, and core are studied. Common construction materials used in the study include concrete, carbon fiber reinforced polymer (CFRP), steel, rubber, and soil.

Additionally, tungsten was among the used materials. Although tungsten is not a typical construction material, it is rare, costly, and very dense. It was used due to its high density for the sake of material comparisons. Table 4-5 shows the properties of the materials used in this study. Material properties are assumed to be homogenous, linearly elastic, and isotropic. The contact regions between different layers are assumed to be perfectly bonded.

Table 4-5: Material properties for the used materials in the unit cell number of layers parametric study.

Material	Young's Modulus E (Pa)	Poisson's Ratio (v)	Density ρ (kg/m^3)
Concrete	30.0×10^9	0.200	2500
Rubber	1.37×10^5	0.463	1300
Soil	20.0×10^6	0.300	1800
Steel	210×10^9	0.275	7890
CFRP	39.2×10^9	0.200	1900
Tungsten	410×10^9	0.250	17500

Additionally, damping was neglected in all the studied models, a common assumption in different studies since low damping has a negligible effect on the dispersion curves (Hussein and Frazier, 2010) and attenuation zones (Zhao et al., 2007). Figure 4-7 shows the studied unit cells where *h* is the height of the unit cell, *a* is the lattice constant, *b* is the thickness of the matrix, *c* is the thickness of the first coating layer, and *d* is the thickness of the second coating layer.

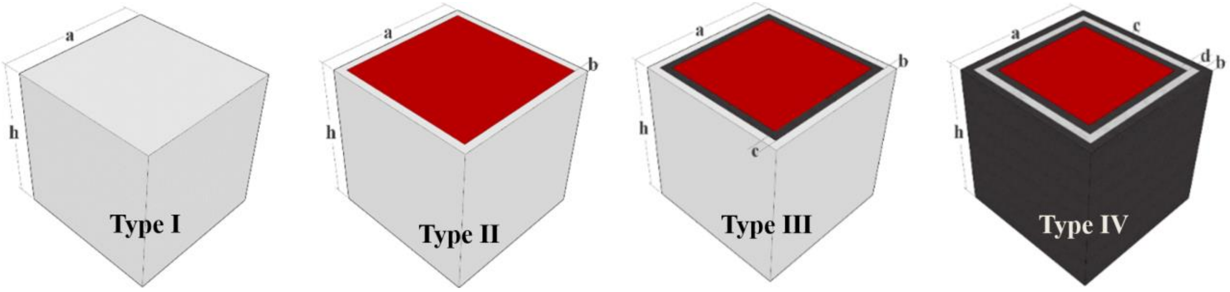

Figure 4-7: Unit cell types used for the number of layers parametric study.

Floquet-Bloch conditions (PBC) were applied to the four vertical sides of the unit cell, while the two horizontal sides remained traction-free in all cases. The lengths and thickness of the matrix were constant in all types of unit cells. Table 4-6 shows the size and thickness of each layer of the studied unit cells.

Table 4-6: Size and thickness of each layer for the studied unit cells.

Unit cell type	h (m)	a (m)	b (m)	c (m)	d (m)
Type I	2.0	h	-	-	-
Type II	2.0	h	0.9a	-	-
Type III	2.0	h	0.9a	0.8a	-
Type IV	2.0	h	0.9a	0.8a	0.7a

The FIBZ, which was used to solve the dispersion equation, is shown in Figure 4-8, where the symmetry points are swept as ($\Gamma - X - M - \Gamma$).

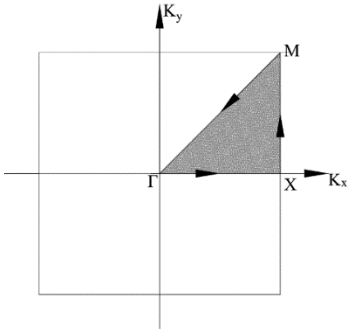

Figure 4-8: The sweeping direction along the FIBZ with symmetry points coordinates Γ: π⁄a (0,0), X:π⁄a (1,0), and M:π⁄a (1,1).

The results of the individual material (Unit cell type I) showed that none of the proposed materials had bandgap presence. This is because when solving the dispersion equation (Equation 3-10 or Equation 3-17), there will always be a real solution so that cos (*ka*) is in the range of (-1, 1). The dispersion relations for all the studied individual materials were somewhat similar, and the main difference was the frequency range. Figure 4-9 shows the dispersion relation for soil and steel where all frequencies have propagated, and no gaps were present.

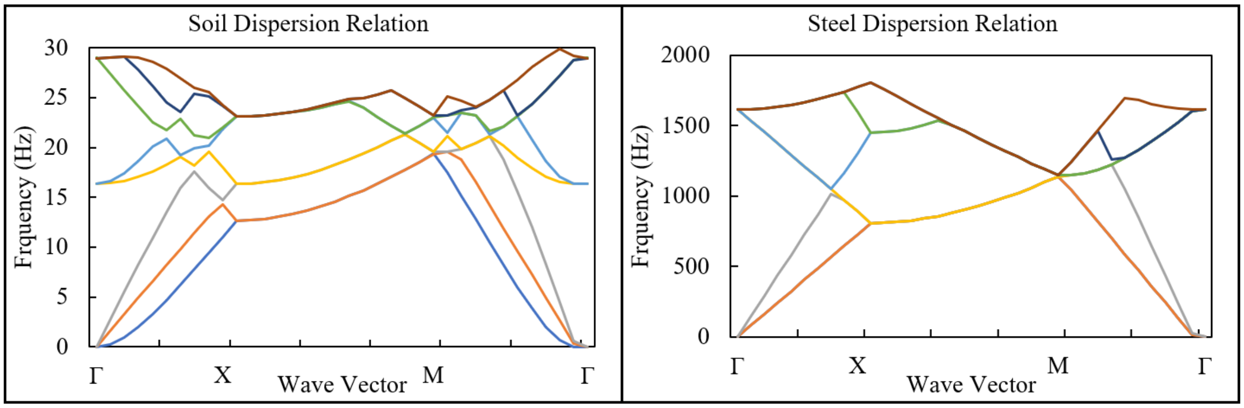

Figure 4-9: Dispersion relation for soil and steel individually.

Thereafter, a type II unit cell was investigated. The proposed unit cell included a rubber coating and varying core materials; concrete, steel tungsten, and CFRP. The limits of the bandgap were recorded for each configuration and compared for different core materials. Figure 4-10 shows the variation of the LBGL, UBGL, and BGW with each of the investigated core materials.

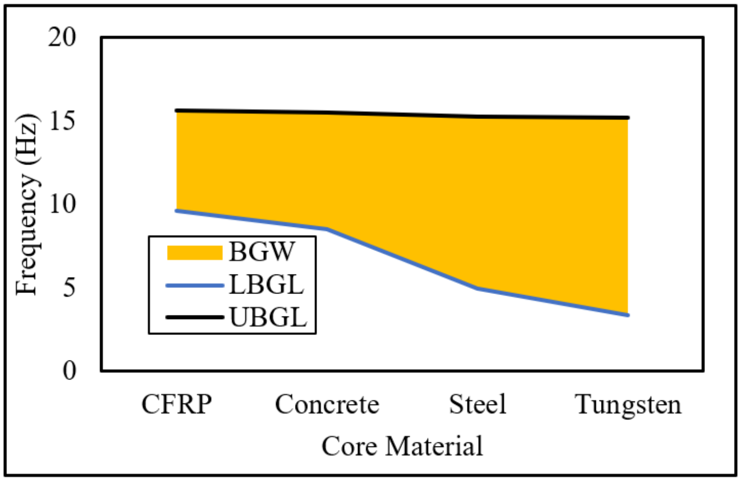

Figure 4-10: Bandgap results for type II unit cell with different core materials.

The bandgaps are 9.6-15.6 Hz, 8.5-15.5 Hz, 4.5-15.3 Hz, and 3.3-15.2 Hz for CFRP, concrete, steel, and tungsten core material, respectively. The UBGL does not show variation with core materials variation. The unit cell matrix and core size were constant in all modules. However, the modulus of elasticity and the core density differed from model to model. Therefore, studying the effects of the modulus of elasticity and core density on the bandgap is necessary. Hence, it is necessary to study the relationship between the core modulus of elasticity (MPa) and the bandgap and the relationship between the density of the core and the bandgap. To this end, a type II unit cell was created with a constant lattice constant (*a*) = 2 m to study the effects of the core modulus of elasticity on the bandgap. Table 4-7 shows the selected unit cell properties for elastic modulus investigation.

Table 4-7: Type II unit cell properties for the core modulus of elasticity study.

Layer	Modulus of Elasticity, E (Pa)	Poisson's Ratio	Density, ρ (kg/m^3)	Size (m)
Matrix	1.37×10^5	0.463	1300	2.0
Core	Variable	0.275	7890	0.9a

Figure 4-11 shows the bandgap width versus the core modulus of elasticity. It is observed that the modulus of elasticity of the core has no effect on the bandgap as both UBGL and LBGL were constant regardless of the core modulus of elasticity value.

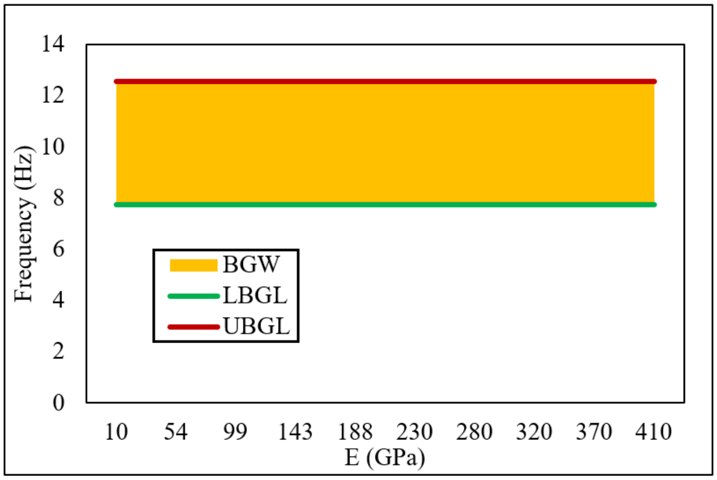

Figure 4-11: Relationship between unit cell (Type II) core modulus of elasticity and the bandgap.

Furthermore, a type II unit cell was created with a constant lattice constant (a) = 2 m to study the effects of the core density on the bandgap, Table 4-8 shows the selected unit cell properties for core density study.

Table 4-8: Type II unit cell properties for the core density study.

Layer	Modulus of Elasticity, E (Pa)	Poisson's Ration	Density, ρ (kg/m^3)	Size (m)
Matrix	1.37×10^5	0.463	1300	2.0
Core	210×10^9	0.275	Variable	0.9a

Figure 4-12 shows the bandgap width against the core density. Four main materials can be identified that have wide density variation such as but not limited to rubber (E=14 $\times 10^{-5}$ GPa and $\rho = 1300\,kg/m^3$) carbon fiber reinforced polymer (E=392 GPa and $\rho = 1900\,kg/m^3$), concrete (E=30 GPa and $\rho = 2500\,kg/m^3$), steel (E=210 GPa and $\rho = 7890\,kg/m^3$), and tungsten (E=410 GPa and $\rho = 17500\,kg/m^3$). It is observed that the bandgap width is proportional to the core density. The higher the core density, the wider the bandgap.

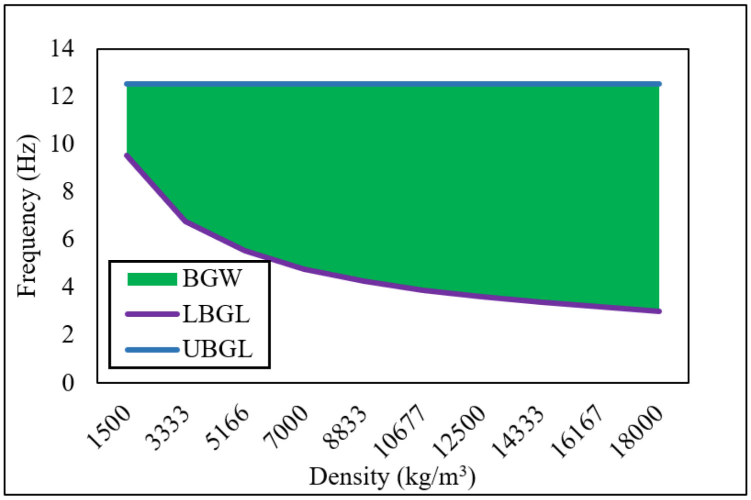

Figure 4-12: Relationship between unit cell (Type II) core density and the bandgap.

Results of type II unit cell show that rubber matrix and steel core seem to be the best candidate for development since both rubber and steel are common materials used in construction. Furthermore, the resultant bandgap of 4.5-13.5 Hz, when rubber and steel are used, the widest observed bandgap among the investigated materials excluding tungsten core because it is not a common construction material. Moreover, unit cells with tungsten core had a wider bandgap (3.3-15.2 Hz). However, tungsten is used in this study for comparison as it is not a common construction material and is expensive. Therefore, a type II unit cell with a rubber matrix and a steel core was selected as a final candidate for two layers unit cells. The dispersion relation of the final type II candidate is shown in Figure 4-13. There are five bandgap boundaries where each has a starting frequency and cut-off frequency, and some of the bandgaps share the same boundary. There are five bandgap bounds points A, B, C, D, and E.

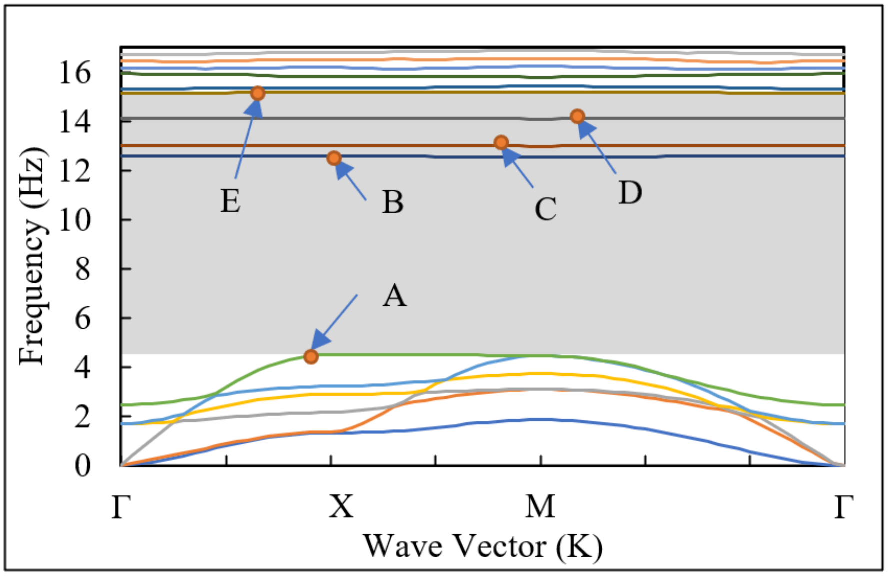

Figure 4-13: Dispersion relation for type II unit cell (3D-2C) made of rubber matrix and steel core.

Figure 4-14 shows the global vibrational modes of type II unit cell at five bandgaps bounds points. The direction and length of the arrows in the figures represent the direction and the magnitude of the relative displacement.

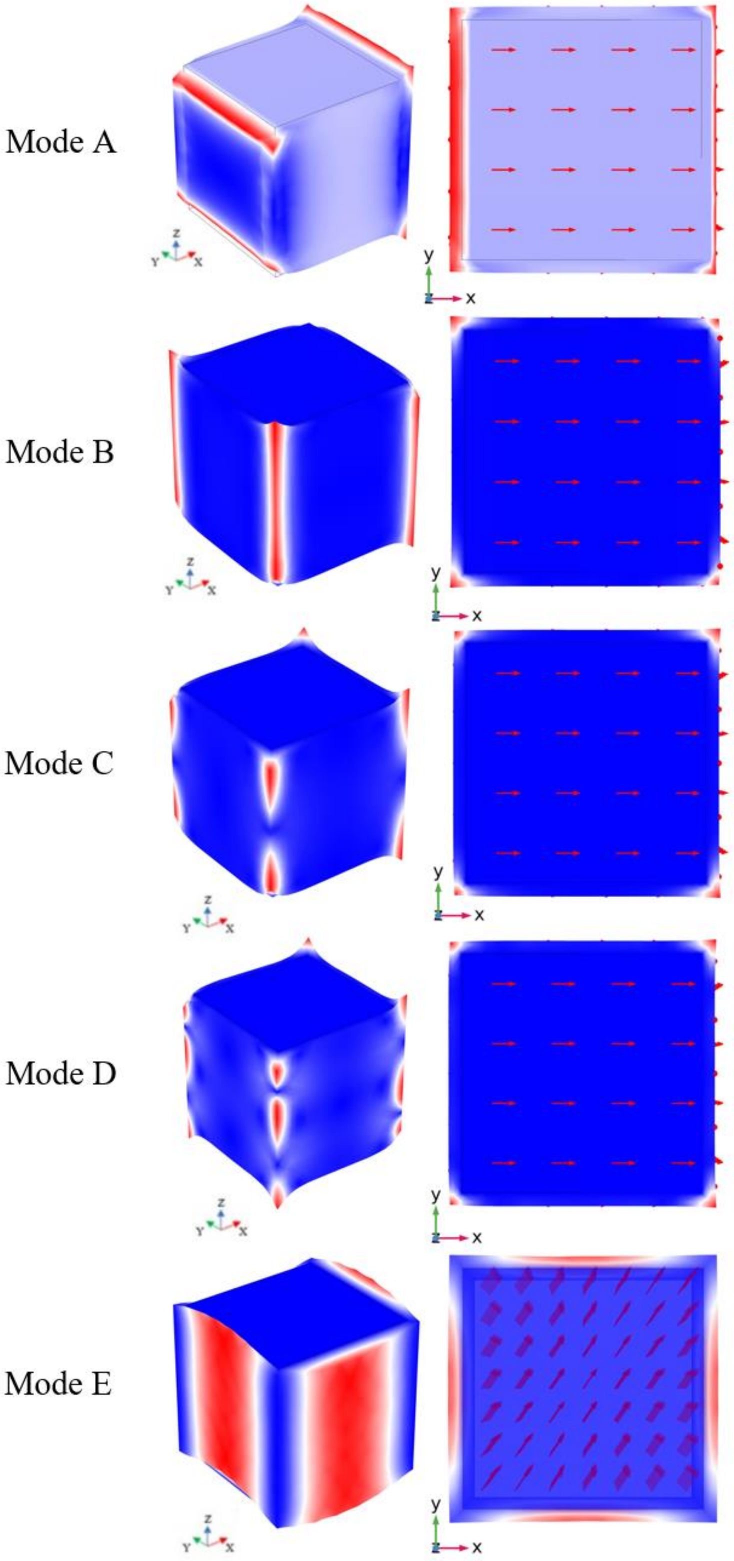

Figure 4-14: Global vibrational modes of type II unit cell.

The unit cell had four bandgaps; the first one is 4.5-12.5 Hz, 2nd bandgap is 12.7-13.0 Hz, 3rd bandgap is 13.1-14.1 Hz, and 4th bandgap is 14.2-15.3 Hz. It is worth mentioning that there are individual frequencies that propagate through the unit cell, which leads to four different bandgaps. Examining the vibrational modes in Figure 4-14, it is observed that for the UBGL, the displacement is maximum at the edges of the unit cell and minimal elsewhere, while at the LBGL, the displacement is maximum at the corners and extends along the length of the unit cell. Those modes are examined to prove that the destructive interferences (outer layer, rubber) are responsible for wave attenuation. It should be noted that the contours represent relative displacement (modal values), not stress.

Type III unit cells with matrix, coating, and core were investigated afterwards. The size of the unit cell was constant a = 2 m as in type II unit cell, and the coating and the core were constant and were made of rubber and steel, respectively. With the same approach as followed in type II unit cell, type III unit cell were investigated. The study included various matrix materials; Table 4-9 shows the investigated unit cells, and Table 4-5 shows the used material properties. FIBZ and PBC were also constant, as previously used in type II unit cell.

Table 4-9: Three-layer unit cell studied configurations (Type III).

Model No.	Matrix	Coating	Core
1	Concrete	Rubber	Steel
2	Tungsten	Rubber	Steel
3	Rubber	Tungsten	Steel
4	Steel	Rubber	Steel
5	CFRP	Rubber	Steel

Type III unit cell with different configurations showed that the LBGL was constant (5.5 Hz) in all the studied models apart from model-3, which showed 4.4 Hz. Moreover, the UBGL showed significant variation in model-1 UBGL is 17.1 Hz, model.8.6 Hz, model.3 15.2 Hz, model-4 is 11.2 Hz, and model-5 is 19 Hz, and bandgap widths of 11.6 Hz, 3.0 Hz, 10.8 Hz, 5.7 Hz, and 13.5 Hz for models 1 to 5 respectively. Table 4-10 shows the results of the studied type III unit cells.

Table 4-10: Three-layer unit cell configurations (Type III) bandgaps.

Model No.	LBGL (Hz)	UBGL (Hz)	BGW (Hz)
1	5.5	17.1	11.6
2	5.6	8.60	3.0.
3	4.4	15.2	10.8
4	5.5	11.2	5.70
5	5.5	19.0	13.5

As a result of having a three-layer unit cell, the attenuation zones have improved in some cases. For instance, for a unit cell with CFRP matrix, rubber coating, and steel core, the bandgap width is 13.5 Hz, which shows 3.1 Hz additional to UBGL compared to type II unit cell, rubber, and steel, unit cell; on the other hand, the LBGL increased from 4.5 Hz to 5.5 Hz. However, the bandgap has been reduced in other cases of the three-layer unit cell.

It is noticeable that for a type III unit cell, the coating and the matrix materials were constant and made of rubber and steel, respectively, apart from model-3, which had tungsten coating. Therefore, model-3 will be excluded from the comparison. Since the LBGL remained constant and only the UBGL limit changed along with the matrix material, a relationship exists between the matrix material and the UBGL. Hence, two comparisons were analyzed for type III unit cell: matrix modulus of elasticity versus UBGL, and the density versus the UBGL. Where the materials used are carbon fiber reinforced polymer (E=392 GPa and $\rho = 1900\ kg/m^3$), concrete (E=30 GPa and $\rho = 2500\ kg/m^3$), steel (E=210 GPa and $\rho = 7890\ kg/m^3$), and tungsten (E=410 GPa and $\rho = 17500\ kg/m^3$). Figure 4-15 shows the relationship between the unit cell UBGL and the unit cell matrix modulus of elasticity.

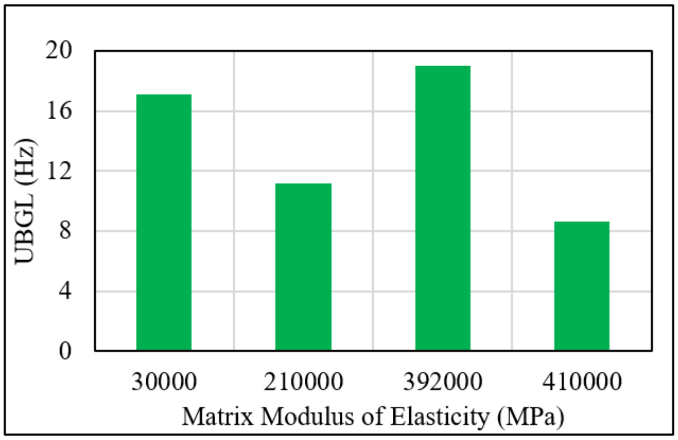

Figure 4-15: Relationship between matrix modulus of elasticity and the upper bandgap limit for type III unit cell.

Figure 4-15 indicates no correlation between the matrix modulus of elasticity and the upper bandgap limit. Figure 4-16 shows the relationship between the matrix density and the UBGL.

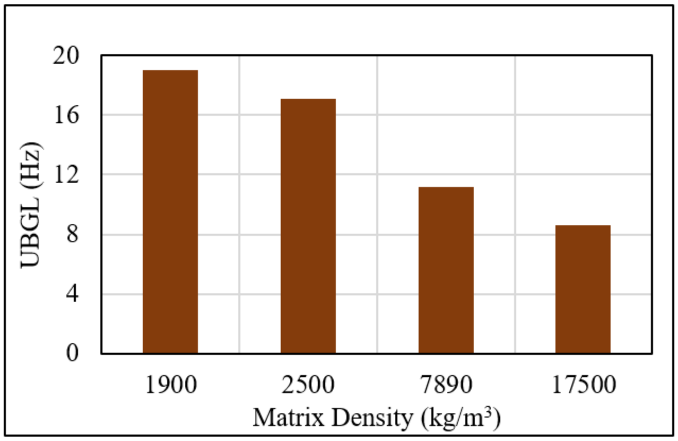

Figure 4-16: Relationship between matrix density and the upper bandgap limit for type III unit cell.

Figure 4-16 shows that the upper bandgap limit (UBGL) is inversely proportional to the matrix density. Therefore, using a low-density material as a matrix is highly recommended to achieve the highest possible upper bandgap limit. Figure 4-17 shows the dispersion relation of a three-layer unit cell made of CFRP matrix, rubber coating, and steel core (Type II), which shows the widest bandgap, the grey-shaded area in Figure 3-22. Additionally, Figure 4-17 shows the vibrational modes of Type II at the upper (A1) and lower limits (B1) of the bandgap, where the maximum displacement at the UBGL occurs at the corners of the coating materials and minimal elsewhere. In contrast, the maximum displacement occurs at the corners and extends along the edges at the LBGL.

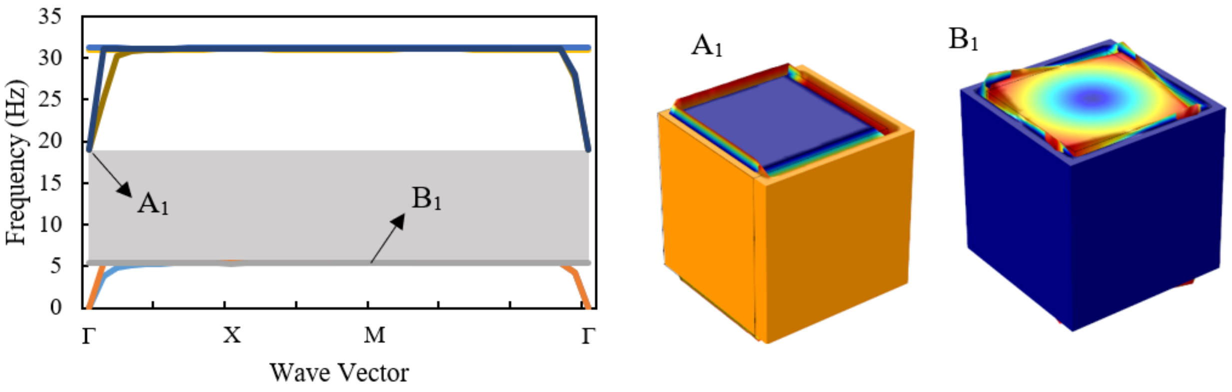

Figure 4-17: Unit cell of three layers dispersion relation and the global vibrational modes for type III unit cell.

When comparing type II and type III unit cells, type III unit cells showed higher UBGL (17.1 Hz and 19.0 Hz) than type II (15.3 Hz). However, comparing the LBGL type II unit cell showed less LBGL (4.5 Hz) than type III unit cell (5.5 Hz). It is very well known that the lower the frequency of a wave, the longer the wavelength will be. Therefore, blocking frequencies in the ultra-low range is more difficult than in the high range, and such frequencies are the most disastrous and more difficult to protect from. Hence, a type II unit cell with a bandgap from 4.5-15.3 Hz is the potential candidate for additional development.

Similarly, type IV unit cells were investigated with different material combinations. Table 4-11 shows the studied four-layer unit cells. Size, PBC, and FIBZ were all constants across all studied type IV models.

Table 4-11: Four-layer unit cell configuration (Type IV).

Model No.	Matrix	Coating-1	Coating-2	Core
1	Concrete	Tungsten	Rubber	Steel
2	Concrete	CFRP	Rubber	Steel
3	CFRP	Tungsten	Rubber	Steel
4	Concrete	Steel	Rubber	Steel

The attenuation zones for the investigated four-layer unit cell (type IV) are narrower than those of three- or two-layer metamaterial due to the significantly reduced core material size. The widest bandgap achieved using a four-layer unit cell is 7.8 Hz, grey shaded area in Figure 4-18, for the case of concrete matrix, CFRP as the first coating layer, rubber as a second coating layer, and steel as a core. Table 4-12 shows the bandgaps of the investigated four-layers unit cell (Type IV).

Table 4-12: Four-layer unit cells dispersion relation results (Type IV).

Model No.	LBGL (Hz)	UBGL (Hz)	Bandgap width (Hz)
1	5.8	8.4	2.6
2	5.8	13.6	7.8
3	5.8	8.5	2.7
4	5.8	10.2	4.4

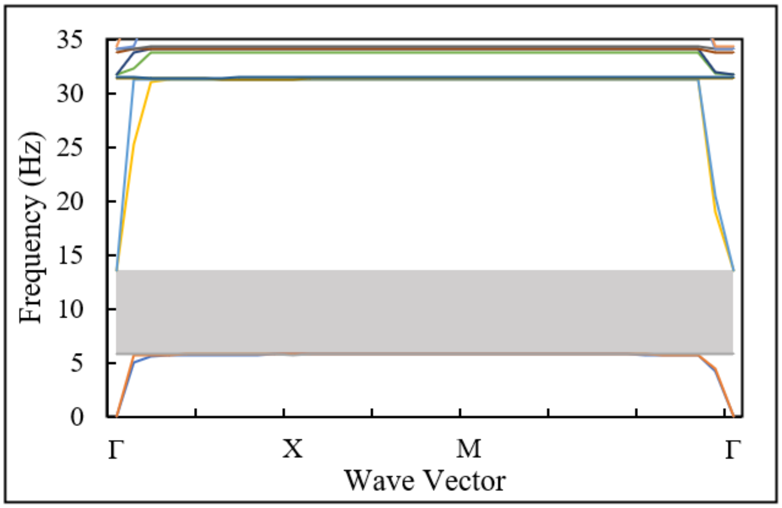

Figure 4-18: Dispersion relation for a unit cell of four layers (Type IV).

Type IV unit cells showed that the LBGL remained constant, similar to the UBGL of type III unit cell, and only the UBGL varies, which is, as observed previously, due to the density of the unit cell matrix. Finally, when comparing unit cells type II and type IV, type II is the best possible choice for development because it resulted in the broadest and lowest possible bandgap.

While investigating metamaterial Types II, III, and IV, it was observed that the core density is the most crucial factor in the bandgap width, more specifically, the LBGL. To this end, a parametric study using a type II unit cell made of 2.0 m rubber and a variable steel core size from 0.1 m-1.9 m was performed to study the effects of the unit cell core size. Similarly, type III unit cell with a concrete matrix of 2.0 m, rubber coating of 1.8 m, and a variable steel core size from 0.1 m-1.7 m were analyzed. Type IV was excluded from the parametric study due to exhibiting low bandgap width. Figure 4-19 shows the variation of the LBGL and UBGL of the bandgap with the core size for the type II unit cell. The grey area represents the bandgap width, and the two solid lines show the lower and upper bandgaps. The bandgap width is proportional to the core size. Furthermore, having a relatively low core size (less than 40% of the matrix size) results in no to extremely narrow bandgap. Moreover, the LBGL increases due to the reduction in the matrix size, which confirms the previous observation that the lower the matrix density, the higher the bandgap will be.

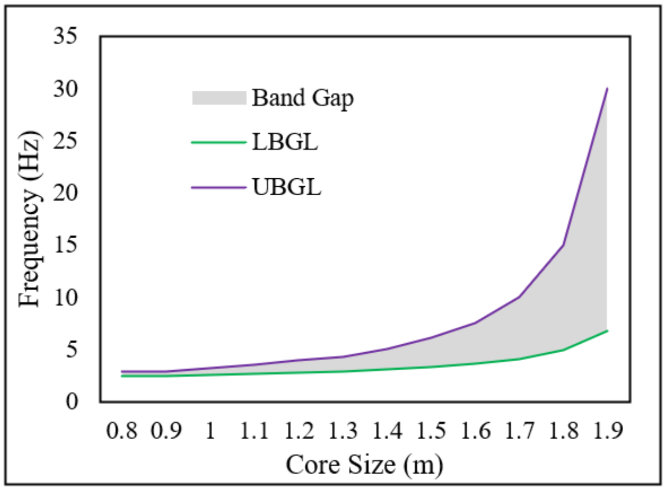

Figure 4-19: Bandgap variation with the core size for two-layer unit cell (Type II).

Similarly, Figure 4-20 shows the variation of the bandgap width with core size for type III unit cell made of concrete matrix, rubber coating, and steel core. At a smaller core material size, two narrow bandgaps can be observed, shown in light grey and orange colors, and as the core size increases, the second bandgap (orange colored) starts diminishing to approximately zero. On the other hand, the first bandgap is proportional to the core material size, like a type II unit cell, and the LBGL decreases with the reduction of the coating material size.

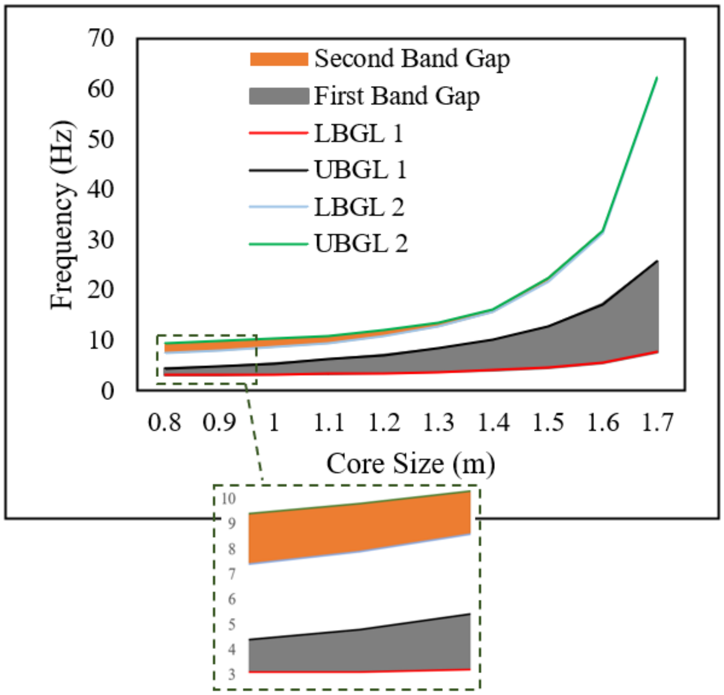

Figure 4-20: Bandgap variation with the core size for a three-layer unit cell (Type III).

After the careful study discussed above, the two-layer rubber coating and steel core unit cell (Type II) were chosen for further investigation because they represent the best combination due to the availability of material, ease of assembly, wide attenuation zone, and the lowest LBGL frequency. Figure 4-21 shows the selected unit cell and its related dispersion relation with four different bandgaps first is 4.5-12.5 Hz, second is 12.7-13.0 Hz, third is 13.1-14.1 Hz, and fourth is 14.2-15.3 Hz.

The unit cell size is 2 m with a matrix thickness of 0.1 m. Rubber was selected as matrix material with 0.14 MPa modulus of elasticity, 0.463 Poisson's ratio, and 1300 kg/m^3 density. Moreover, steel was selected as the core material with 210 GPa modulus of elasticity, 0.275 Poisson's ratio, and 7890 kg/m^3 density. PBC was applied at the four vertical sides of the unit cell, and the two top and bottom surfaces were traction-free.

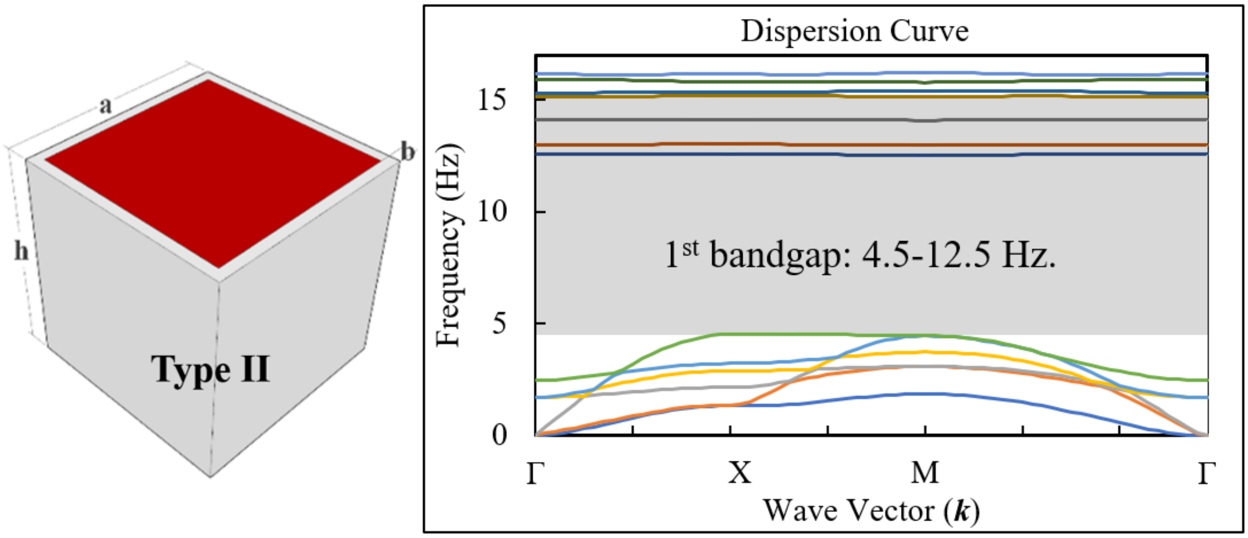

- 2nd bandgap: 12.7-13.0 Hz.
- 3rd bandgap: 13.1-14.1 Hz.
- 4th bandgap: 14.2-15.3 Hz.

Figure 4-21: Final selected unit cell (Type II) and its dispersion relation.

4.2. Unit Cell Simplified Spring-Mass Model

In the previous section, the characteristics of the unit cell were investigated based on FEA. In this section, the global vibrational modes of the bandgap limit frequencies are simplified into equivalent spring-mass model to theoretically determine the bandgap width of the unit cell.

Examining the vibrational mode A in Figure 4-14, the global displacement of the steel is along the positive X-direction, while the rubber displaces slightly at the edges along the Y-direction. Examining the vibrational mode E in Figure 4-14, the rubber displaces larger than the steel core in all directions. Moreover, in all the vibrational modes, the rubber displaces followed by steel because the rubber has a small width compared to the steel core. Therefore, the rubber matrix can be considered a spring, and the steel core is the mass. Such displacement modes can be written in simplified equivalent spring-mass mode, as shown in Figure 4-22, where m is the equivalent mass and k is the equivalent spring stiffness. A similar approach has been studied for other types of unit cells in the literature (Chen et al., 2022).

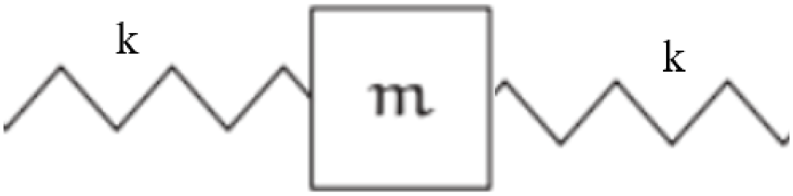

Figure 4-22: Type II unit cell equivalent spring-mass model.

Since the unit cell is symmetrical about the X-axis, it would be sufficient to consider only half of the unit cell. The mass of the rubber can be divided into two masses, m_1, and m_2, where m_1 is represented as a spring connecting the other half of the rubber to the steel since the steel displacement is relative to the rubber, and most of the rubber displacement occurs in this part by tension/compression deformation. On the other hand, m_2 displacement is negligible, and the stiffness provided by the rubber part is negligible compared to m_1. Figure 4-23 shows the unit cell discretization.

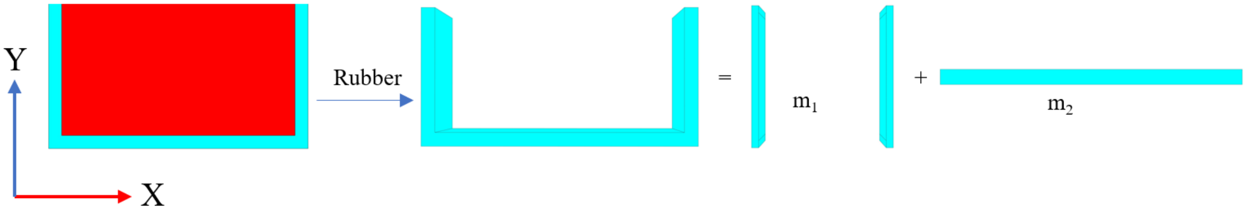

Figure 4-23: Unit cell discretization for defining the spring-mass model.

Thereafter, m_1 is divided into two parts, m_{11}, and m_{12}, by the mass ratio α. Where $\alpha = \frac{m_R}{m_S}$. The mass ratio is represented by a fixed distance between the steel core and the end of the rubber matrix. This distance is shown in Figure 4-24.

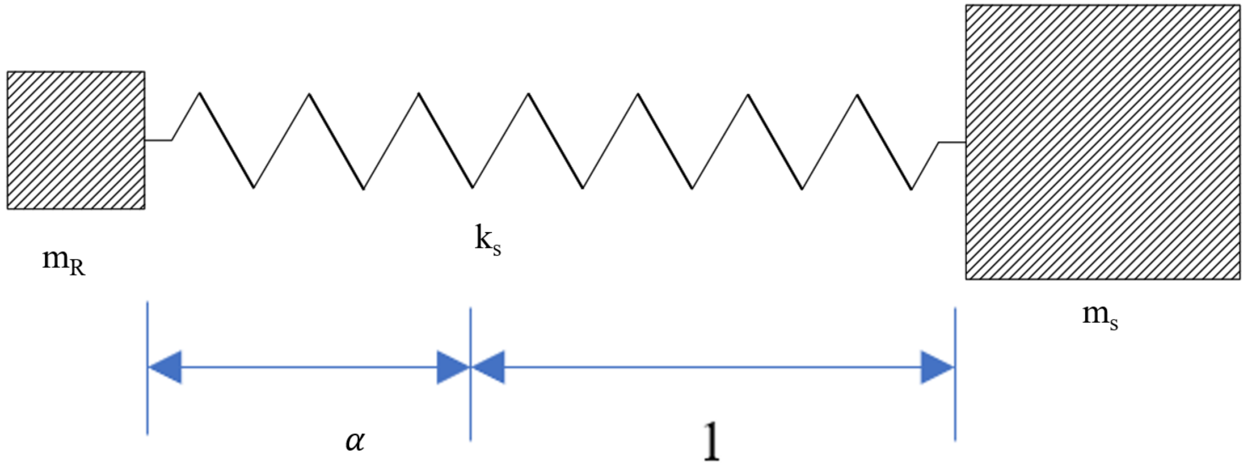

Figure 4-24: Spring-mass-spring equivalent model.

As explained above, the final masses would be (Equations 4-1 and 4-2).

$$m_s = m_{steel} + m_1 \times \frac{\alpha}{\alpha + 1} \quad \text{Eq. 4-1}$$

$$m_R = m_2 + m_1 \times \frac{1}{\alpha + 1} \quad \text{Eq. 4-2}$$

Solving Equations 4-1 and 4-2, the ratio α can be found (Equation 4-3).

$$\alpha = \frac{m_2 + m_1}{m_{steel} + m_1} \quad \text{Eq. 4-3}$$

Using Figure 4-23, the rubber masses (m_1 and m_2) can be calculated as follows (Equation 4-4):

$$m_1 = \rho_{Rubber} \times 2 \times (0.1 \times 0.9 \times 2) = 468kg$$

$$m_2 = \rho_{Rubber} \times (0.1 \times 2 \times 4) = 1040kg \quad \text{Eq. 4-4}$$

The mass of the steel m_{steel} can be calculated (Equation 4-5):

$$m_{Steel} = \rho_{steel} \times (0.9 \times 1.8 \times 2) = 25563.6kg \qquad \text{Eq. 4-5}$$

Finally, solving Equations 4-1, 4-2, and 4-3 yields $\alpha = 0.038$, m_R = 1489.29 kg, and m_S = 25580.7 kg.

Thereafter, the rubber stiffness can be calculated using Equation 4-6:

$$k = \frac{(\lambda+2\mu) \times length}{depth} = \frac{(\frac{1.37\times10^5\times0.463}{1.463\times0.074}+\frac{1.37\times10^5}{1.463})\times2\times0.9}{0.1} = 1.22 \times 10^7 \text{ N/m} \qquad \text{Eq. 4-6}$$

Finally, the lowest passing frequency can be calculated using Equation 4-7:

$$f_l = \frac{1}{2\pi} \times \sqrt{\frac{k}{m_S}} \qquad \text{Eq. 4-7}$$

Solving Equation 4-7 gives the lowest passing frequency (f_l) of 3.5 Hz, while the FEA analysis showed that the lowest bandgap limit is approximately 4.5 Hz, showing a good match between the results. On the other hand, the highest passing frequency (f_h) can be calculated using Equation 4-8, which shows that the highest passing frequency is 14.5 Hz.

$$f_h = \frac{1}{2\pi} \times \sqrt{\frac{k}{m_R}} \qquad \text{Eq. 4-8}$$

The FEA showed that the highest passing frequency is 15.3 Hz, which closely matches the FEA result.

Therefore, the mass-spring simplified model can be used to predict the bandgap bounds of a unit cell. Moreover, Equations 4-7 and 4-8 agree well with the previously concluded hypothesis that the lower bandgap limit depends on the core mass, and the upper bandgap limit is inversely proportional to the matrix mass.

4.3. Verification of Bandgap Existence

Once the dynamic response methodology is verified, the first step would be verifying the existence of the bandgap and verifying the selected unit cell bandgap. To this end, a similar model to Figure 4-25 has been used with 16-unit cells arranged without spacing between them. Low-amplitude harmonic displacement was applied at the interface between the soil and the PML to the left side of the model to simulate elastic bulk wave propagation. Figure 4-25 shows the unit cell for the reduced frequency domain analysis.

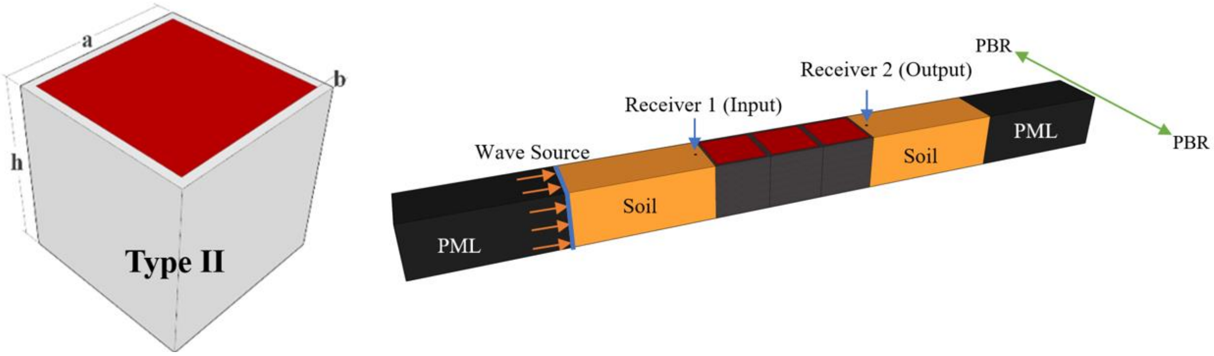

Figure 4-25: Type II unit cell and the typical reduced model for the frequency domain analysis.

The waves start at the interface and propagate through the homogeneous soil until it reaches the unit cells, and the PML absorbs all the incoming waves, preventing unnecessary wave reflection back to the model. The size of the PML and homogenous soil was selected as twice the size of the unit cells altogether, with an array of 16-unit cells arranged between the two homogenous soils. Material properties are shown in Table 4-13.

Table 4-13: Material properties of the dynamic response model.

Material	Young's Modulus E (Pa)	Poisson's Ratio (v)	Density ρ (kg/m^3)
Soil	$20.0\ \times 10^{6}$	0.300	1800
Rubber	$1.37\ \times 10^{5}$	0.463	1300
Steel	$210\ \times 10^{9}$	0.275	7890

Figure 4-26 shows the bandgap of the unit cell as observed in the dispersion relation equation and the transmission as observed in the dynamic frequency domain analysis. It can be observed that there is an excellent match between both results.

When calculating the transmission between before and after the unit cell, the result will be positive or negative. When the transmission is positive, the input displacement is lower than or equals the output displacement, which means that the unit cell could not block the wave at that incident frequency, and in some cases, amplified it. On the other hand, when the transmission is negative,the input displacement is higher than the output displacement, which means that the unit cells managed to absorb the incoming wave incident preventing it from propagating to the other end where the structure is located and therefore protected the structure from the incoming wave. Figure 4-26 shows that the transmission when the frequencies range from 4.5 to 15.3 Hz is negative (Grey shaded area in Figure 4-26), concluding that the unit cells arrangement blocked all the incoming waves that fell in that range.

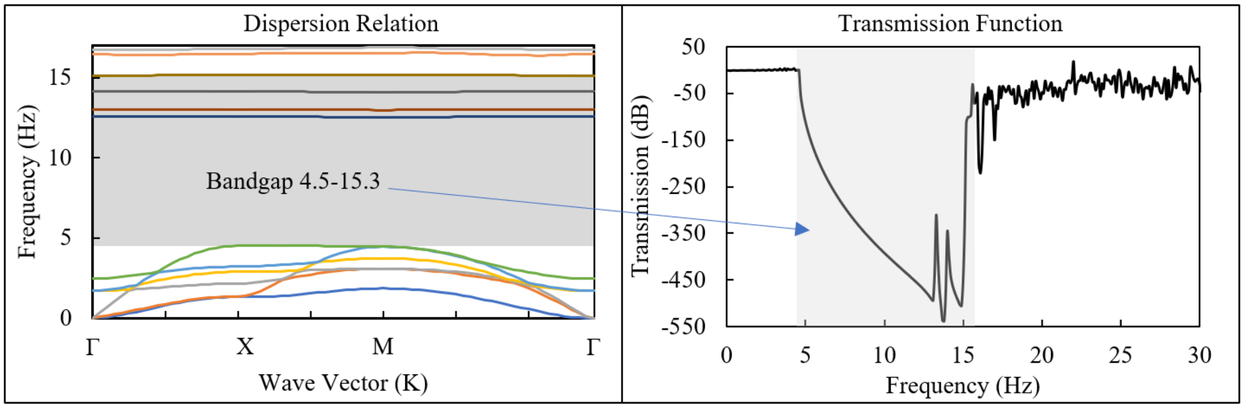

Figure 4-26: Dispersion relation and Transmission of type II unit cell.

4.4. Variation of Configuration of the Array of Unit Cells to Manipulate the Bandgap

In this parametric study, the reduced frequency domain model will be used (Section 3.3.). The reduced method allows a significant reduction in computational time. Figure 4-27 shows the proposed configurations where Model-A represents typical unit cells configurations where the unit cells are arranged back-to-back. This model simulates a periodic unit cell in two directions. Models-B and C have uniformly spaced configurations where the unit cells are arranged uniformly. Models-D and E are a single-graded configuration with the starting unit cells arranged back-to-back, and the remaining are uniformly spaced. Finally, Model-F represents a double-graded configuration where the starting cells are back-to-back, then uniform spacing, then increased uniform spacing, then decreased spacing, and finally, a back-to-back arranged cell. Such configuration is adopted from the linear chirped configuration (Shahoei et al., 2012) used in microwaves photonics (Figure 3-22).

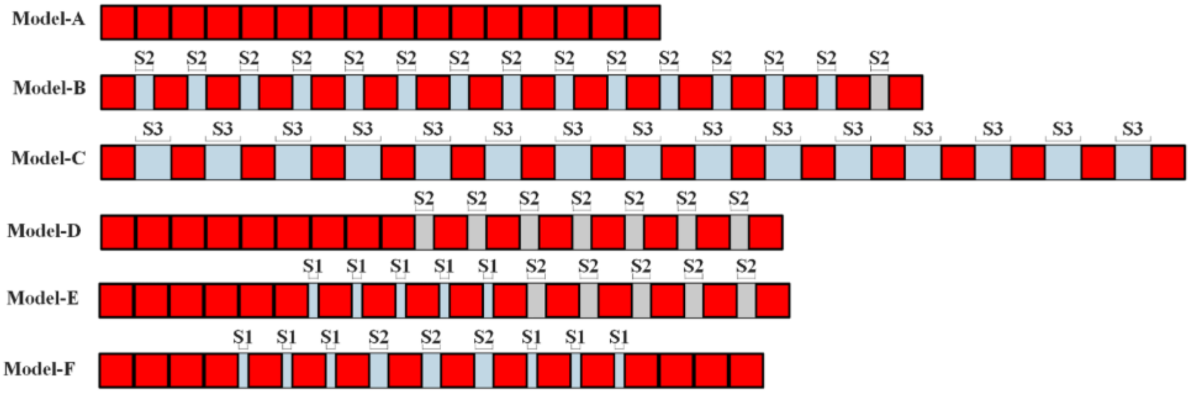

Figure 4-27: Unit cells proposed configurations.

Type II unit cell is used in this study since it was the best unit cell with the broadest possible bandgap (Section 4.1.). The material properties used in the reduced frequency response mode are shown in Table. 4-14.

Table 4-14: Material properties for the frequency response reduced model.

Material	Modulus of Elasticity, (E) (MPa)	Density, (ρ) (kg/m^3)
Rubber	0.14	1300
Steel	210 000	7890
Soil	30	1800

The spacings used in Models A to F are S_1 = 0.25a, S_2 = 0.5a, and S_3 = 2a, where *a* is the lattice constant. 16-unit cells are used in all models. The spacings between the unit cells are filled with homogenous soil. Two receiver points will be used to capture the input and output displacements which will be used to calculate the transmission among the unit cells. The transmission can be calculated using wave energy, displacements, velocity, acceleration, or velocity. However, since the incoming waves are generated by applying a low-amplitude harmonic displacement at the interface between the homogenous soil and the PML to the left side of the models, displacement will be used to calculate the transmission to maintain consistency in all calculations. Model-A will be used as a base model to compare the results of the remaining configurations. PBC is applied at the vertical sides of the model, and the top and bottom sides remain traction-free surfaces. Notably, the free surfaces are used to imitate Lamb waves in plates (Miniaci et al. 2016; Zeng et al. 2019; Zhang et al. 2021). However, quasi-Lamb waves may be generated as well. Moreover, the free surfaces are breached when the unit cells are stacked and embedded in soil. However, their effects on the bandgap are proven to be negligible (Zeng et al. 2019).

Figure 4-28 shows the dispersion relation of Models A and B. It can be observed that using uniform spacing increased the upper bandgap limit (Marked by a green circle), and the unit cell observed bandgap is shown in the grey-shaded area. However, the uniform spacing allowed some frequencies (Marked by a red circle) within the bandgap to propagate. Therefore, the uniformly spaced configuration cannot be a good candidate since it decreases the lower bandgap limit.

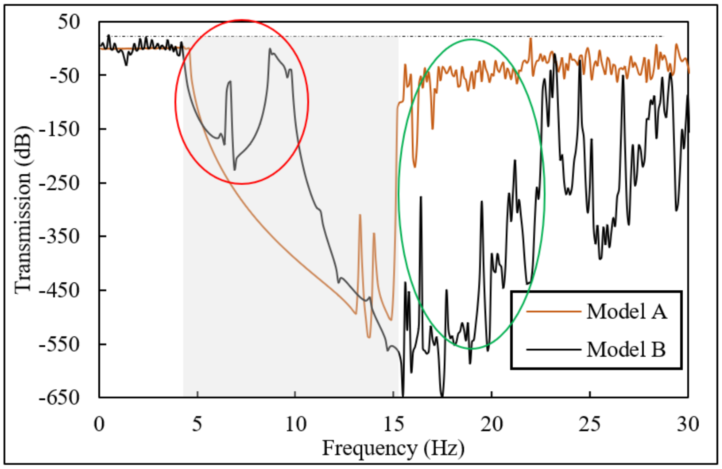

Figure 4-28: Comparison of Transmission between model-A and model-B.

Similarly, model-C (Uniformly spaced configuration with higher spacings than model-B) yielded the same results as model-B except the upper bandgap limit increased (Marked in green circle) more than that of model-B and allowed waves that were within the bandgap to propagate (Marked in red circle) through the unit cells, as shown in Figure 4-29 (the grey shaded area represents the unit cell observed bandgap).

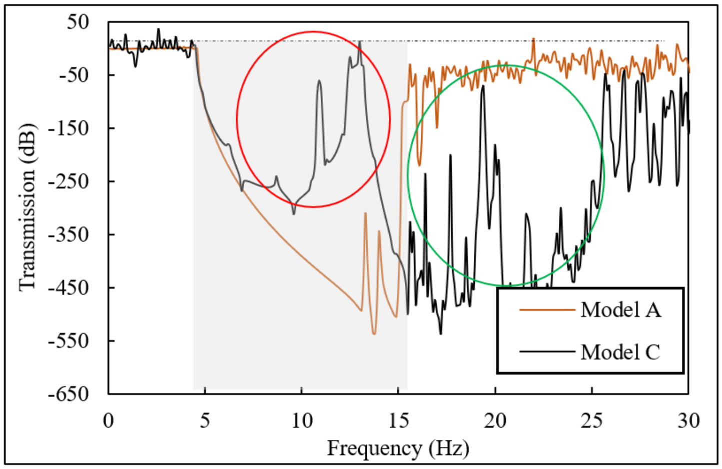

Figure 4-29: Comparison of Transmission between model-A and model-C.

Furthermore, model-D, a single-graded configuration, was analyzed, and the result showed an increase in the upper bandgap limit without adverse effects on the lower limit. The upper bandgap limit increased from 15.3 to 17 Hz, and an additional bandgap occurred between 21-26 Hz, as shown in the marked green circle in Figure 4-30, where the bandgap is shown in the grey-shaded area.

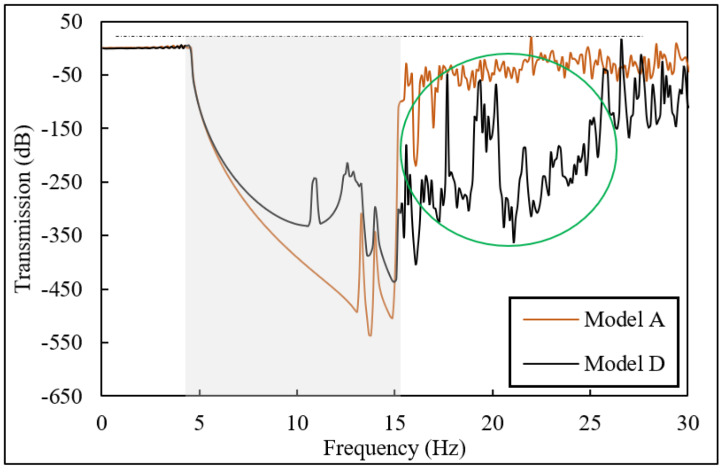

Figure 4-30: Comparison of Transmission between model-A and model-D.

Moreover, model-E is a single-graded configuration with three-unit cell arrangements, starting with back-to-back cells, then spaced at 0.25a, and ending with cells spaced at 0.5a. The results showed a consistent upper bandgap limit. However, instead of increasing the upper bandgap limit, it created a different bandgap, between 18-26 Hz, as marked in the green circle in Figure 4-31. Finally, the double-graded configuration results, shown in Figure 4-32, showed that double-graded configurations could increase the upper bandgap significantly as the bandgap increased from 15.3 Hz to nearly 30 Hz. The increase was consistent along frequencies higher than the UBGL, and all frequencies in the range of the unit cell bandgap were blocked. Therefore, the double-graded mode with type II unit cell has been selected as a final configuration model that will be evaluated using the full frequency domain model. Additionally, the double-graded configuration is used to evaluate its performance in the frequency and in the time domains.

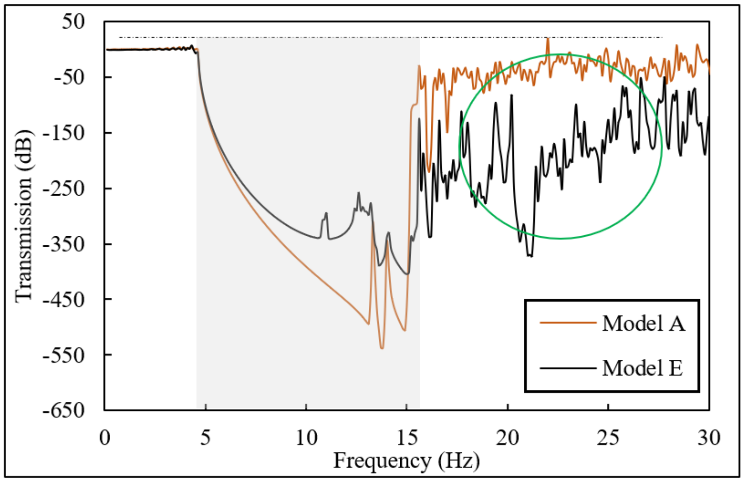

Figure 4-31: Comparison of Transmission between model-A and model-E.

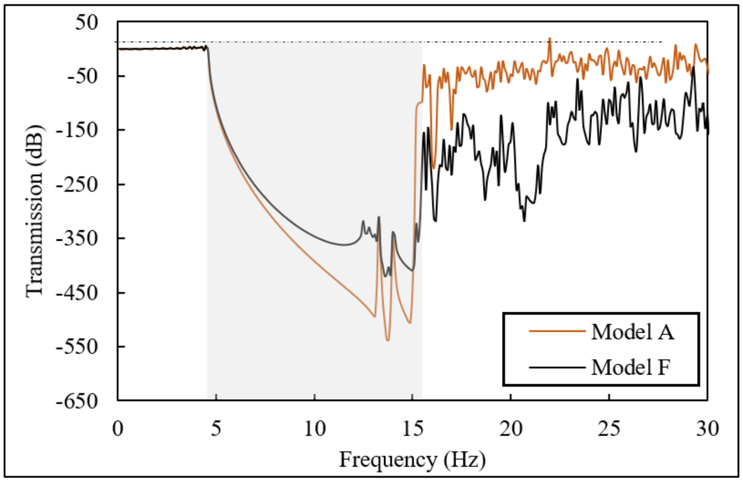

Figure 4-32: Comparison of Transmission between model-A and model-F.

4.5. Evaluation of the Performance of the Selected Configuration in the Frequency Domain Using Full Model

After selecting the final unit cells configuration, the next step is to embed the unit cells in a large soil medium since the unit cells will eventually be buried in the soil. To this end, the methodology presented in section 3.4. will be implemented here.

Figure 4-33 shows the full-frequency domain model with the two receiver nodes. Two types of waves are applied in this evaluation: Surface waves, which are generated by applying a low-amplitude harmonic displacement at the upper edge between the homogenous soil and the PML to the left side of the model in the vertical direction, and bulk waves, which is generated by applying a low-amplitude harmonic displacement along the interface between the homogenous soil and the PML to the left side of the model in the vertical direction.

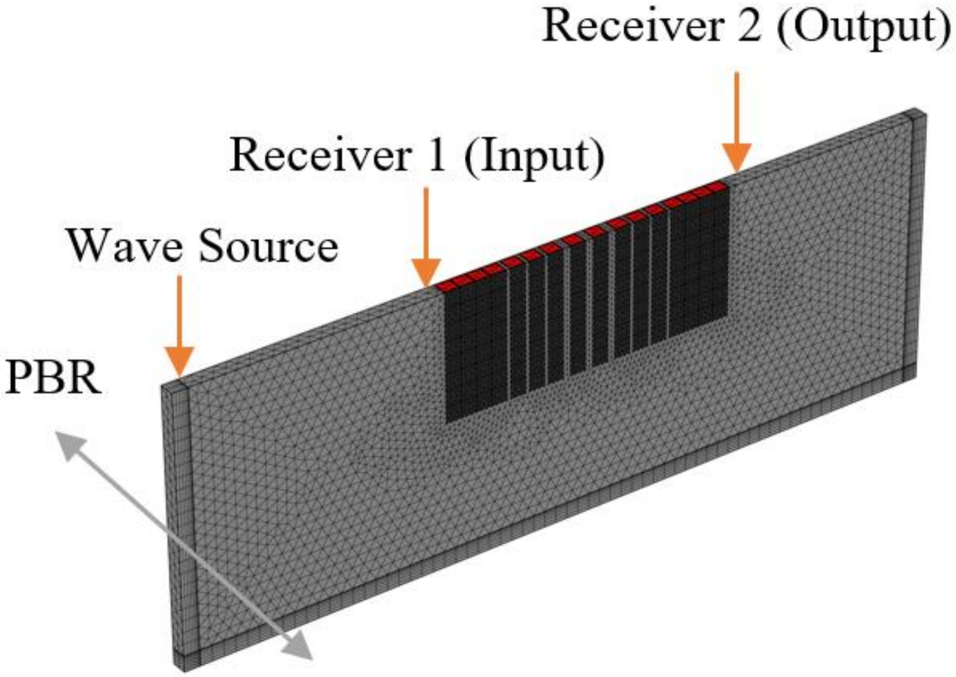

Figure 4-33: Frequency domain analysis using the full model.

The transmission from receiver 1 to receiver 2 when surface waves are applied is shown in Figure 4-34. It compares the transmission between receiver points 1 and 2 when double-graded unit cells are used (Blue line) and when the double-graded unit cells are not used (Orange line). It is observed that the frequencies that fall within the bandgap are blocked (Grey shaded area), and additional frequencies less than the lower bandgap limit were blocked, specifically in the range of 3.5 – 4.5 Hz (Marked in green circle). Moreover, the double-graded configuration blocked all frequencies higher than the theoretical upper bandgap limit (Marked in orange circle). Therefore, when a structure is subjected to surface waves in the range of 0 to 30 Hz (Most disastrous frequencies), the double-graded metamaterial configuration can block all the waves between 3.5 – 29.8 Hz, nearly 88% of the most disastrous seismic waves. The same observations and conclusion can be seen when comparing the displacement at receiver point 2 between using a double-graded configuration and without it, as shown in Figure 4-35.

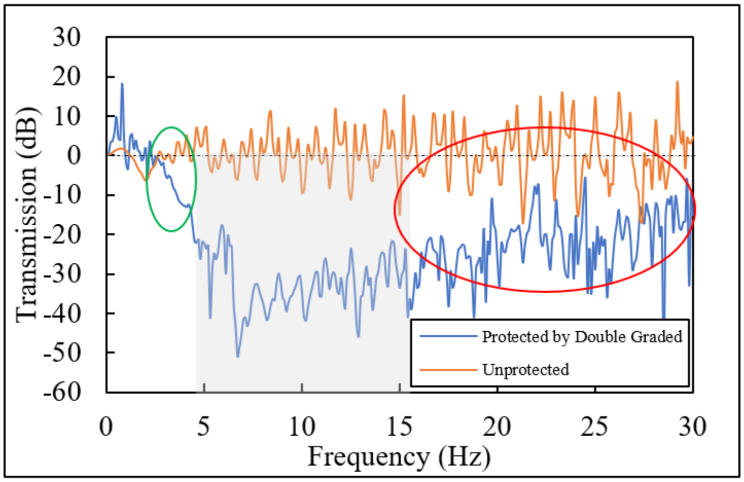

Figure 4-34: Transmission for double-graded configuration compared to a soil medium without protection subjected to surface waves.

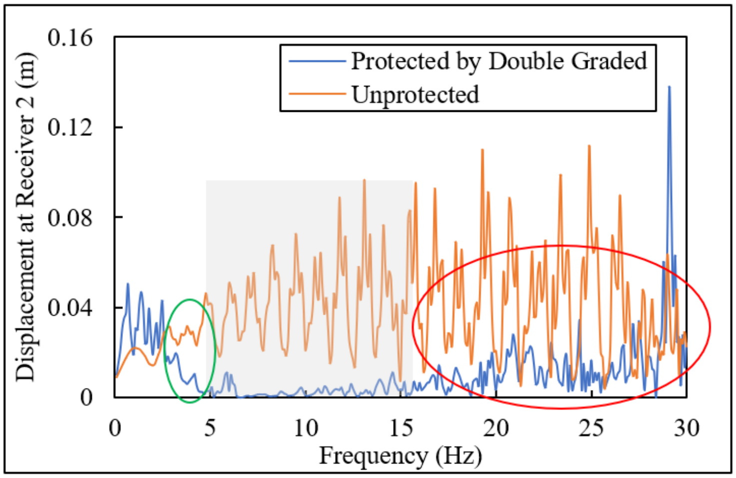

Figure 4-35: Recorded displacement at the receiver point 2 for double-graded configuration compared to a soil medium without protection subjected to surface waves.

Similarly, when comparing the transmission between receivers 1 & 2 when the medium is subjected to bulk waves, the complete bandgap (Grey shaded area in Figure 4-36) is blocked.

Additionally, more frequencies above the upper bandgap limits are blocked, as shown in Figure 4-36.

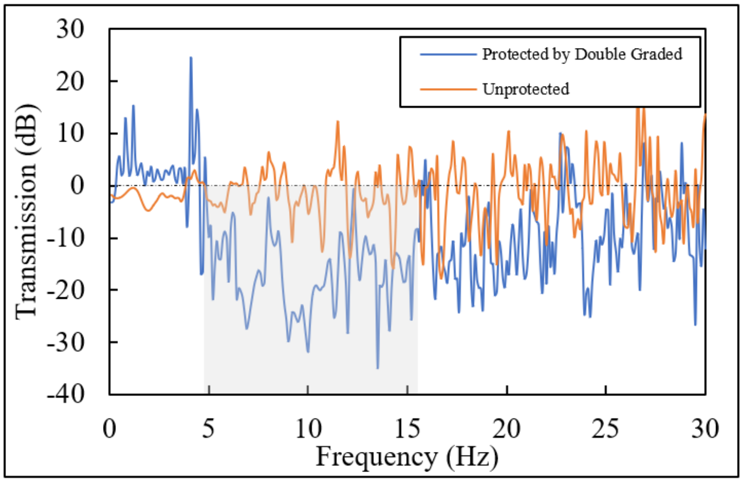

Figure 4-36: Transmission between receivers 1 and 2 for double-graded configuration compared to a soil medium subjected to bulk waves without protection.

Furthermore, Figures 4-37 to 4-39 show the displacement variation along a line that extends from the wave source to the first third of the unit cells with 60 m length for waves with 5.3 Hz, 10.8 Hz, and 14.7 Hz frequencies, respectively. Once the wave launches from the source, it loses some of its amplitude due to the linear properties of the soil medium as it absorbs some of the wave energy. Thereafter, the waves propagate through the soil medium until it reaches the meta-barriers. The meta-barriers reflect some of the wave energy, divert the direction of another part, and absorb the remaining part, leading to structure protection.

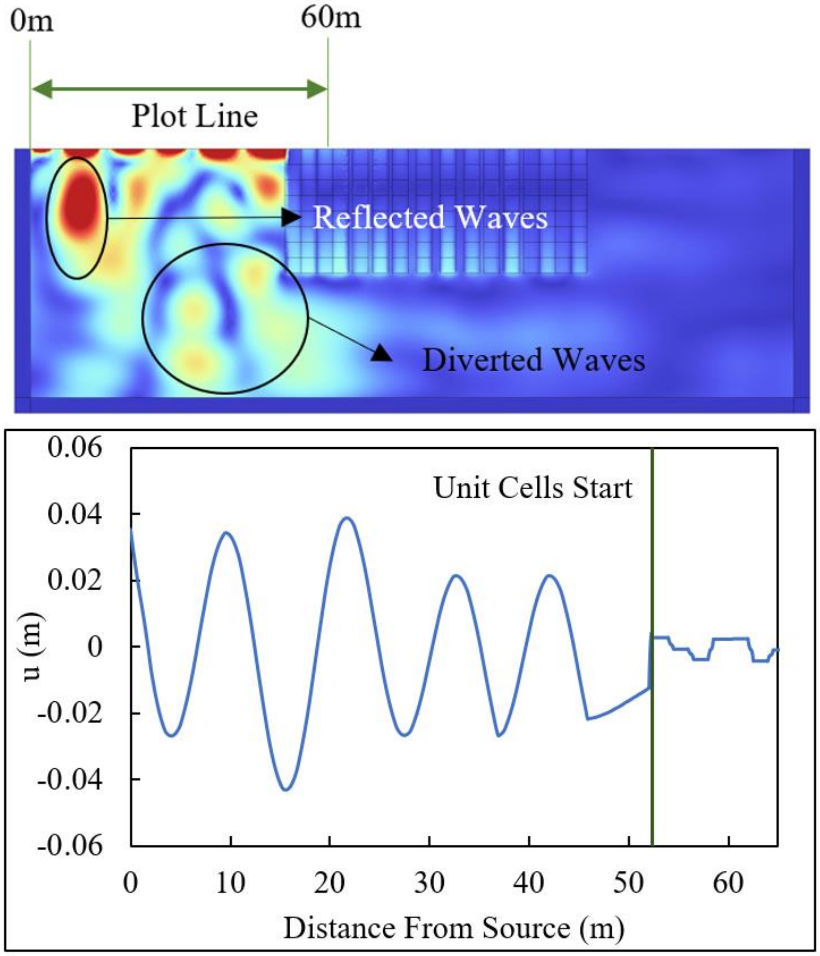

Figure 4-37: Displacement caused by surface waves with a frequency of 5.3 Hz along the top surface of the medium.

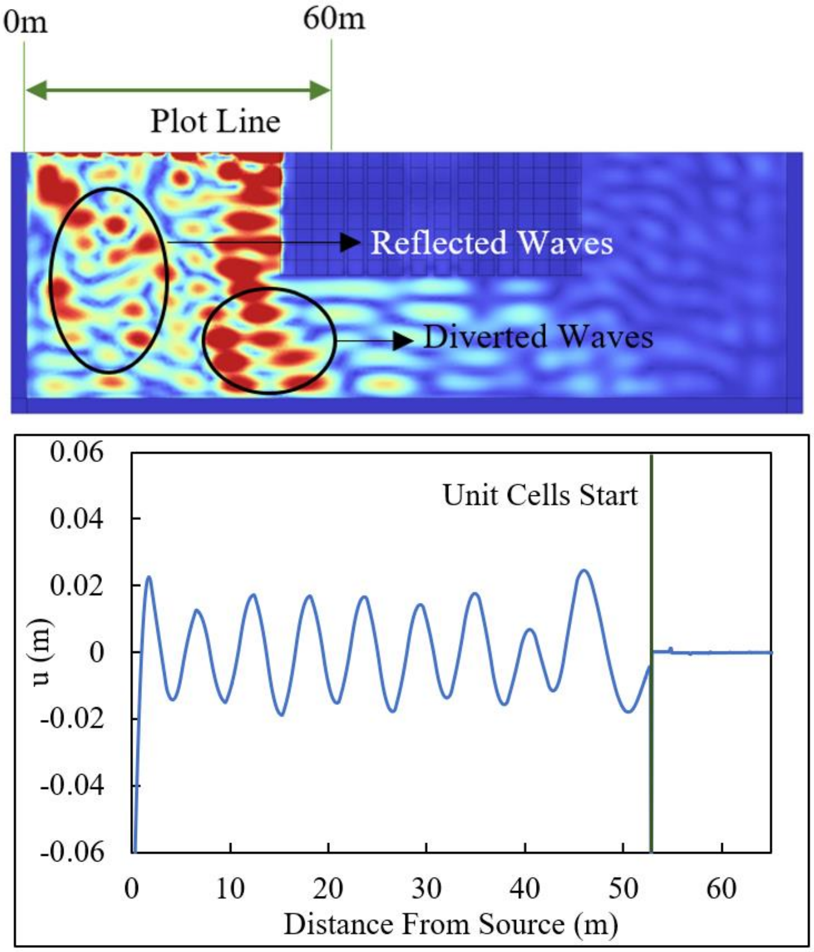

Figure 4-38: Displacement caused by surface waves with a frequency of 10.8 Hz along the top surface of the medium.

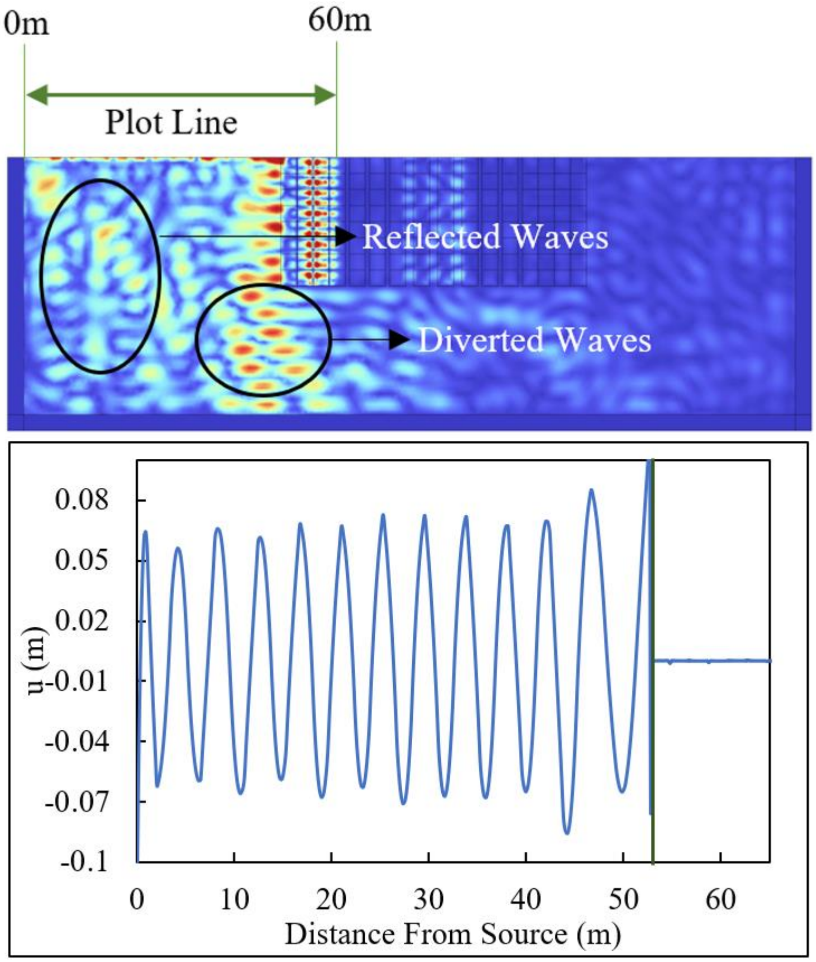

Figure 4-39: Displacement caused by surface waves with a frequency of 14.7 Hz along the top surface of the medium.

4.6. Effects of Using Double-Graded Meta-barriers on Response of a SDOF Structure

The resonance frequency of a structure is the frequency where a structure resonates the most when subjected to a small load/displacement in the range of that frequency. It can be obtained as discussed in section 3.1.3. the purpose of this study is to investigate the effects of protecting a structure with metamaterial and to see its effects on the structural response of a structure at the peak frequency. To this end, a single degree of freedom (SDOF) structure has been modeled, and its resonance frequency is analyzed. For the SDOF structure a lumped mass model is adopted, where a concentrated translational mass is supported by a column (beam element) and is supported on a fixed support. This can also be idealized as a mass-spring model. Figure 4-40 shows the two different methods for modeling the SDOF.

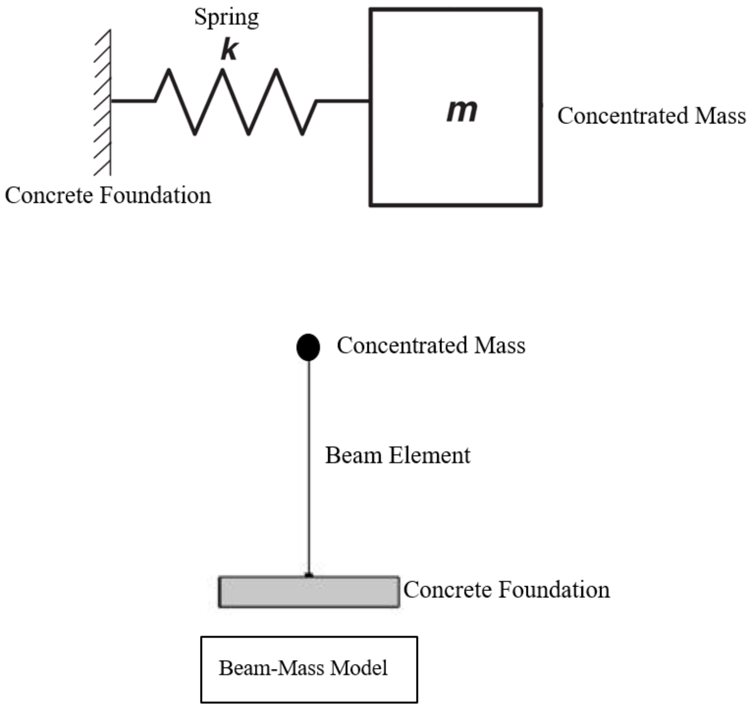

Figure 4-40: Methods of modeling the SDOF structure.

To verify the methods of modeling SDOF structure, the proposed models in Figure 4-40 were simulated using COMSOL Multiphysics. 40 Tons mass on top was considered, and a column with equivalent stiffness of 9.8 x 10^7 N/m was considered. Moreover, a 6x1 m concrete foundation was considered as a support to the SDOF. Three peak resonance frequencies were obtained using the spring-mass model, beam-mass model, and using the formulation, as discussed in section 3.1.3. The results are shown in Table 4-15. The results showed that all models would have the same peak resonance frequency of 7.4 Hz. However, the obtained amplitude from the formulation and spring-mass model differed from the beam-mass model by less than 4%. This is because the formulation and the spring-mass model are idealized cases and do not consider the exact interaction between column-mass and column-foundation. Therefore, the beam-mass model will be used to evaluate the double-grading meta-barriers on the peak response of the SDOF at different excitation frequencies.

Table 4-15: Results of simulating SDOF structure using three different methods.

Model	F_n (Hz)	Amplitude (m)
Formulation	7.400	15.42
Spring-Mass	7.405	15.42
Beam-Mass	7.394	14.87

The natural frequency curve of the selected SDOF is shown in Figure 4-41, where the natural period is at 7.4 Hz.

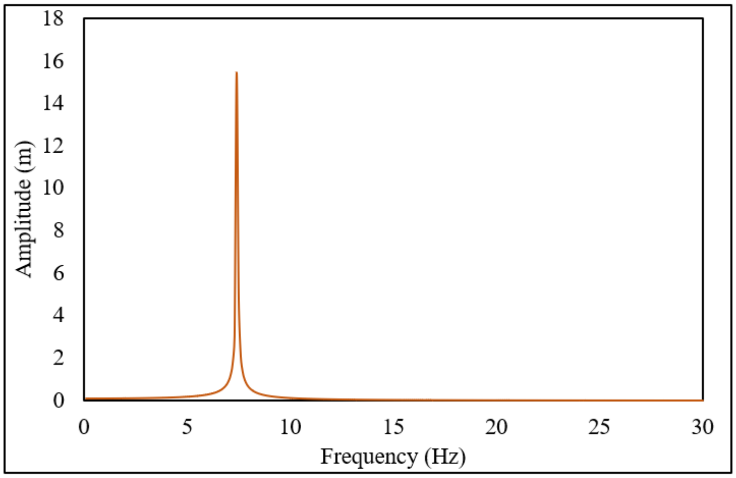

Figure 4-41: Selected SFOF natural frequency curve.

Furthermore, a model was developed in the frequency domain, which will be used to study the effects of using double-graded configurations on an SDOF structure peak response. Figure 4-42 shows the dimensions of the FEA model for this purpose.

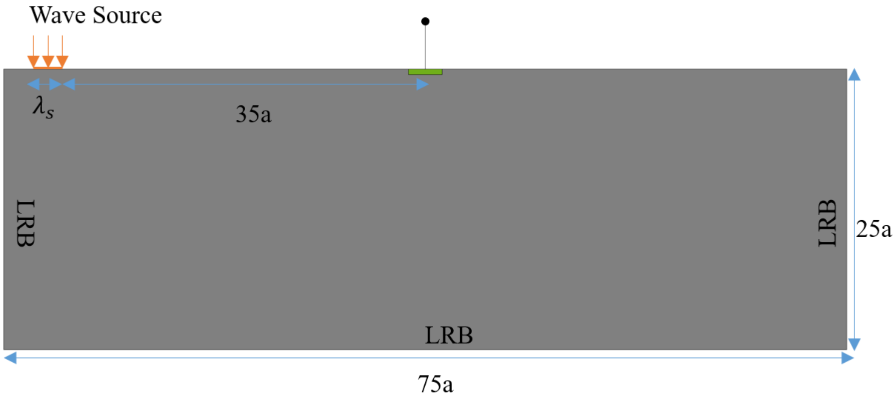

Figure 4-42: FEA model for the frequency domain analysis including the SDOF structure.

Furthermore, four reference points were selected for the sake of comparison between different configuration; P0 is immediately before the meta-barriers, P1 is immediately after the meta-barriers, P2 is at the intersection point between the foundation and the column, and P3 is at the top of the SDOF structure as shown in Figure 4-43.

Figure 4-43: Reference points used to evaluate the effectiveness of the meta-barriers for SDOF structure.

Figure 4-44 shows the concept of using meta-barriers to protect a structure by surrounding the structure with meta-barriers from all sides. This concept can protect sensitive structures such as but not limited to remote nuclear power plants or any other remote structure. It can also be used to protect a small city by surrounding the city with such meta-barriers.

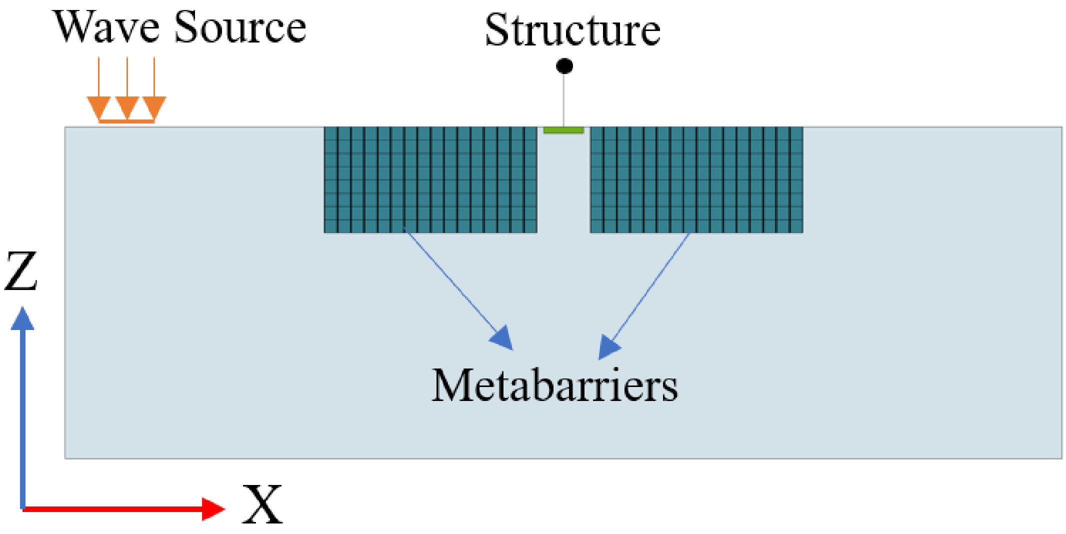

Figure 4-44: Using meta-barriers to protect structures from seismic waves.

Initially, two models were evaluated, double-graded array (DGA) and stacked unit cells (A). Figure 4-45 shows the initial two models.

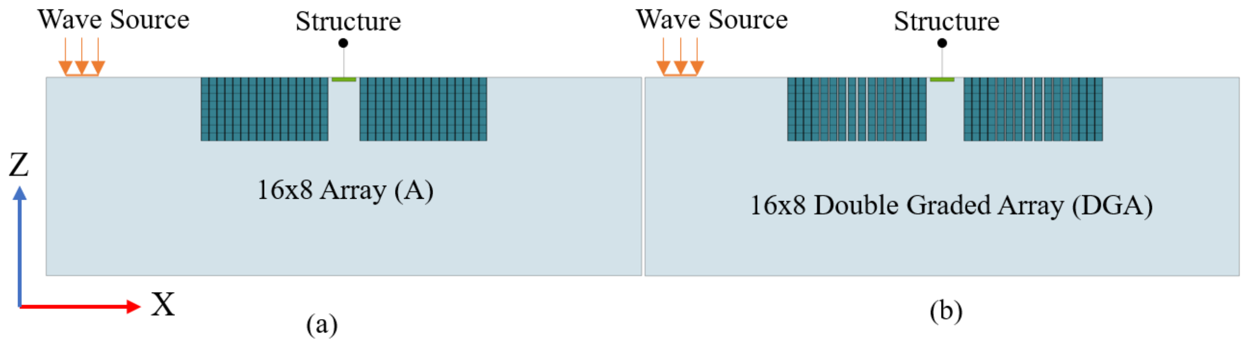

Figure 4-45: Primary evaluated models, (a) stacked unit cells, and (b) double graded design.

Figure 4-46 shows the horizontal displacement amplitude at points P0 and P1 for the initial two models compared to a model without unit cells (F). It is observed that the DGA model reflects fewer waves than the stacked unit cells. This can be seen in the displacement amplitude at P0, where the displacement at frequencies within the bandgap range is higher in the case of stacked unit cells. This is because the DGA configuration absorbs the incoming waves and diverts the direction of part of the incoming waves to the ground. When comparing the displacements between using unit cells and without protection, the model without protection showed less displacement since all the waves are propagating without any reflection from the unit cells.

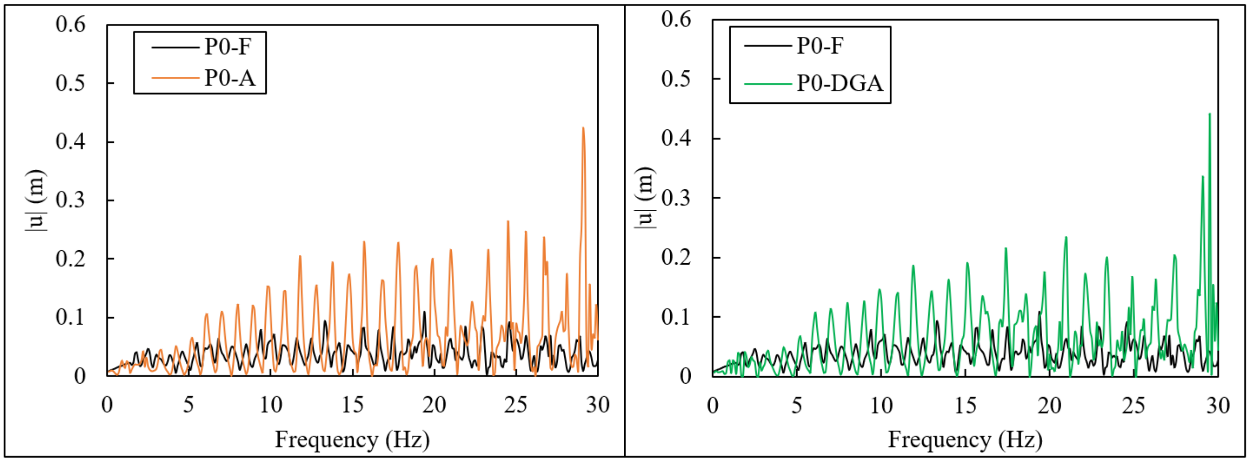

Figure 4-46: Horizontal displacement amplitude at P0 comparison between protected structure and without protection.

Furthermore, when comparing the displacement immediately after the unit cells (P1), both configurations block all frequencies within the bandgap. However, the DGA significantly reduces the wave amplitude higher than the upper bandgap limit, as shown in Figure 4-47.

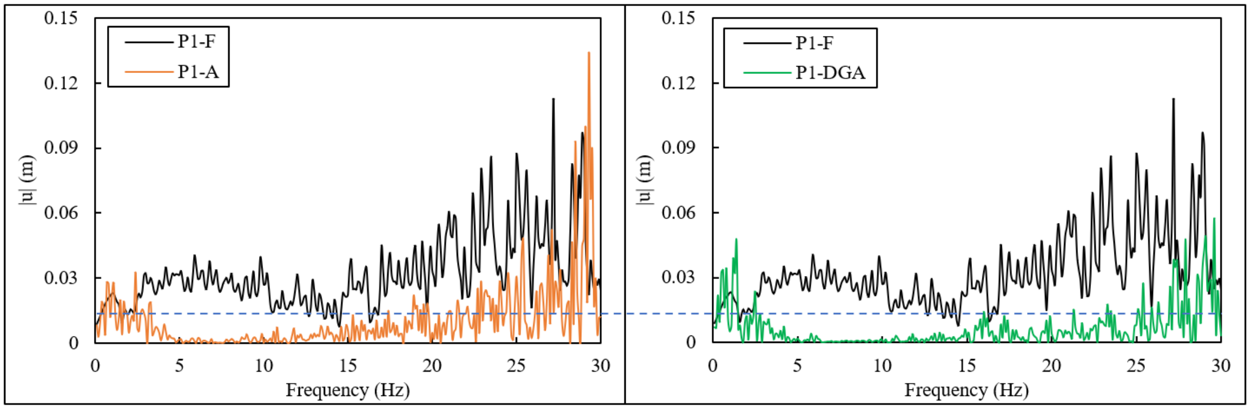

Figure 4-47: Horizontal displacement amplitude at P1 comparison between protected structure and without protection.

Moreover, Figure 4-48 shows the horizontal displacement amplitude at the top of the structure (P3). It is observed that the double-graded array (DGA) caused additional amplification at the

SDOF structure peak resonance frequency and reduced the amplification elsewhere. This is considered a drawback of using a double-graded configuration. Therefore, it is necessary to modify the DGA to prevent additional amplification at the peak resonance frequency.

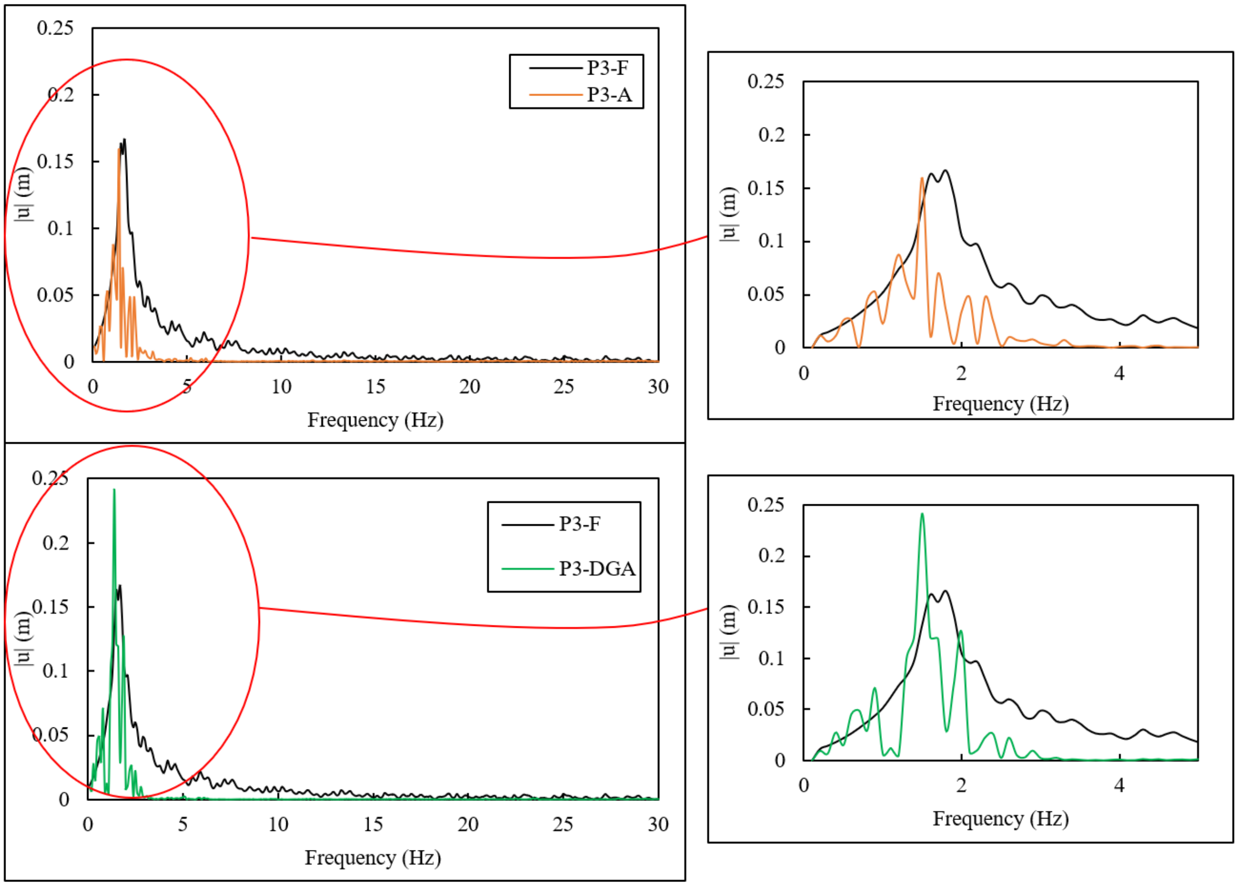

Figure 4-48: Horizontal displacement amplitude at P3 comparison between protected structure and without protection.

To this end, instead of changing the scheme of the configuration, changing the combination of the unit cell, or adding additional unit cells, the additional amplification is eliminated by removing some of the DGA unit cells so that the configuration looks like a double-graded pyramid (DGP). Figures 4-49, 4-50, and 4-51 show the performance of DGA against DGP at reference points P0, P1, and P3, respectively.

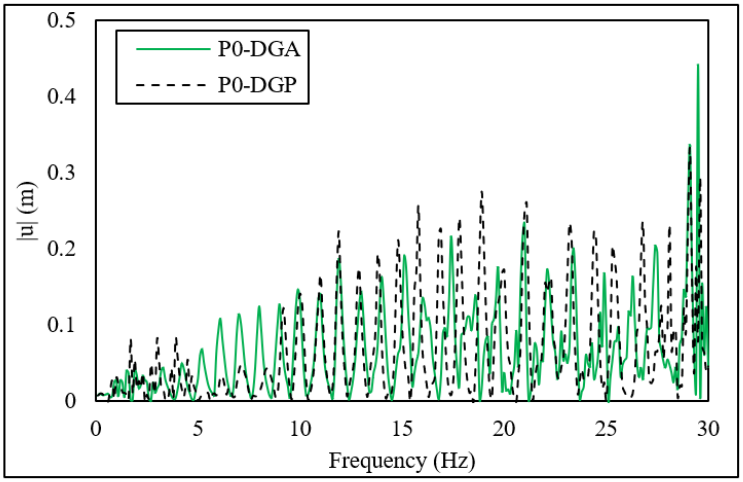

Figure 4-49: Horizontal displacement amplitude at P0 comparison between double-graded array and double-graded pyramid.

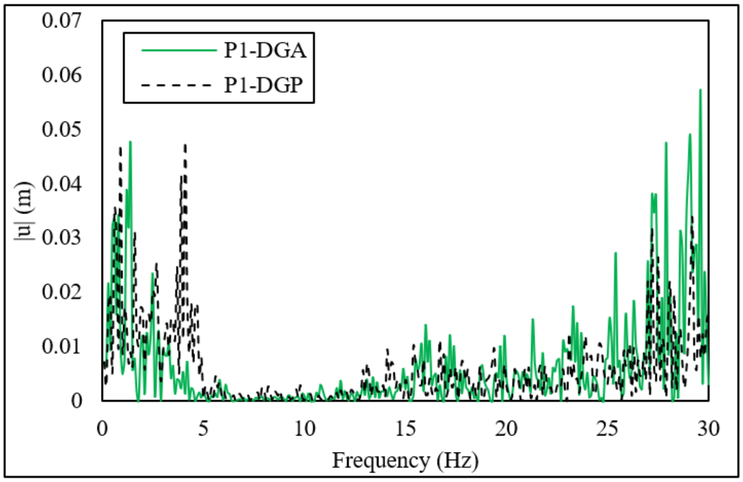

Figure 4-50: Horizontal displacement amplitude at P1 comparison between double-graded array and double-graded pyramid.

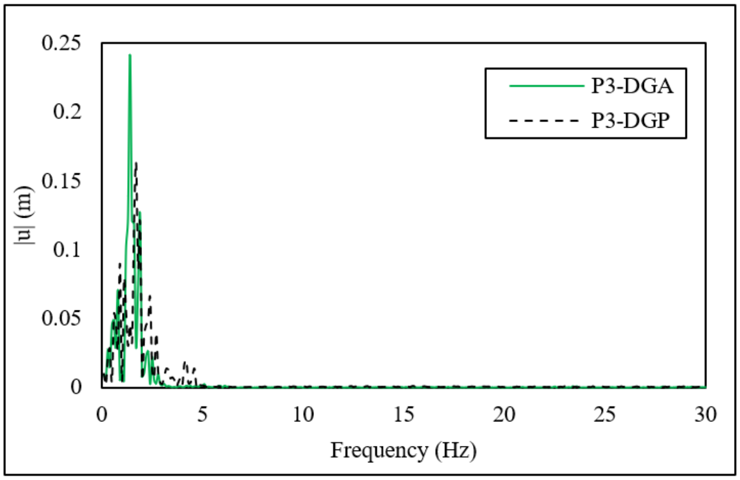

Figure 4-51: Horizontal displacement amplitude at P3 comparison between double-graded array and double-graded pyramid.

It is observed that the double-graded pyramid performs nearly the same as the double-graded array in terms of absorbing the incoming waves (Figure 4-49). Moreover, Figure 4-50 shows that the DGP provides better protection in the bandgap range and up to 30 Hz, whereas the displacements in Figure 4-50 show less amplitude except for 4.5 Hz frequency. Finally, the DGP allows less amplification at the SDOF peak resonance frequency, as seen in Figure 4-51. Therefore, to eliminate the additional amplification at the peak resonance frequency, the DGA unit cells should be reduced instead of increased so that the new configuration would divert more waves to the ground and provides better protection than the proposed configuration. The DGP configuration is shown in Figure 4-52, where the number of unit cells in the vertical direction has been reduced periodically to form a pyramid-like configuration, while the number of unit cells along the horizontal direction remained the same as in the DGA with 16-unit cells.

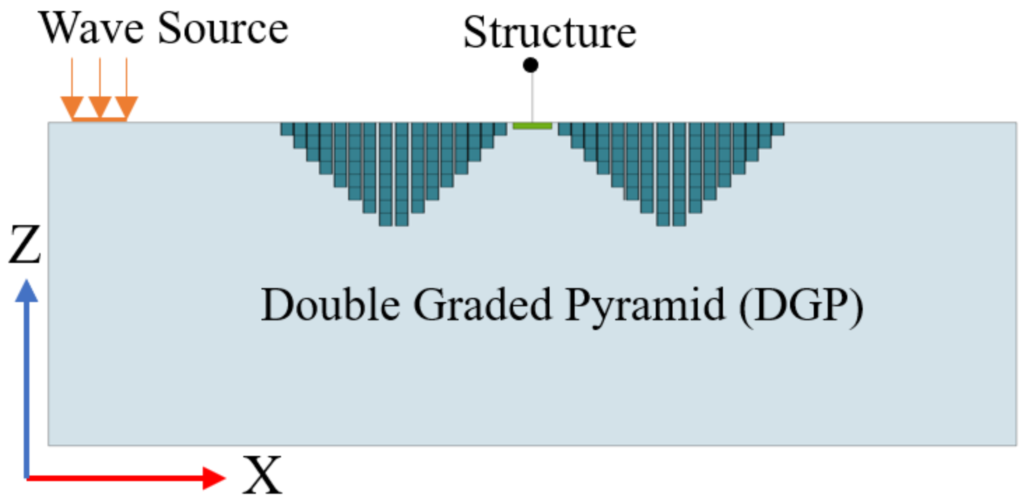

Figure 4-52: Final proposed configuration, pyramid-like double-graded configuration.

Finally, displacement contours at different frequencies for the three evaluated models are shown in Figures 4-53, 4-54, and 4-55 for frequencies of 2.3 Hz, 8.8 Hz, and 19 Hz, respectively. The protection is visible in all figures as the displacement after the unit cells are absorbed to nearly 0 m. Furthermore, the double-graded pyramid diverts the wave's direction to the ground rather than reflecting it to the source, as seen in the arrows on the figures. Additionally, the displacement before the unit cells is more concentrated in the stacked unit cells and the double-graded array than in the double-graded pyramid. This is due to the capability of the double-graded pyramid to divert the wave's direction rather than reflecting it.

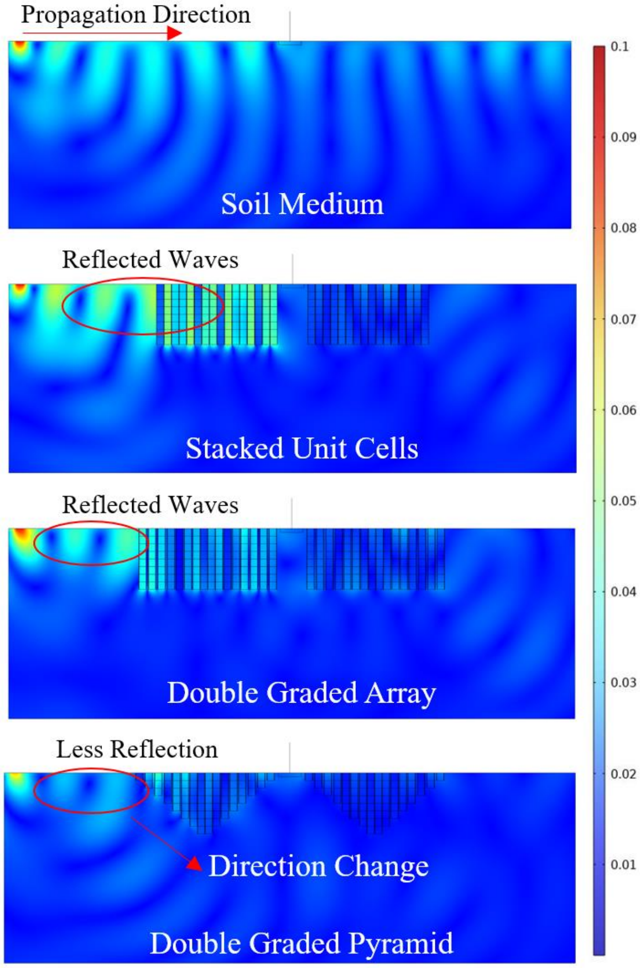

Figure 4-53: Displacement contours comparison for the evaluated configurations subjected to 2.3 Hz harmonic wave.

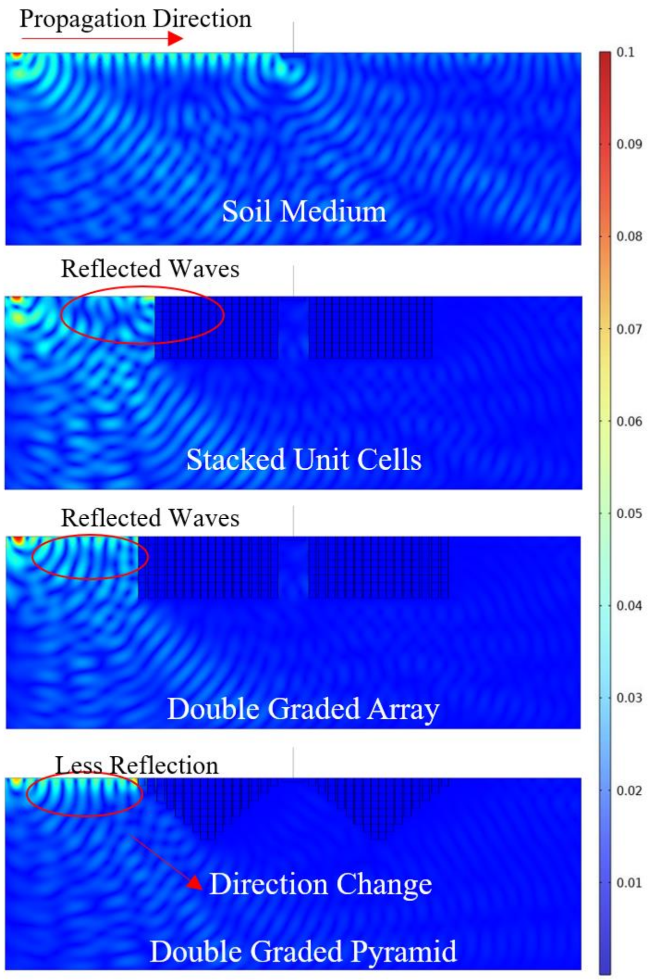

Figure 4-54: Displacement contours comparison for the evaluated configurations subjected to 8.8 Hz harmonic wave.

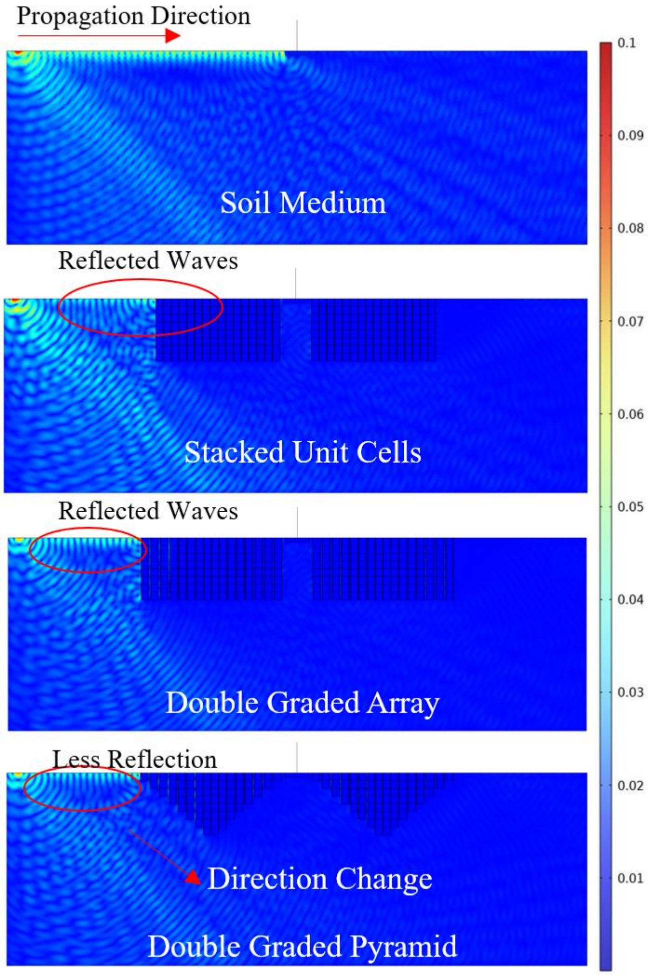

Figure 4-55: Displacement contours comparison for the evaluated configurations subjected to 19 Hz harmonic wave.

4.7. Performance Evaluation of Meta-barriers in the Time Domain

The final evaluation step is simulating the double-graded array and pyramid in the time domain where three types of wavelets are applied: Ormsby wavelet, Ricker wavelet, and a real-life seismic event, as discussed in section 3.5.

Ormsby wavelet was selected because it can be used to apply multiple frequencies in a very short time with four frequencies applied: f_4, f_3, f_2, and f_1 are 30 Hz, 27.5 Hz, 2.5 Hz, and 0.1 Hz, resulting in a wave with frequencies ranging from 0.1 to 30 Hz in less than a second (See Fig. 3.18). As shown in Figure 4-56, when Ormsby wavelet is applied and generated, all four main types of seismic waves are observed.

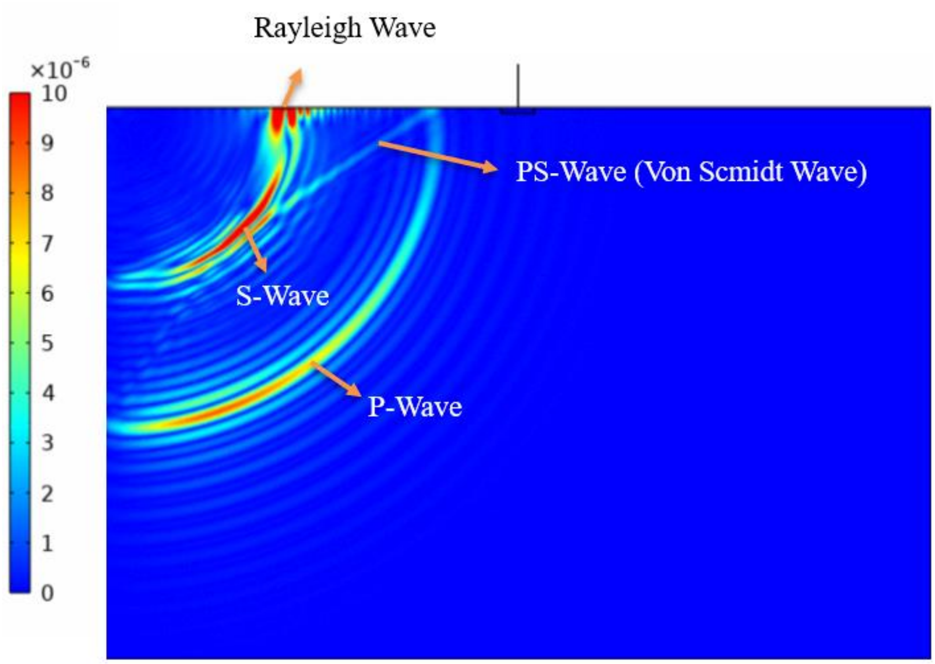

Figure 4-56: Types of waves generated in a soil medium subject to low-amplitude displacement in type domain using Ormsby wavelet.

Figure 4-56 shows that both body waves (P and S waves) are the fastest and first to propagate and reach the structure. Additionally, the amplitude of such waves is observed to be higher as they propagate deep to the ground, while their amplitude along the surface is minimal and decreases as they propagate through the medium. Moreover, surface waves (Rayleigh and Love waves) can be observed as they propagate slower than the body waves and only along the surface. Additionally, their amplitude is greater than body waves, and they only propagate at the surface, which is why they are considered the most disastrous waves.

The result of the Ormsby wavelet application is shown in Figure 4-57, which is a comparison between the observed displacement at the top of an SDOF structure placed in a soil medium without protection (Soil, shown in the blue line in Figure 4-57) and with protection using two types of configurations: double graded array (Grey line) and double graded pyramid (Orange line). The result showed that both protection configurations protected the structure from all incoming waves for the specified time, with the observation that the double-graded pyramid is more efficient than the array because the double-graded pyramid can divert the waves rather than reflect them. The result showed that the graded array protected the structure from 80% of the incoming waves, and the double-graded pyramid protected the structure from 90% of the wave energy. Furthermore, Figures 4-58, 4-59, and 4-60 show the contours of the wave at 0.70, 1.1, and 1.7 seconds respectively. All types of waves (P, S, and surface waves) can be observed in the figures. Additionally, the waves can be seen propagating towards the SDOF until they hit the meta-barriers, where wave reflection can be observed from the double-graded configurations (middle and bottom in Figure 4-58). Moreover, the double-graded array reflected more waves than the pyramid, as seen in the red-marked circle.

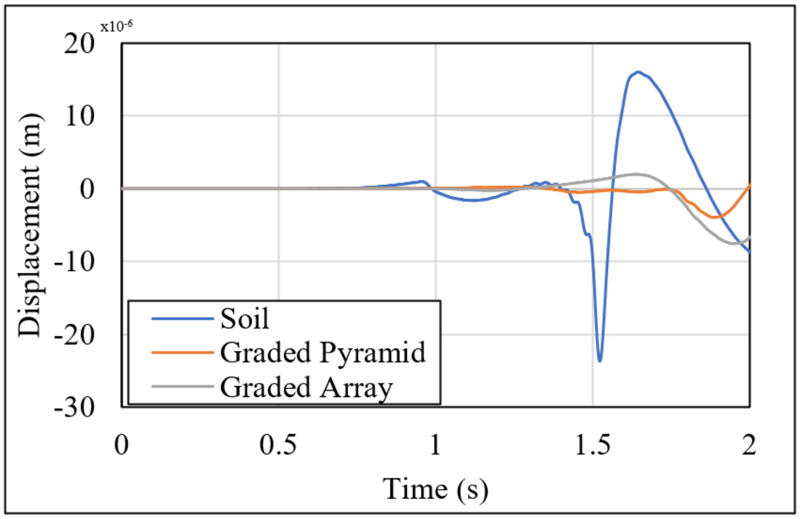

Figure 4-57: Displacement comparison at the top of an SDOF structure with and without protection with a double-graded array and a double-graded pyramid.

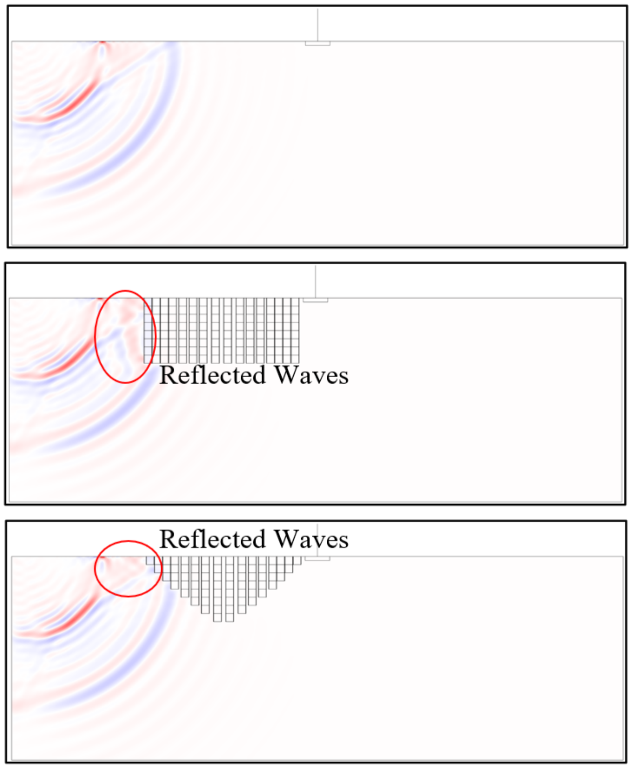

Figure 4-58: Wave contours generated by Ormsby wavelet at 0.7 seconds with different configurations (Top) soil medium without protection, (Mid) protection using a double-graded array, and (Bottom) protection using a double-graded pyramid.

Furthermore, at 1.1 seconds (Figure 4-59), the P-wave already arrived and passed the structure without protection (Top in Figure 4-59). However, when the structure is protected, the meta-barriers absorb part of the P-wave, reflect it partly, and change the direction of the third part. The peak acceleration has been reduced by 68% and 75% when graded array and graded pyramid are used, respectively. Furthermore, the acceleration square root of mean squares (RMS) has been reduced by 50% and 67% when graded array and graded pyramid are used, respectively.

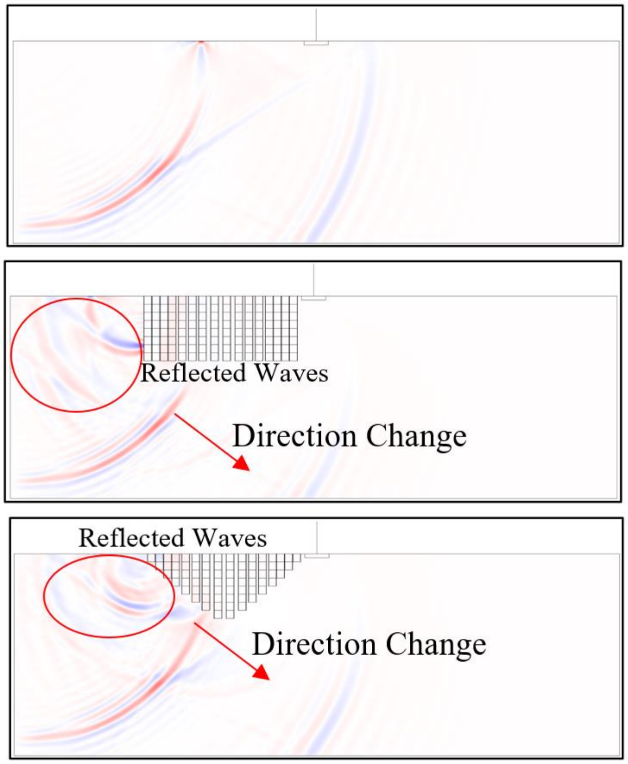

Figure 4-59: Wave contours generated by Ormsby wavelet at 1.1 seconds with different configurations (Top) soil medium without protection, (Mid) protection using a double-graded array, and (Bottom) protection using a double-graded pyramid.

Finally, at 1.7 seconds (Figure 4-60), the waves arrived at the structure and can be seen reflected towards the source, propagated through the structure and to the top, causing displacement in the structure. Furthermore, the structure appears to be protected from the incoming waves when meta-barriers are used as they absorb and reflect the incoming waves.

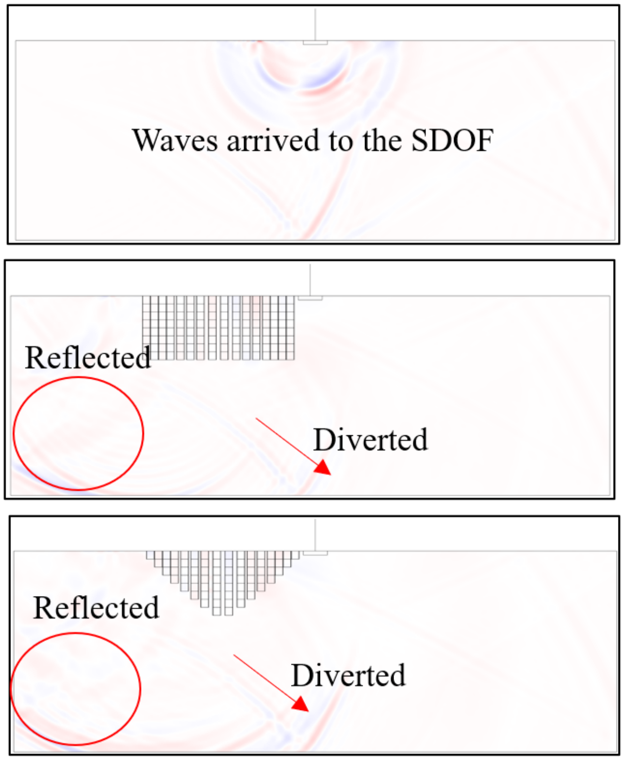

Figure 4-60: Wave contours generated by Ormsby wavelet at 1.7 seconds with different configurations (Top) soil medium without protection, (Mid) protection using a double-graded array, and (Bottom) protection using a double-graded pyramid.

To verify that the double-graded pyramid can divert waves direction more than absorb it, a point halfway through the distance between the wave source and the unit cells was selected. Figure 4-61 shows the displacement at the aforementioned point. The results include the displacement in both directions, i.e., both propagated and reflected waves. Since the curves include the forward and backward propagating waves at that point, higher displacement means more reflection. Since the displacement while using the graded pyramid is lower at that point (Blue circled area) than the double-graded array, the double-graded pyramid diverts more waves than reflecting it. The acceleration RMS is 7% higher at the input node when the double graded array is used compared to the double graded pyramid.

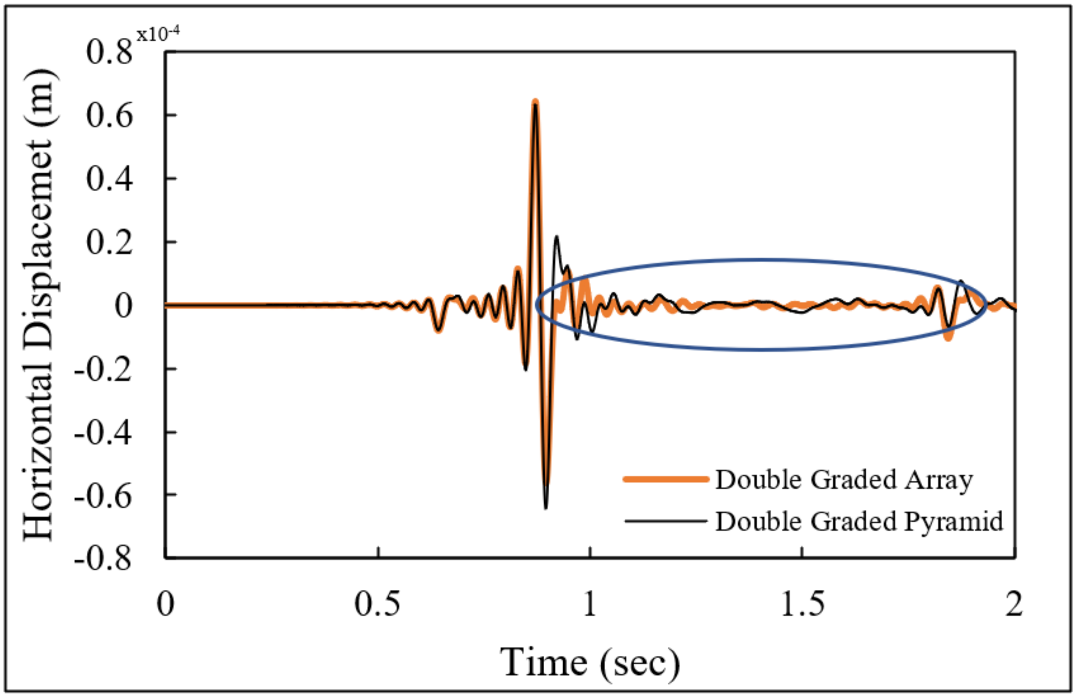

Figure 4-61: Horizontal displacement at a point between the metabarriers and the wave source (Ormsby Wavelet).

Furthermore, for the same proposed configurations, the Ricker wavelet is applied, as shown in Figure 3-19, with a peak frequency of 1.7 Hz, which is equal to the SDOF peak resonance frequency when placed in the soil medium. Surprisingly, both the double-graded array and pyramid blocked the whole wave and prevented it from arriving at the structure, as shown in Figure 4-62. Moreover, the displacement at a point between the meta-barriers and the wave source was captured, and the results are shown in Figure 4-63. Since the displacement at that point includes all forward and backward displacements, higher displacement means more wave reflection. Therefore, the double-graded pyramid shows less displacement at the point than the double-graded array, which means the double-graded array reflects more waves than the double-graded pyramid, and the double-graded pyramid diverts the waves rather than reflecting them.

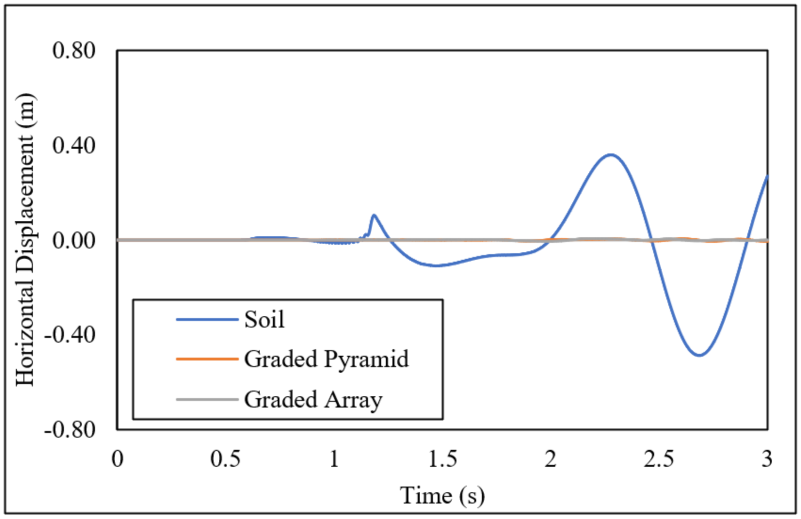

Figure 4-62: Horizontal displacement at the top of the SDOF subjected to Ricker wavelet.

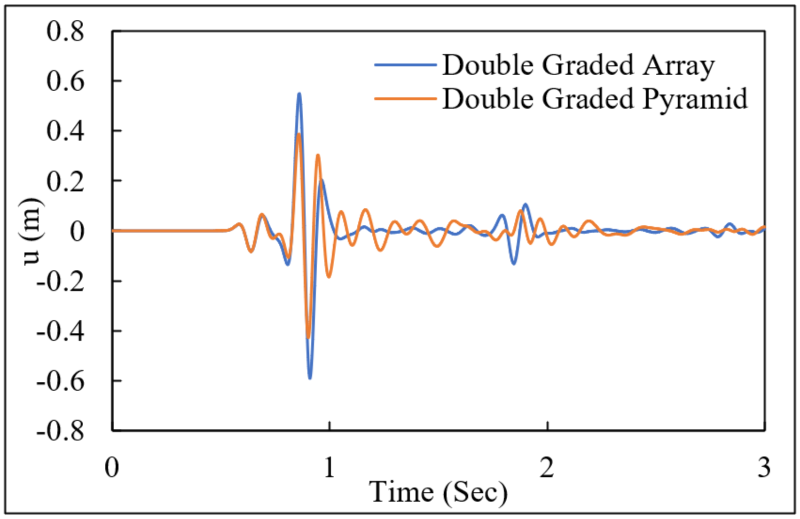

Figure 4-63: Horizontal displacement at a point between the meta-barriers and the wave source (Ricker Wavelet).

Finally, real-life seismic event data has been used to evaluate the effects of using double-graded meta-barriers on SDOF structure acceleration, as discussed in section 3.5. The evaluation results of the real-life seismic event show that the double-graded pyramid can efficiently attenuate seismic waves and can divert the wave's direction more than reflecting it compared to the double-graded configuration. Figure 4-64 shows the input normalized acceleration at the input receiver (P0in Figure 4-43). It is observed that the DGP model input acceleration is lower than the DGA model. Since the input receiver captures both forward and backward going waves, it includes initially propagating and reflected waves. Since the DGP model showed less acceleration at that receiver, and the same forward propagating amplitude for all three models. It is evident that the DGP design diverts the waves to the ground rather than reflecting them back towards the source and the model without protection showed the lowest input acceleration since no reflection is present and all waves are propagating to the other end of the model. Moreover, the input acceleration seems lower at the input node of DGP when compared to the input node of DGA. This is because a pyramid-like configuration can divert the wave direction rather than reflect it since the input node includes all forward and backward propagating accelerations.

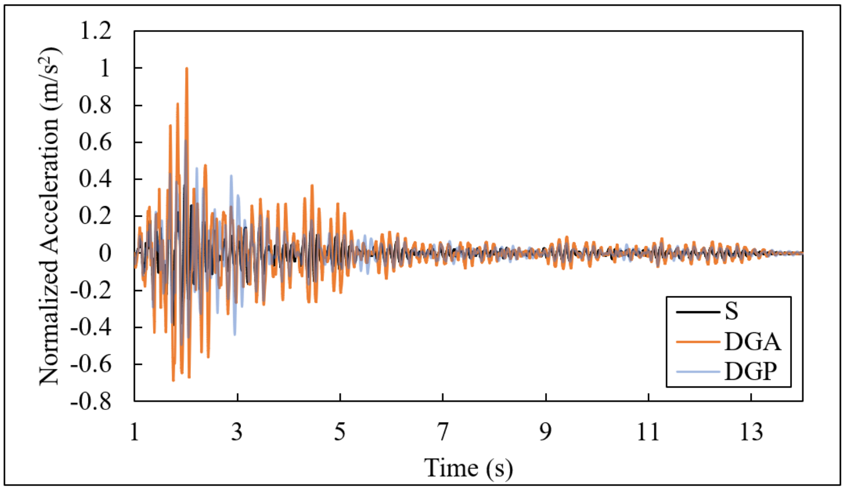

Figure 4-64: Input acceleration at nodes P0 comparison between unprotected model and protection by DGA and DGP.

Moreover, Figure 4-65 shows the Fourier amplitude of Oroville time histories at the input receiver. The result shows that the DGP model diverts the waves with frequencies that fall in the bandgap range.

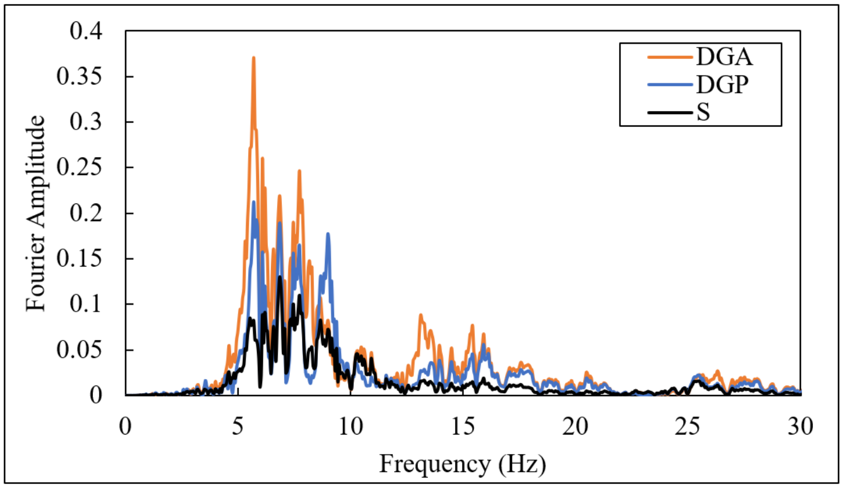

Figure 4-65: Fourier amplitude of the input acceleration comparison between proposed designs.

Finally, Figure 4-66 show the normalized acceleration at the output receiver for the proposed designs compared to a model without protection. The results show that DGA can attenuate most seismic waves as a significant reduction in wave amplitude is observed. Moreover, the number of peaks in the plot is reduced at the output point due to the complete block of all frequencies that fall within the unit cell bandgap. The same observation for the acceleration was observed when using a double-graded pyramid-like configuration (DGP), as shown in Figure 4-66. The peak acceleration has been reduced by 70%, and 66% when DGA and DGP are used, respectively. Additionally, the acceleration RMS has been reduced by 67%, and 64% when DGA and DGP are used, respectively.

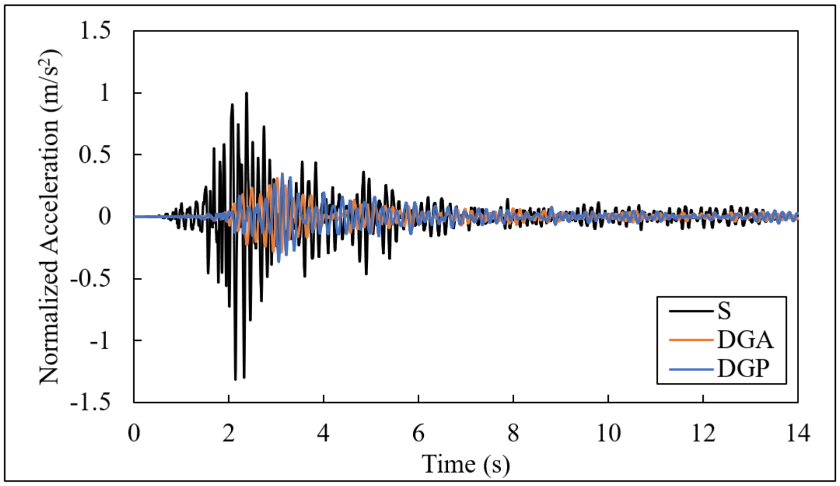

Figure 4-66: Normalized output acceleration at the P1 for the proposed designs compared with model without protection.

Additionally, when comparing the output acceleration (at node P1) and the acceleration at the top of the SDOF (node P3), the amplification from bottom to top is different in each case. When soil alone without protection (S), the acceleration at (Figure 4-67 top-left) seems to be transmitted from the bottom to the top of the SDOF. Moreover, the Fourier amplitude (Figure 4-67 top-right) shows that the SDOF significantly amplified the wave at the peak resonance frequency of 1.7 Hz. Furthermore, Figure 4-67 (Mid-left) shows the acceleration comparison of P1 versus the acceleration at the top of the structure for a structure protected by double-graded configuration (DGA), where generally, there was amplification in almost all the periods. However, the number of peaks is reduced because the unit cells attenuated all frequencies within the bandgap.

Moreover, due to the periodic grading arrangement, the DGA model protected the structure from all frequencies above 3.0 Hz, which is not in the bandgap limit. This can be confirmed by looking at the Fourier amplitude of the DGA (Mid-right) at the SDOF peak resonance frequency (1.7 Hz). The structure significantly amplified the wave to a value higher than that of a structure without protection, which is considered a drawback of using the double-graded configuration. The double-graded pyramid-like configuration (DGP) was developed to overcome this drawback. As shown in Figure 4-67 (Bottom-left), the number of peaks is reduced, and all frequencies that fall in the bandgap are attenuated by the unit cells. Figure 4-67 (Bottom-right) shows the Fourier amplitude for a structure protected by a double-graded pyramid-like configuration. The DGP model reduced the amplification at the top of the structure to nearly as the model without protection.

Moreover, the DGP model reduced the amplification of the structure at frequencies lower than the bandgap (Starting at 2.0 Hz). Therefore, the double-graded pyramid-like model lowered the lower bandgap limit from 4.9 Hz to 2.0 Hz and increased the upper bandgap limit from 15.5 Hz to 29.8 Hz. Finally, the results obtained using the real-life seismic event data agree well with the frequency domain analysis, as discussed in section 4.6.

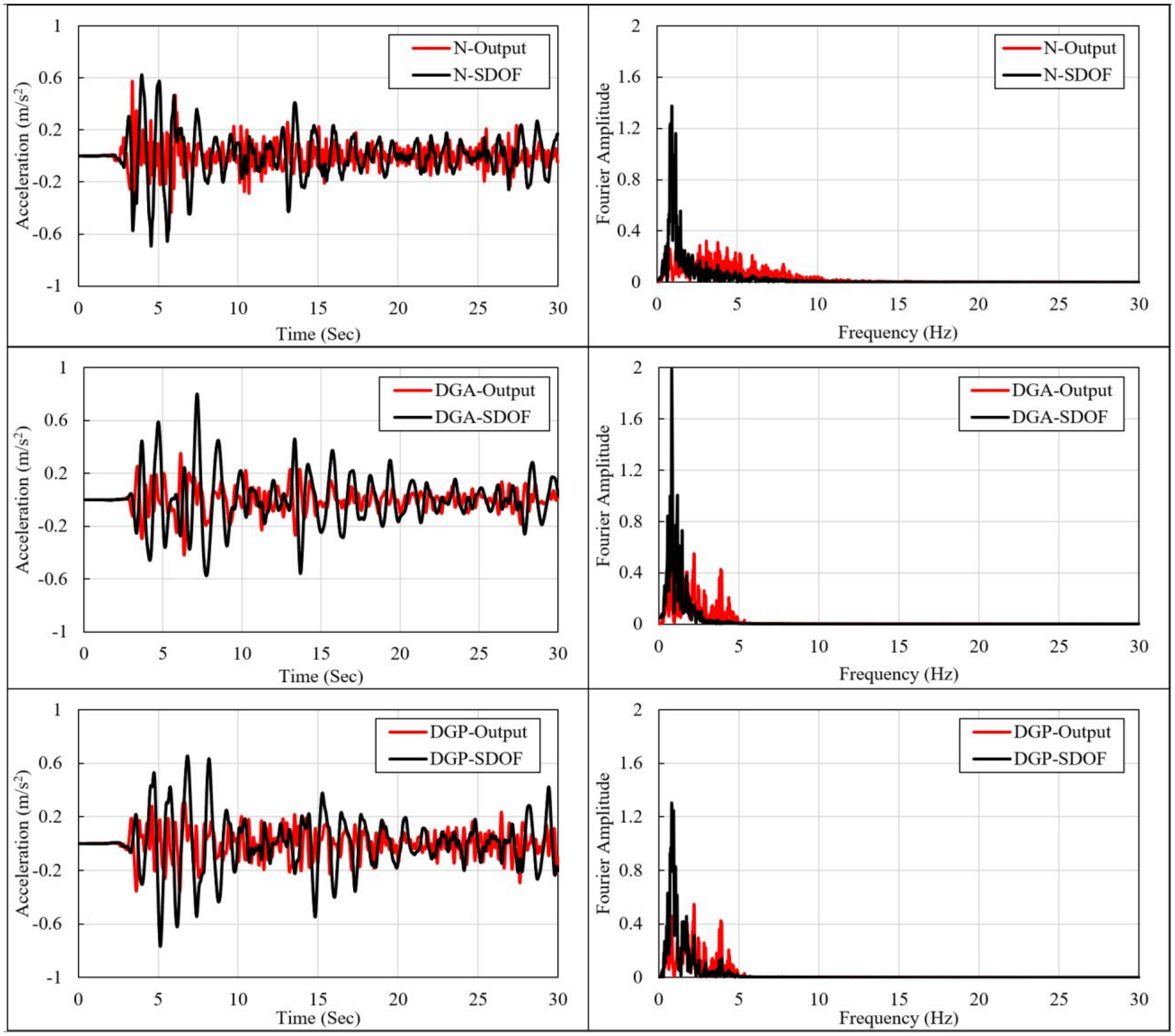

Figure 4-67: Acceleration amplitude and Fourier amplitude at nodes P1 and P3 for a soil medium (N), double-graded array (DGA), and double-graded pyramid (DGP).

CHAPTER 5 : SUMMARY AND CONCLUSIONS

5.1. Summary

Protection from seismic waves is vital due to the catastrophic and devastating effects that earthquakes can inflict on human lives, economies, and infrastructure. Earthquakes can cause widespread destruction, resulting in loss of life, injuries, and damages of communities. Damage to buildings, roads, bridges, and utilities can disrupt essential services such as water, electricity, and communication, leading to prolonged disruptions and economic losses. Rebuilding after earthquakes can be costly and time-consuming, impacting local economies and livelihoods.

Traditional seismic protection methods are techniques used to safeguard buildings and infrastructure from the damaging effects of earthquakes. These methods include seismic-resistant design and construction practices, such as reinforcing buildings with steel braces or using base isolation systems to decouple the structure from the ground motion. Other methods may include adding dampers, bracing systems, or shear walls to increase the building's stability during seismic events. Traditional seismic protection methods rely on engineering principles and materials to mitigate the forces exerted by earthquakes and minimize damage to structures. While effective, these methods may have limitations and need periodic maintenance and upgrades to remain effective in the face of evolving seismic hazards. Traditional seismic protection methods may have cost, design complexity, and effectiveness limitations against strong earthquakes, and they may also require ongoing maintenance and upgrades to remain effective in the long term. Additionally, traditional methods may not be suitable for all types of buildings or infrastructure, and their effectiveness can vary depending on local geological and soil conditions.

Therefore, a new seismic protection method has emerged in recent years based on artificially engineered materials, known as metamaterials, with exceptional properties due to their periodic effects and extraordinary properties that cannot be found naturally. This type of metamaterial has been proven to have the ability to block a specific range of frequencies from propagating and protecting a structure, new cities, bridges, railways, historical sites, and remote isolated sensitive structures from seismic waves that fall into that range. This range of frequencies is known as the attenuation zone or bandgap. In the literature, there has not been a comprehensive attempt to widen the unit cell bandgap without changing its components or size. This research aims to enlarge a unit cell attenuation zone without modifying its original features (shape, size, and materials properties). In this research, metamaterial unit cell properties that influence the bandgap were investigated, including unit cell shape, the number of materials that comprise the unit cell, mechanical properties of each layer, and the size of the unit cell components. Based on the investigation, a unit cell with the broadest possible bandgap was proposed.

The performance of the proposed unit cell was also evaluated in the frequency domain under a harmonic excitation with different frequencies in the range of destructive seismic wave (0-30 Hz). Moreover, the unit cell attenuation zone has been widened by using a double-graded configuration, that can increase both the upper and lower bounds of the bandgap.

Finally, the performance of the double-graded configuration is evaluated on the response of a SDOF structure in the frequency and time domains under two wavelets and the 1975 Oroville dam record. Results showed that the proposed configuration effectively reduces the response of the SDOF under the investigated excitations.

5.2. Key Findings and Recommendations

This study focused on achieving the broadest possible blocking range (bandgap) of meta-barriers, specifically in the range of (0-30 Hz). Moreover, the geometrical and mechanical properties that control the bandgap limits of a unit cell have been investigated. Furthermore, the study proposed a new layout for the meta-barriers to increase the frequency-blocking range of unit cells. Finally, the configuration's ability has been verified in the frequency and time domains under three excitations: Ormsby wavelet, Ricker wavelet, and a real-life seismic event. The key findings of this study can be summarized as follows:

1. Metamaterials can block specific frequencies due to their unnatural properties. This range is known as bandgap.
2. It was concluded that a unit cell made of two layers of rubber and steel could block a wide range of frequencies and is comparable to a larger unit cell in the literature (to the order of 10m). The proposed unit cell (rubber coating and steel core) can block frequencies in the range of (4.5-15.1 Hz) using analytical methods.
3. The upper bandgap limit of a unit cell is controlled by the matrix (outer layer) density.
4. The lower bandgap limit is controlled by the unit cell core (interior layer) density, which is considered the most crucial factor in controlling the width of the bandgap.
5. Young’s modulus and Poisson’s ratio do not play an important role in bandgap of the unit cells.
6. It was proven that double-graded meta-barriers (irregularly spaced unit cells) could increase the bandgap by 14.2 Hz, about twice as much as regular stacked unit cells.

7. The double-graded barriers can filter seismic frequencies in the range of (3.9-29.3 Hz) which is nearly 85% of the most destructive frequencies (0-30 Hz).
8. The double-graded configuration can reduce the amplification of a structure. However, at peak frequency, it was observed that the amplification increased by about 15%. To overcome this drawback, reducing the number of unit cells in the vertical direction is recommended, so the overall shape of the unit cells protecting the structure is a triangular-like shape (double graded pyramid).
9. Both configurations (double graded unit cells and pyramid) can reduce the amplification of a structure generally. However, the double-graded pyramid can cause additional reduction to the peak amplification of the structure.
10. Double-graded pyramid-like configuration can lower the lower bandgap limit from 4.5 Hz to 2.0 Hz and increase the upper bandgap limit from 15.5 Hz to 29.8 Hz.
11. A double-graded pyramid-like configuration can protect a structure from 91% of the most destructive wave.
12. The double-graded pyramid can divert the wave direction rather than reflect it to the source or the surrounding structure.
13. In wave FEA simulation, the soil medium size is not a significant factor in wave propagation, and its affects on wave propagation are negligible.
14. Perfectly matched layers are an excellent choice for preventing wave reflection from the boundaries of the FEA.
15. A meta-barriers height of 4a, where a is the lattice constant, is ideal for observing a complete bandgap in dynamic response models.

Based on the conclusion above, using 2-layered unit cells with periodicity in two horizontal directions is recommended for maximum protection from surface waves. Moreover, the density of the outer layer of a unit cell (Matrix) is recommended to have low density, such as rubber, carbon fiber reinforced polymer, or concrete, which are considered common construction materials, and a high inner layer (core) material such as steel. Additionally, the unit cells are recommended to be embedded in soil with the periodic arrangement in the horizontal directions such that the unit cells are spaced as follows 0-x-y-x-0 m, where x is 0.125a, y is 0.25a, and a is the size of the unit cell (lattice constant). Moreover, the embedded unit cells are recommended to form an equiangular triangle shape in the vertical direction to reduce the seismic wave reflection and to increase the wave direction diversion.

5.3. Suggested Future Development

Seismic metamaterials are the new category of seismic protection methods. This research established the possibility of widening the metamaterial attenuation zone and maximizing the protection range. Future development of this research is suggested below:

1. Experimental testing of the double-graded configuration to evaluate its capabilities obtained in the numerical analysis.
2. Interactions between different metamaterial layers and with the soil because such regions are assumed to be perfectly bonded, which is not ideal in real-life scenarios.
3. The effect of material nonlinearity is ignored in current study, which needs further investigation.
4. Investigate the effect of soil types on the performance of the proposed meta-barriers

5. Investigate the effect of different earthquake records (near-fault, far-fault) with different frequency content.
6. To investigate the performance of the meta-barrier for different wave sources (from bottom for examples) and at different angles using shake table tests and numerical analyses.
7. In-depth evaluation of the science behind wave blocking of meta-barriers due to periodicity and local resonance at the unit cell level.

REFERENCES

- Achaoui T., Antonakakis S., Brule R., Craster S., Enoch, and Guenneau S. (2017). Clamped seismic metamaterials: ultra-low frequency stop bands. New J. Phys. **19(6)**, 063022.
- Alhan C., Gavin H. P., and Aldemir U. (2006). ptimal control: basis for performance comparison of passive and semiactive isolation systems. J. Eng. Mech. **132(7),** 705-713.
- Bao J., Shi Z. F., and Xiang H. J. (2012).Dynamic response of a structure with periodic foundations. J. of Eng. Mech. **138,** 761-9.
- Braile L., Purude University (2010) URL https://web.ics.purdue.edu/~braile/edumod/waves/WaveDemo.htm.
- Brillouin L. (1930).Les électrons dans les métaux et le classement des ondes de de Broglie correspondantes Comptes Rendus Hebdomadaires des Séances de l'Académie des Sciences. **191**, 292.
- Brule S., Javelaud E. H., Enoch S., and Guenneau S..(2017)Flat lens effect on seismic waves propagation in the subsoil. Scientific Reports **7**, 18066.
- Chang S.-Y., Chen C.-D., Yeh J.-Y., and Chen L.-W.(2019). Elastic wave propagation of two dimensional metamaterials composed of auxetic star-shaped honeycomb structures. Crystals **9**: 121.
- Chen C., Lei J., and Liu Z. (2022). Ternary Seismic Metamaterial for Low Frequency Vibration Attenuation. Mat. **15**: 1246.
- Chen Y., Qian F., Scarpa F., Zuo L., and Zhuang X. (2019). Harnessing multi-layered soil to design seismic metamaterials with ultralow frequency band gaps. Mat. Des. **175**, 107813.

- Cheng Z. B., Shi Z. F., Mo Y. L., and Xiang H. J. (2013). Locally resonant periodic structures with low frequency band gaps. J. Appl. Phys. **114,** 033532.
- Chong K. H., Lee L., “Earthquake seismology I” (2020) URL: https://www.ucl.ac.uk/EarthSci/people/lidunka/GEOL2014/Geophysics4%20%20Seismic%20waves/Seismology/EARTHQUAKE%20SEISMOLOGY%20I.htm.
- Colombi A., Roux P., Guenneau S., Gueguen P., and Craster R. V.. (2016). Forests as a natural seismic metamaterial: Rayleigh wave bandgaps induced by local resonances. Scientific Reports **6**, 19238.
- Colombi A., Guenneau S., Roux P., and Craster R. V. (2016). Transformation seismology: composite soil lenses for steering surface elastic Rayleigh waves. Scientific Reports **6,** 25320.
- Colquitt D. J., Colombi A., Craster R. V., Roux P., and Guenneau S. R. L.. (2017). Seismic metasurface: Sub-wavelength resonators and Rayleigh wave interaction. J. Mech. Phys. Solids **99,** 379-393.
- COMSOL Multiphysics® v. 6.5. www.comsol.com. COMSOL AB, Stockholm, Sweden.
- Daradkeh A. M., Hojat Jalali H., and Seylabi E.. (2022). Mitigation of seismic waves using graded broadband metamaterials. J. Appl. Phys. **132**, 054902.
- Du Q., Zeng Y., Huag G., and Yang H. (2017). Elastic metamaterial-based seismic shield for both Lamb and surface waves. AIP Advances **7**: 075015.
- Du Q., Zeng Y., Xu Y., Yang H., and Zeng Z. (2018). H-fractal seismic metamaterial with broadband low-frequency bandgaps. J. Phys. **51**: 105104.
- Farzam M. F., and Hojat Jalali H. (2022). Tandem tuned mass damper inerter for passive control of buildings under seismic loads. Struct. Conrol Health Monit. **29(9)**: 2987.

- Fiore S., Magisano D., Finocchio G., and Chiappini M. (2021). Metafoundation as a new approach for seismic isolation of buildings. 8th ECCOMAS Thematic Conference, Greece.
- Geng Q., Zhu S., and Chong K. P. (2018). Issues in design of one-dimensional metamaterials for seismic protection. Soil Dynamics and earthquake engineering **107**, 264-278.
- Gomez-Leon A., and Platero G.(2013). Floquet-Bloch Theory and Topology in Periodically Driven Lattices. Phys. Rev. Lett. **110,** 200403.
- Hojat Jalali H., and Farzam M. F. (2022). Inerter-Connected Double Tuned Mass Damper for Passive Control of Buildings under Seismic Excitation. Periodica Polytechnica Civil Eng. **66(2)**: 421–432.
- Huang J., and Shi Z.(2013) Attenuation zones of periodic pile barriers and its application in vibration reduction for plane waves. J. Sound and Vibration **19**, 4423-4439.
- Huang J. K., and Shi Z. F.(2013). Application of periodic theory to rows of piles for horizontal vibration attenuation. Int. J. of Geomech **13**, 132–42.
- Hussein M., and Frazier M.(2010). Band structure of phononic crystals with general damping. J. Appl. Phys. **108**, 093506.
- John S. (1987) Strong localization of photons in certain disordered dielectric superlattices. Phys. Rev. Lett. **58**, 2486.
- Jung H.-J., Spencer B. F., Ni Q. Q., and Lee I. W. (2004). State-of-the-art of semiactive control systems using MR fluid dampers in civil engineering applications. Struc. Eng. and Mech. **17(3-4)**: 493-526.
- Kaveh A., Farzam M. F., and Hojat Jalali H. (2020a). Statistical seismic performance assessment of tuned mass damper inerter. Struct. Conrol Health Monit. **27(10)**: 2602.

- Kaveh A., Farzam M. F., Hojat Jalali H., and Maroofiazar R. (2020b). Robust optimum design of a tuned mass damper inerter. Acta Mechanica **231**: 3871-3896.
- Khelif A., Achaoui Y., Benchabane S., Laude V., and Aoubiza B. (2010). Locally resonant surface acoustic wave band gaps in a two-dimensional phononic crystal of pillars on a surface. Phys. Rev. B **81**, 214303.
- Kittel C. (2005).Introduction to Solid State. Physics 8th ed.
- Li T., Su Q., and Kaewunruen S. (2020). Seismic metamaterial barriers for ground vibration mitigation in railways considering the train-track-soil dynamic interactions. Construction and Building Materials **260**: 119936.
- Liu X., Wang Y., and Chen Y. (2019). Attenuation zones of two-dimensional periodic foundations including the effect of vertical loads. App. Sci. **9**, 993.
- Liu Y., Chen Y., Li J., Hung T.-C., and Li J. (2012). Study of energy absorption on solar cell using metamaterials. Solar Energy **86(5)**: 1586-1599.
- Madelung O. (1995).Introduction to Solid-State Theory. Springer.
- Maheshwari H. K., and Rajagopal P. (2022). Novel locally resonant and widely scalable seismic metamaterials for broadband mitigation of disturbances in the very low frequency range of 0-33 Hz. Soil Dyn. Earthquake Eng. **161**, 107409.
- Marchi L. D., Marzani A., and Miniaci M. (2013). A dispersion compensation procedure to extend pulse-echo defects location to irregular waveguides. NDT&E Int. **54**, 115–122.
- Martincek G. (1995). Dynamics of Pavement Structures. Taylor & Francis Group.
- Mei J., Liu Z., Shi J., and Tian D. (2003). Theory for elastic wave scattering by a two-dimensional periodical array of cylinders: An ideal approach for band-structure calculations. Phys. Rev. B **67**, 245107.

- Miniaci M., Krushynska A., Bosia F., and Pugno N. M. (2016). Large scale mechanical metamaterials as seismic shields. New J. Phys., **18(8),** 083041.
- Miniaci M., Kherraz N., Croenne C., Mazzotti M., Morvaridi M., Gliozzi A. S., Onorato M., Bosia F., and Pugno N. M. (2021). Hierarchical large-scale elastic metamaterials for passive wave mitigation. Appl. Metamat. **8**, 14.
- Moser F., Jacobs L. J., and Qu J. (1999). Modeling elastic wave propagation in waveguides with the finite element method. NDT&E Int. **32**, 225–234.
- Mu D., Shu H., Zhao L., An S. (2020). A Review of Research on Seismic Metamaterials. Advanced Engineering Materials **22,** 1901148.
- Muhammad, Lim C. W., and Zur K. K. (2021). Wide Rayleigh waves bandgap engineered metabarriers for ground born vibration attenuation. Eng. Struc. **246**, 113019.
- Palermo A., Vitali M., and Marzani A. (2018). Metabarriers with multi-mass locally resonating units for broadband Rayleigh waves attenuation. Soil Dynamics and Earthquake Eng. **113**, 265-277.
- Paz M., and Leigh W. (2004). Structural Dynamics: Theory and Computation. 5th ed. New York, Springer.
- PEER. Peer Ground Motion Database http://peer.berkeley.edu/peer_ground_motion_database 2012.
- Pourzeynali S., Salimi S., Yousefisefat M., and Kalesar H. E. (2016). Robust multi-objective optimization of STMD device to mitigate buildings vibrations. Earthquake and Structures **11(2)**:347-369.
- Rodger M. W., Metamaterials: What are they? What are they good for? APS March Meeting Abstract 200. p. 5001.

- Sevil O., WorldVision.org (2023) URL https://www.worldvision.org/disaster-relief-news-stories/2023-turkey-and-syria-earthquake-faqs.
- Shahoei H., and Yao J. (2012). Continuously Tunable Microwave Frequency Multiplication by Optically Pumping Linearly Chirped Fiber Bragg Gratings in an Unbalanced Temporal Pulse Shaping System. J. Lightwave Tech. **30**, 12.
- Shi Z., and Huang J. (2013). Feasibility of reducing three-dimensional wave energy by introducing periodic foundation. Soil Dyn. Earthq. Eng. **50**, 204-212.
- Smith D. R., Vier D. C., Kroll N., and Shcultz S. (2000) Direct calculation of permeability and permittivity for a left-handed metamaterials. Appl. Phys. Lett **77,** 2246.
- Sukhovich A., Merheb B., Muralidharan K., Vasseur J. O., Pennec Y., Deymier P. A., and Page J. H. (2009). Experimental and Theoretical Evidence for Subwavelength Imaging in Phononic Crystals" Phys. Rev. Lett. **102**, 154301.
- U.S. Geological Survey, "Earthquake Hazards" (2021) URL https://www.usgs.gov/natural-hazards/earthquake-hazards/science/cool-earthquake-facts?qt-science_center_objects=0#qt-science_center_objects.
- Verma A., Gupta A., and Nath B. (2017). Base Isolation System: A Review. Int. J. Eng. Sci. Inv. **6(9)**, 2319-6726.
- Xiang H. J., Shi Z., Wang S. J., Mo Y. L. (2012). Periodic Materials-based vibration attenuation in layered foundations: experimental validation. Smart Mat. Struc. **21**, 112-003.Xiong C., Shi Z., and Xiang H. J. (2012). Attenuation of building vibration using periodic foundations. Adv. Struc. Eng. **15**, 1375-88.

- Xu X., Barnhart M. V., Li X., Chen Y., and Huang G. (2019). Tailoring vibration suppression bands with hierarchical metamaterials containing local resonators. J. Sound and Vib. **442**: 237-248.
- Yan Y., Cheng Z., Menq F., Mo, Tang Y., Shi Z. F. (2015). Three dimensional periodic foundations for base seismic isolation. Smart Mater Struct **24,** 075006.
- Yan Y., Laskar A., Cheng Z., Menq F., Tang Y., Mo Y. L., and Shi Z. F. (2014). Seismic isolation of two dimensional periodic foundations. J. Appl. Phys. **116,** 044908.
- Yang F., Kong D., and Kong L. (2018). Accurate measurement of high-frequency dynamic blast waves through compensation of miniature piezoelectric pressure sensors. Sensors and Actuators A **280**, 14-23.
- Zhang K., Ge M., Zhao C., Deng Z., and Xu X. (2019). Free vibration of nonlocal Timoshenko beams made of functionally graded materials by Symplectic method. Comp. Part B: Eng. **156**, 174-184.
- Zhang K., Luo J., Hong F., and Deng Z. (2021). Seismic metamaterials with cross-like and square steel sections for low-frequency wide band gaps. Eng. Struc. **232**, 111870.
- Zhao H., Liu Y., Yu D., Wang G., Wen J., and Wen X. (2007). Absorptive properties of three-dimensional phononic crystal. J. Sound and vibration **303**, 158-194.

APPENDIX A. DISPERSION RELATIONS OF THE INVESTIGATED UNIT CELLS FOR GEOMETRY PARAMETRIC STUDY

This appendix presents all the results of the investigated unit cell geometry that were not included in section 4.1.1.

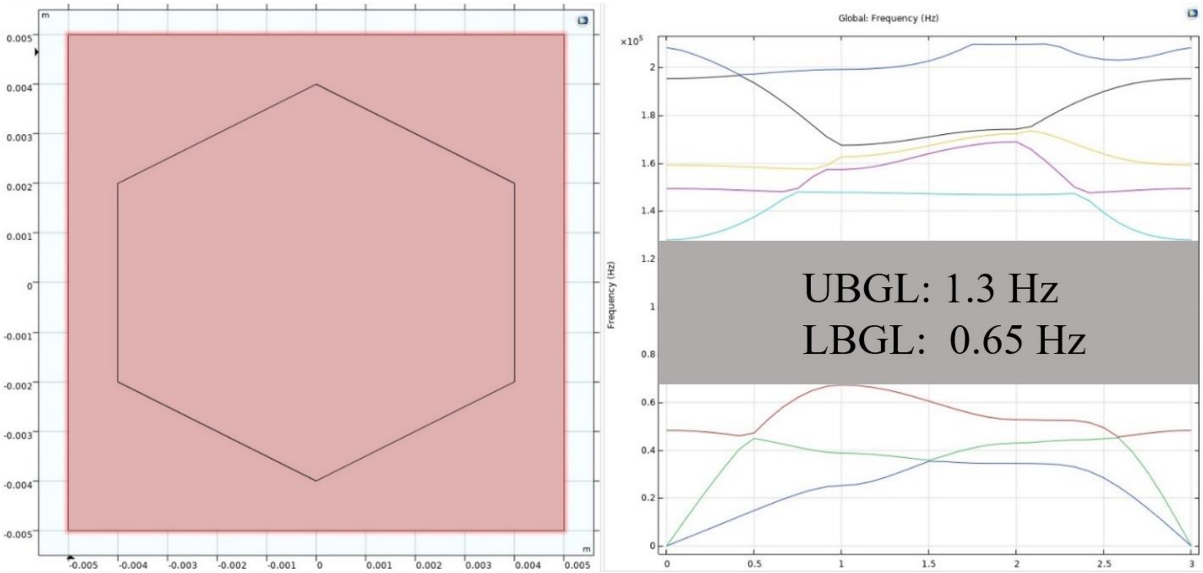

Figure A- 1: Square concrete matrix (1 m) and hexagon rubber core.

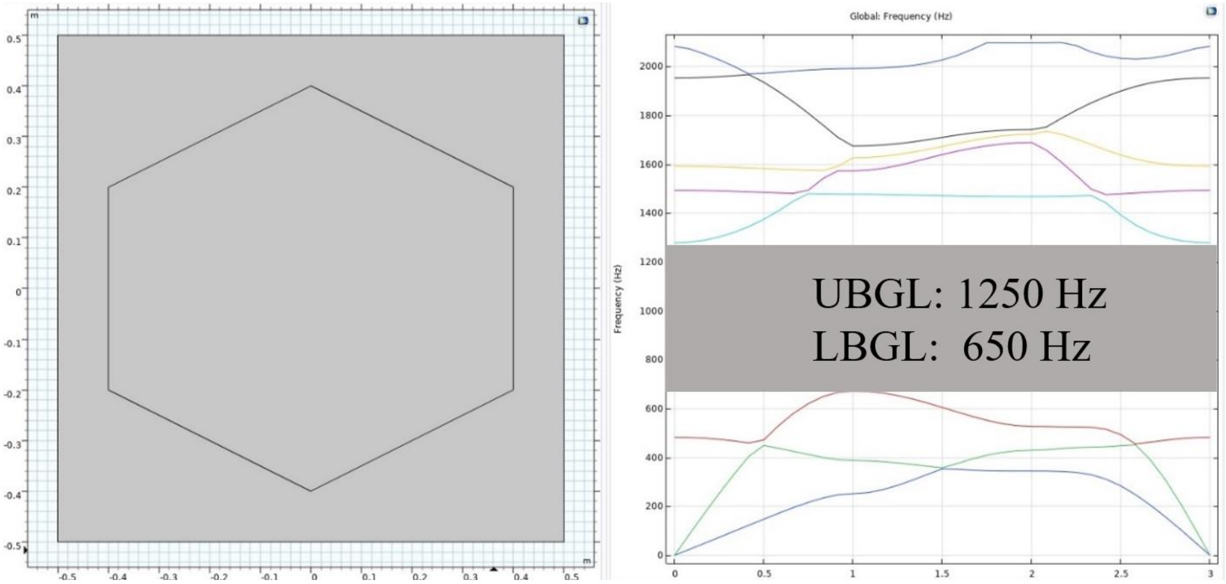

Figure A- 2: Square concrete matrix (1 cm) and hexagon rubber core.

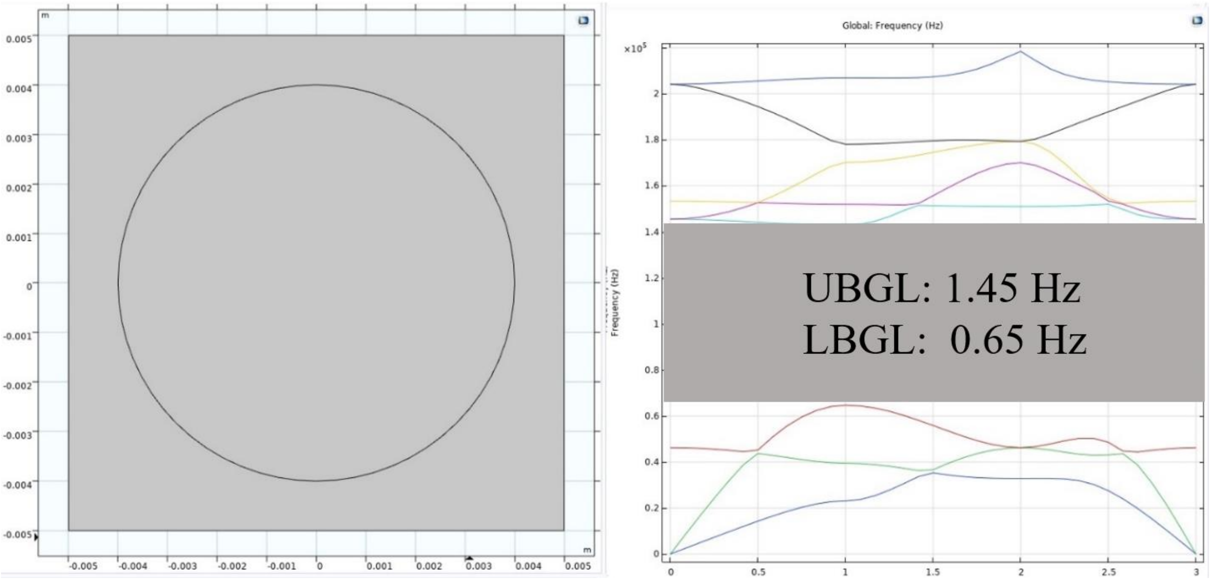

Figure A- 3: Square concrete matrix (1 cm) and circular rubber core.

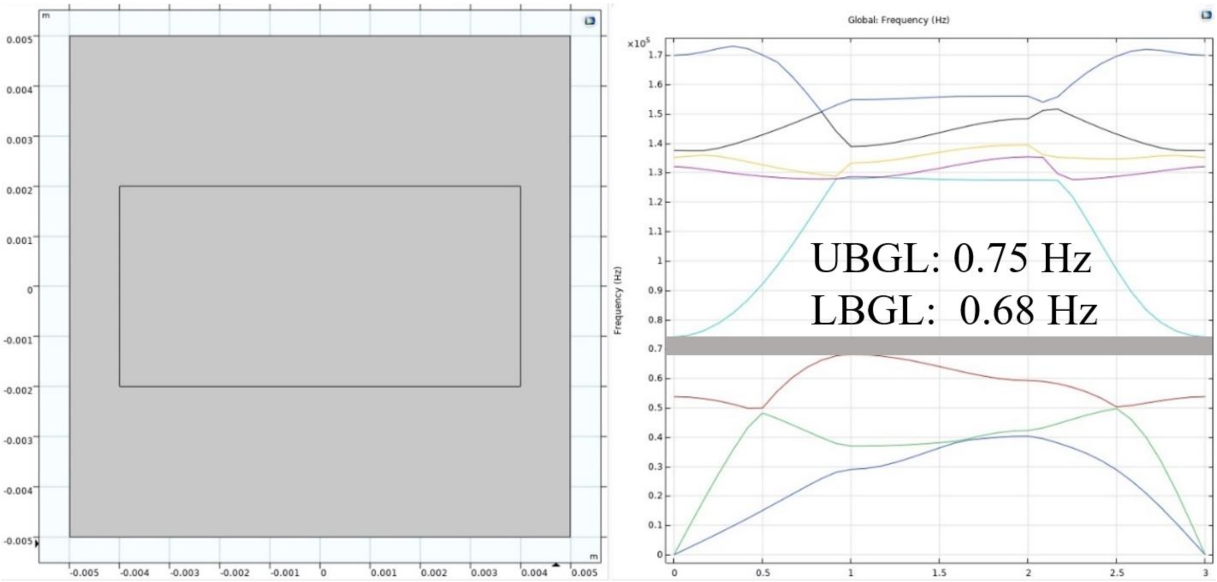

Figure A- 4: Square concrete matrix (1 cm) and rectangular rubber core (0.8x0.4 cm).

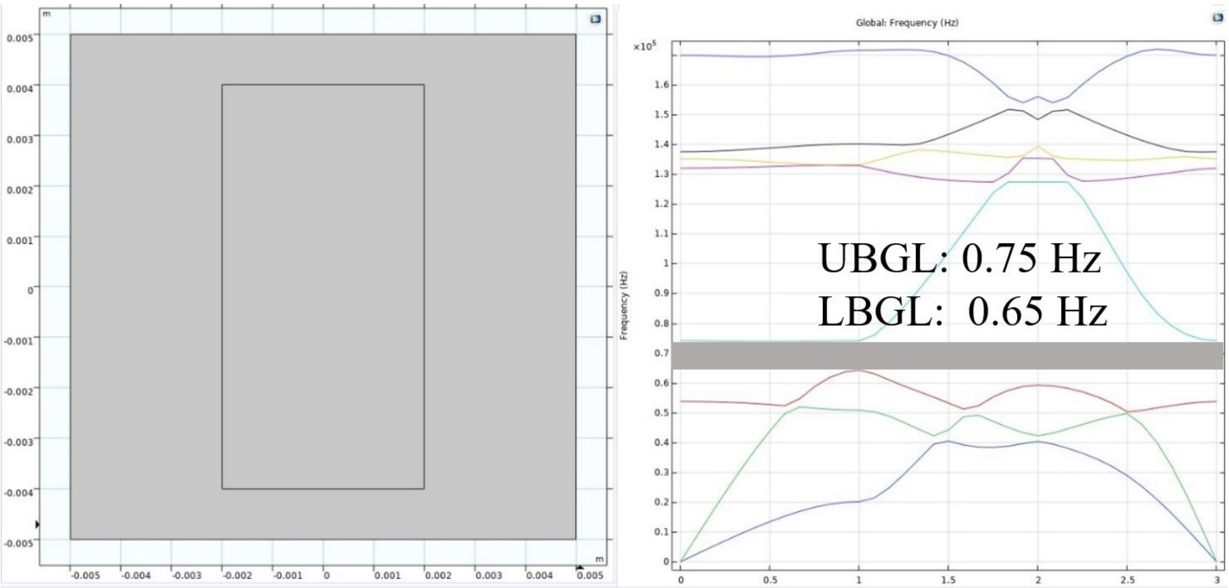

Figure A- 5: Square concrete matrix (1 cm) and rectangular rubber core (0.4x0.8 cm).

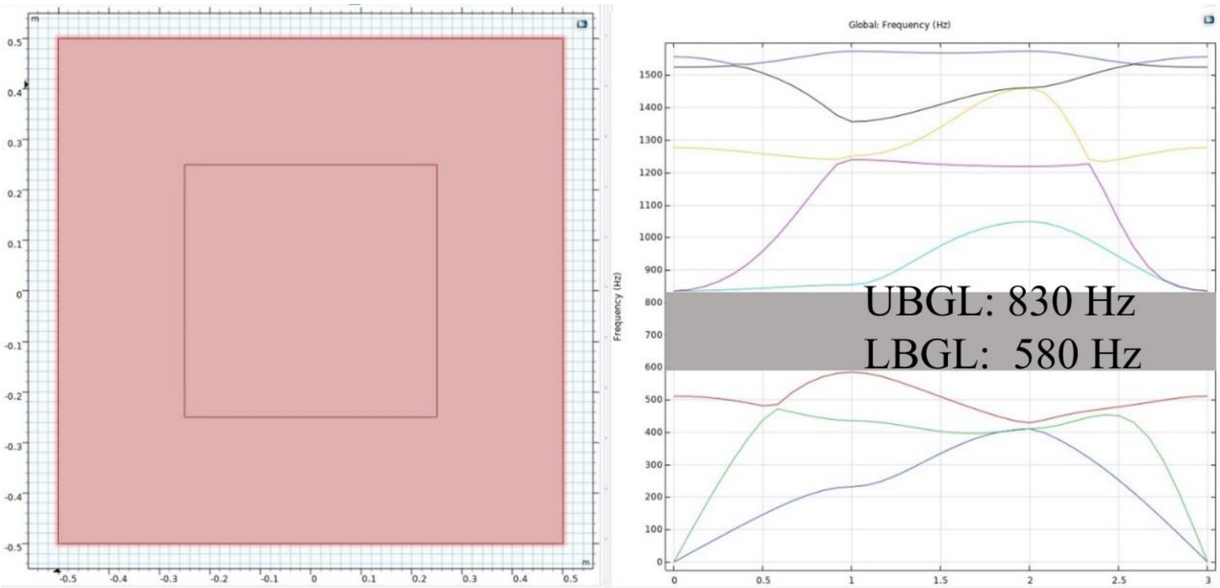

Figure A- 6: Square concrete matrix (1 m) and square rubber core (0.5 m).

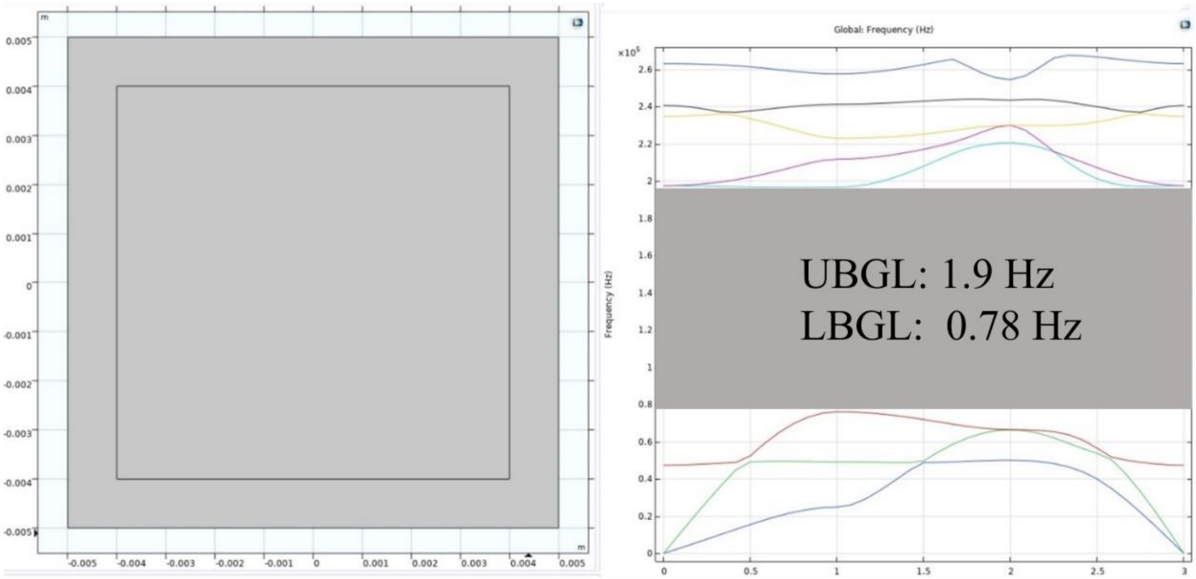

Figure A- 7: Square concrete matrix (1 m) and square rubber core (0.8 m).

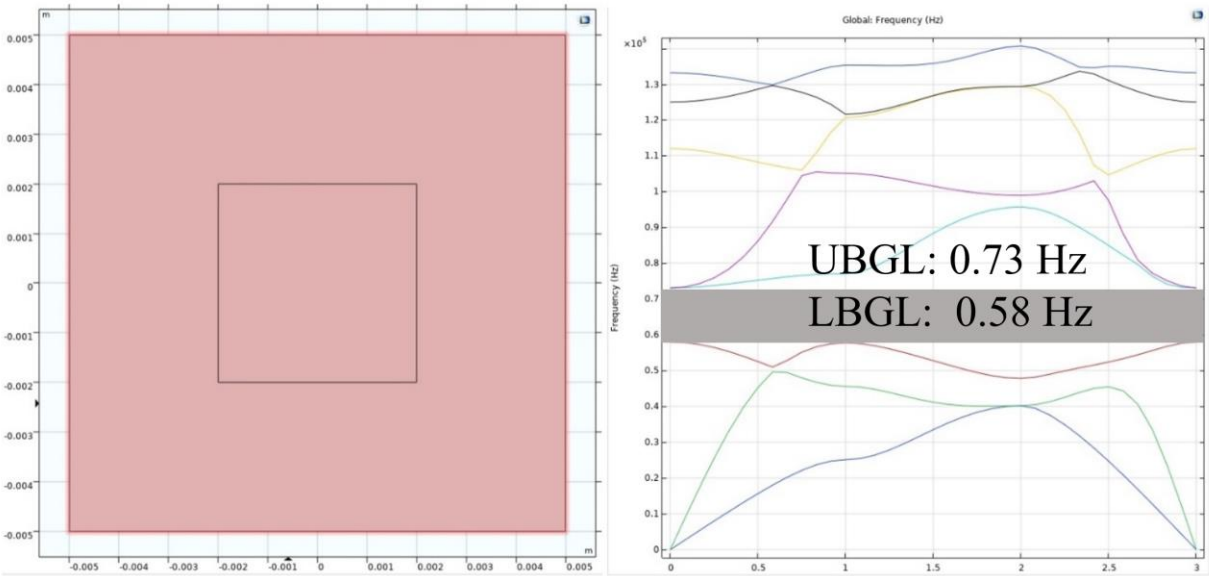

Figure A- 8: Square concrete matrix (1 cm) and square rubber core (0.5 cm).

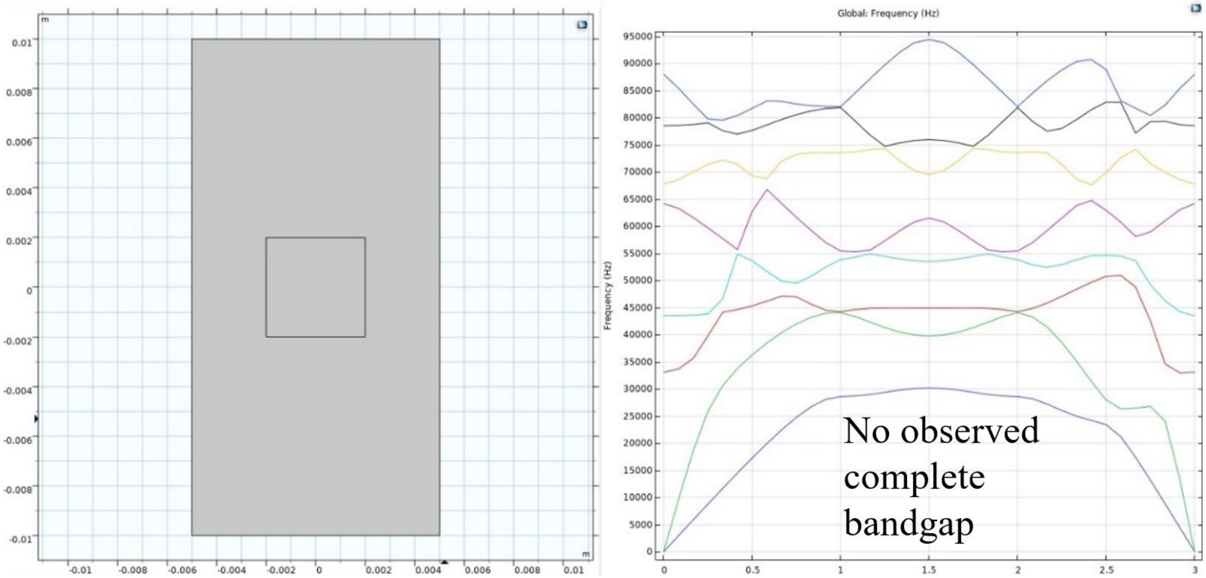
Global: Frequency (Hz)

No observed complete bandgap

Figure A- 9: Rectangular concrete matrix (1x10 cm) and square rubber core (0.1 cm).

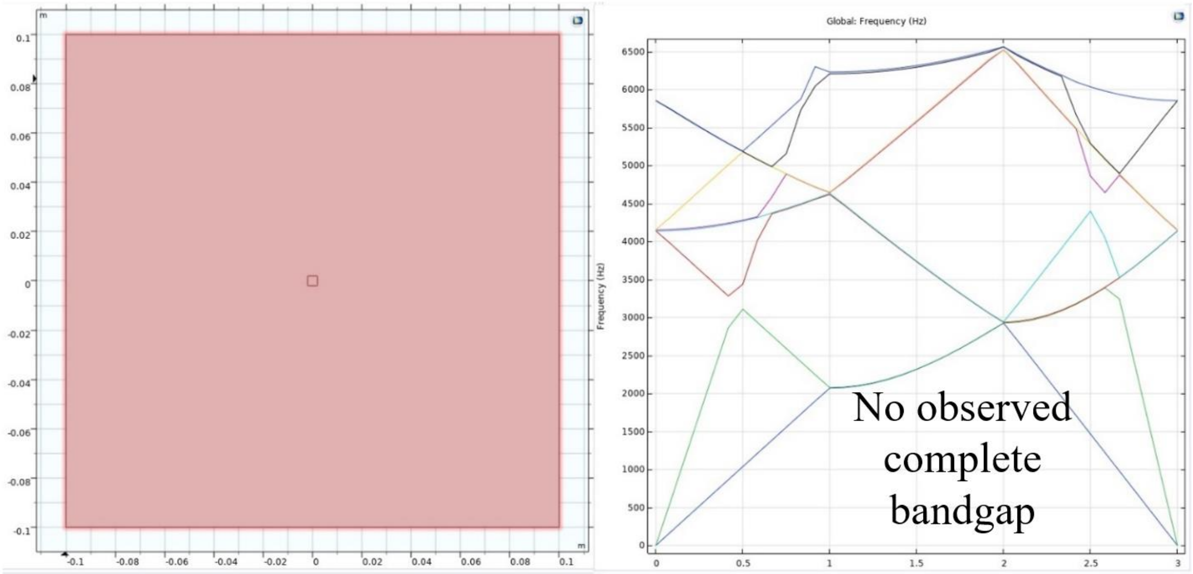
Global: Frequency (Hz)

No observed complete bandgap

Figure A- 10: Square concrete matrix (0.2 m) and square rubber core (0.01 m).

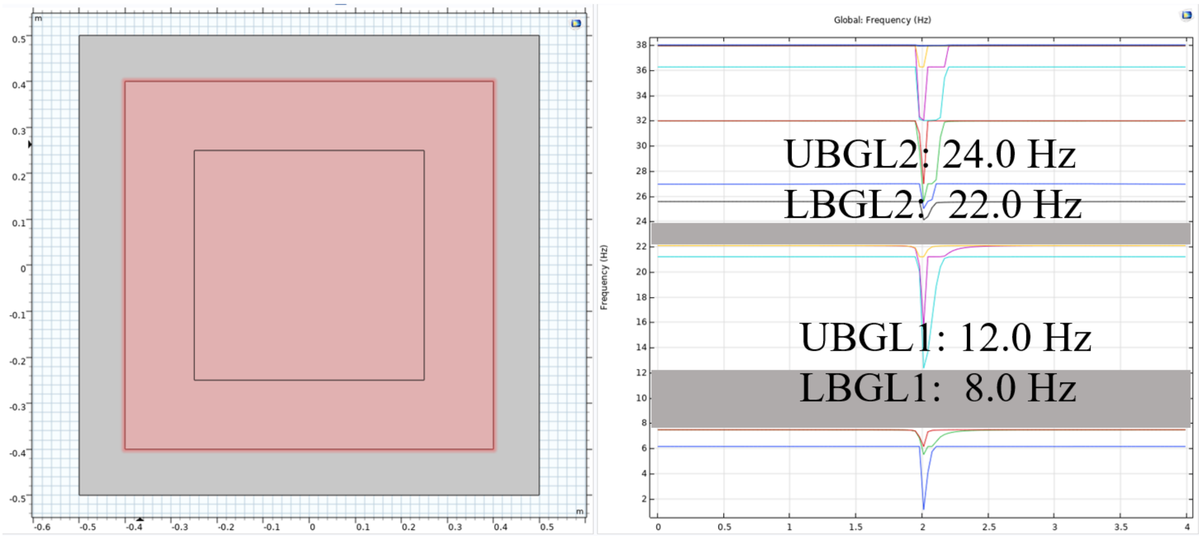

Figure A- 11: Square concrete matrix (1 m), square rubber coating (0.8 m), and square steel core (0.4 m).

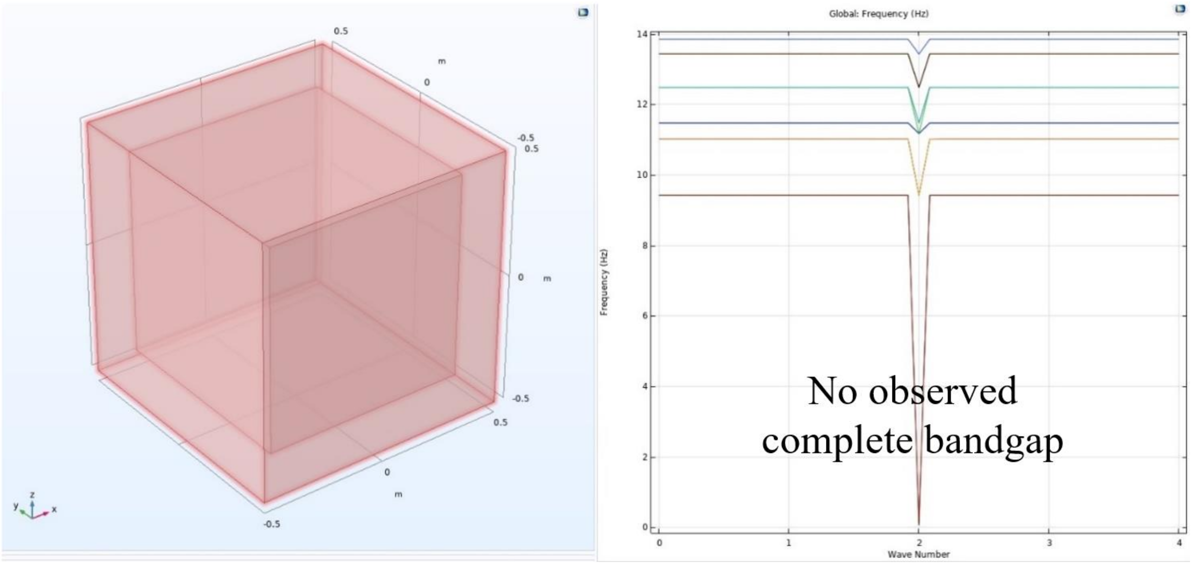

Figure A- 12: Cubical concrete matrix (1 m) and cubical rubber core (0.8 m).

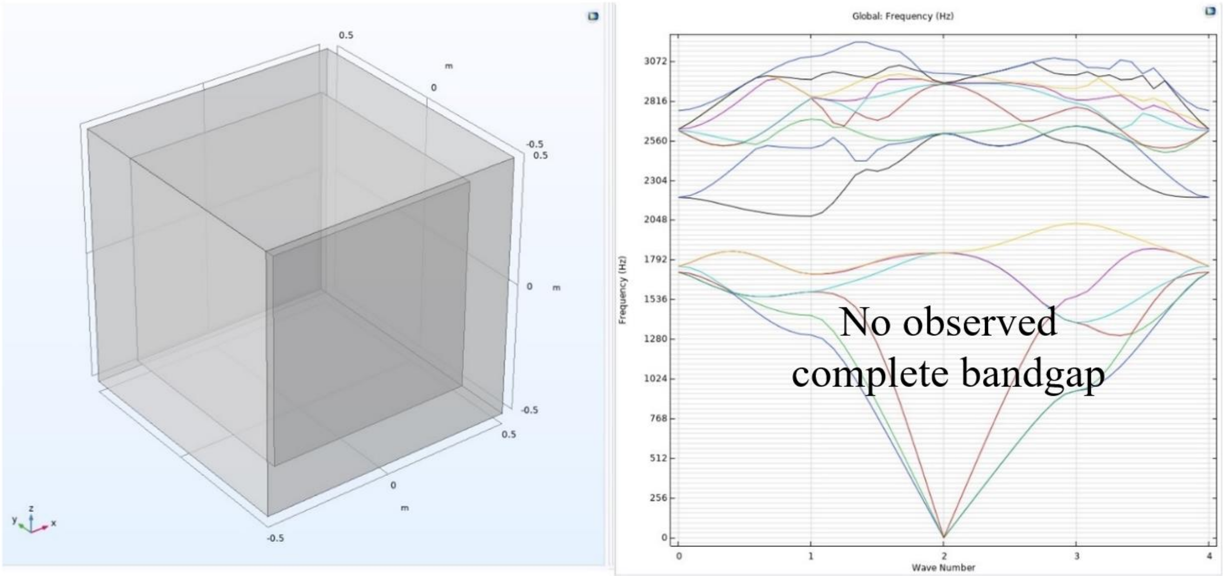

No observed complete bandgap

Figure A- 13: Cubical concrete matrix (1 m) and cubical steel core (0.8 m).

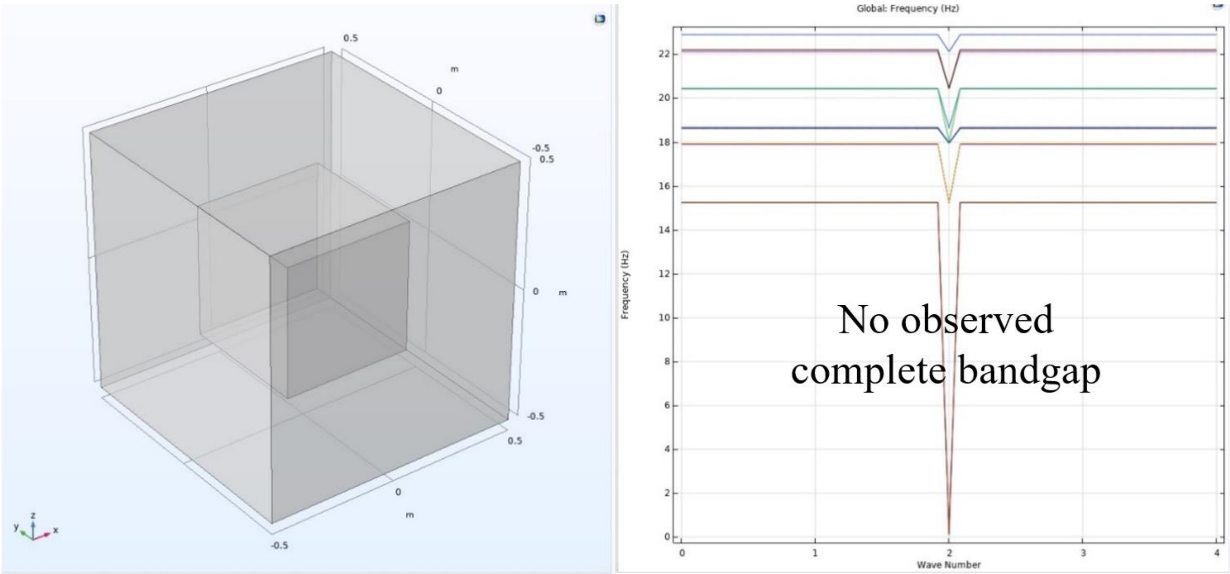

No observed complete bandgap

Figure A- 14: Cubical concrete cube matrix (1 m) and cubical rubber core (0.4 m).

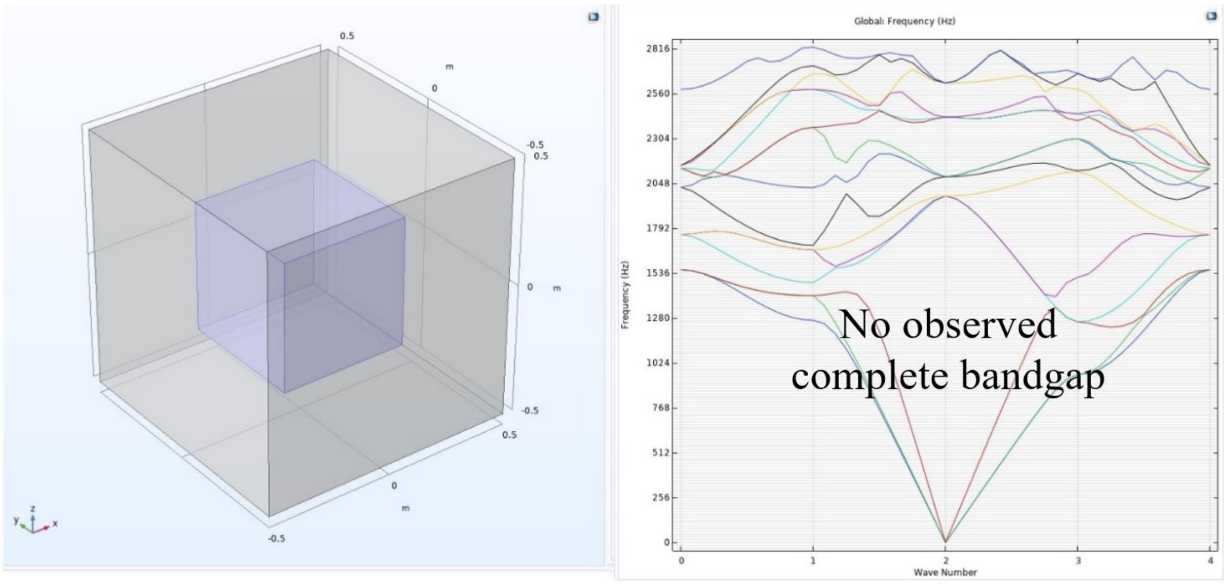

Figure A- 15: Cubical concrete matrix (1 m) and cubical steel core (0.4 m).

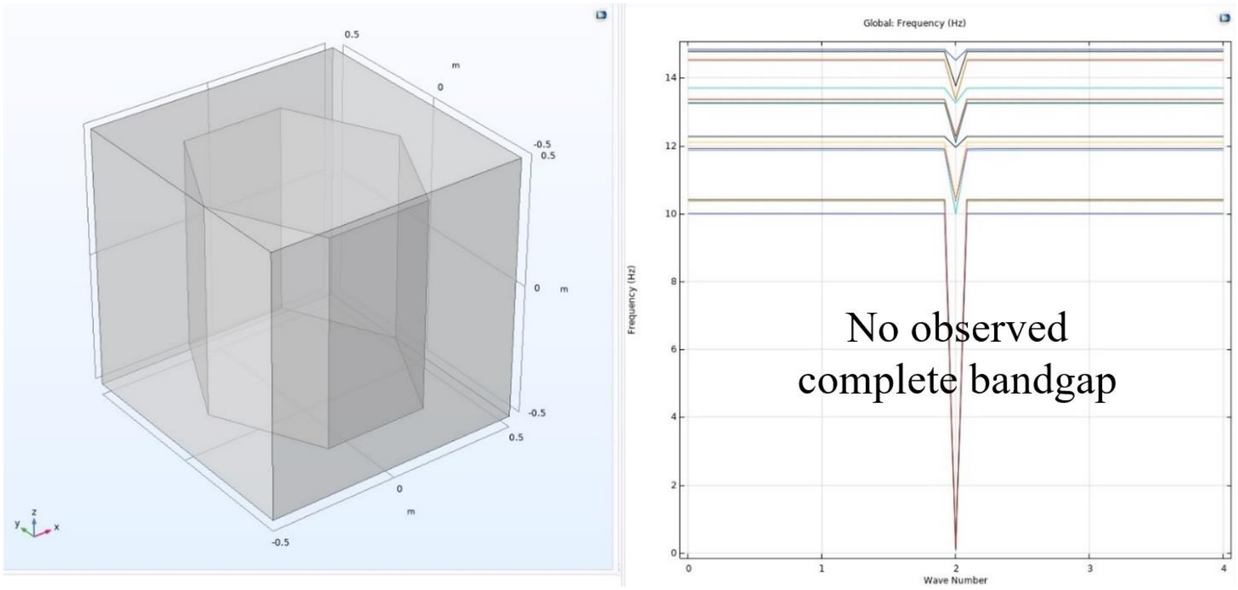

Figure A- 16: Cubical concrete matrix (1 m) and hexagonal rubber core.

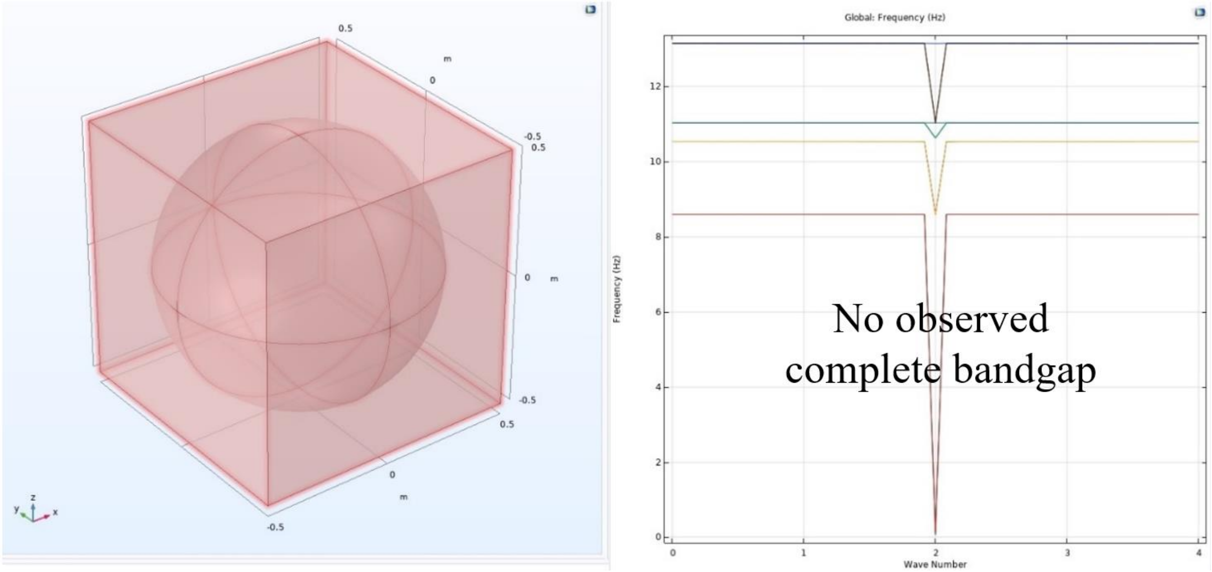

No observed complete bandgap

Figure A- 17: Cubical concrete matrix (1 m) and spherical rubber core.

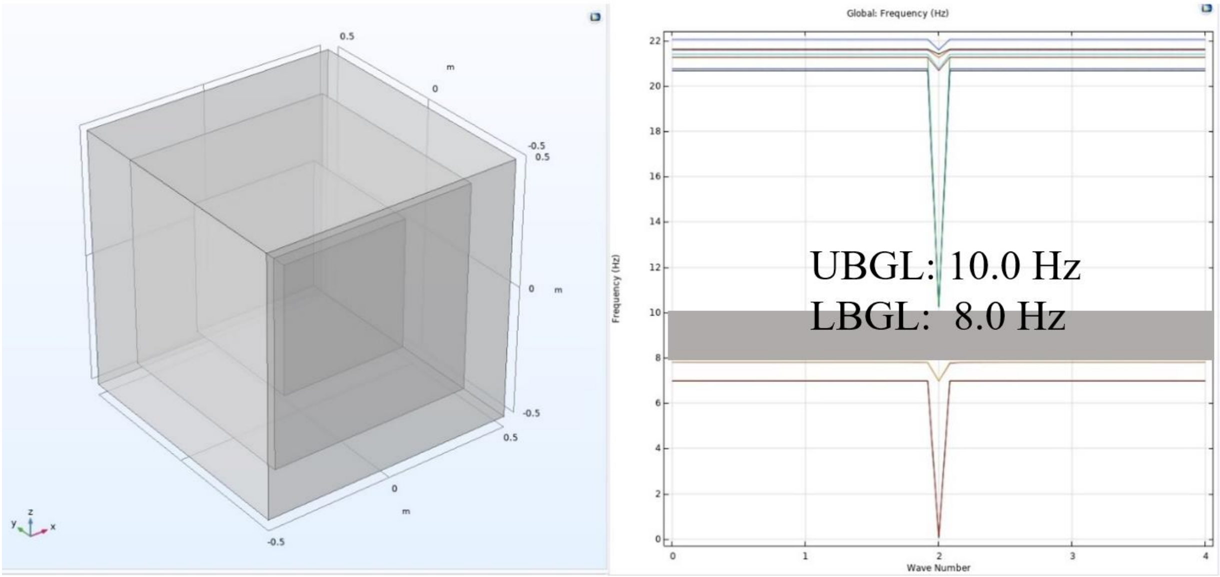

UBGL: 10.0 Hz
LBGL: 8.0 Hz

Figure A- 18: Cubical concrete matrix (1 m), cubical rubber coating (0.8 m), and cubical steel core (0.4 m).

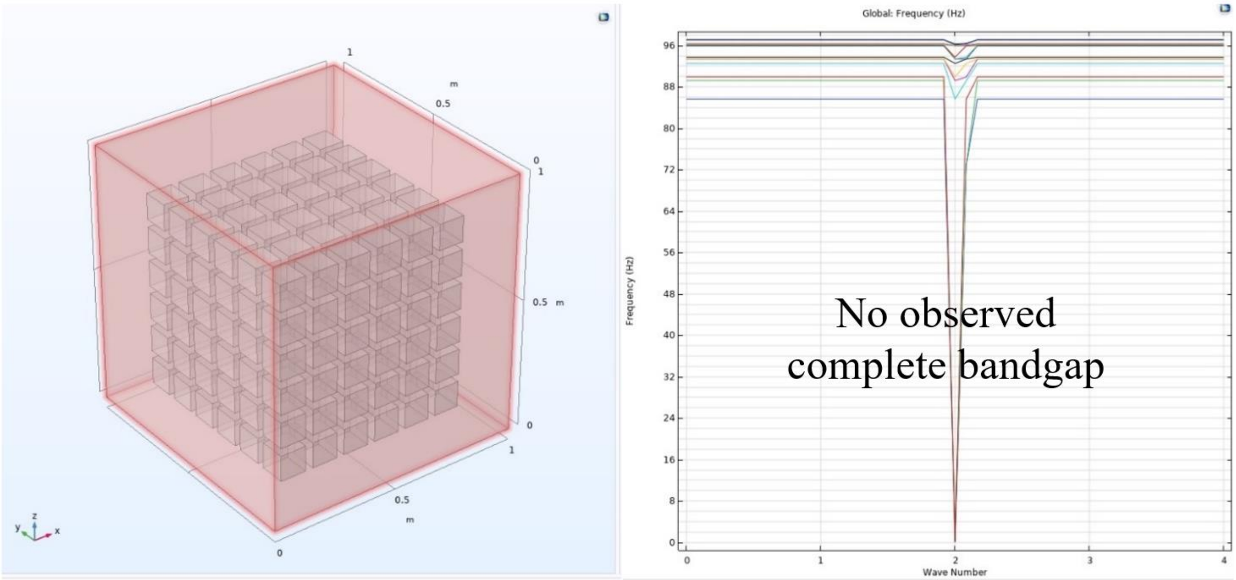

Figure A- 19: Cubical Concrete matrix (1 m) and cubical rubber array (0.01 m each).

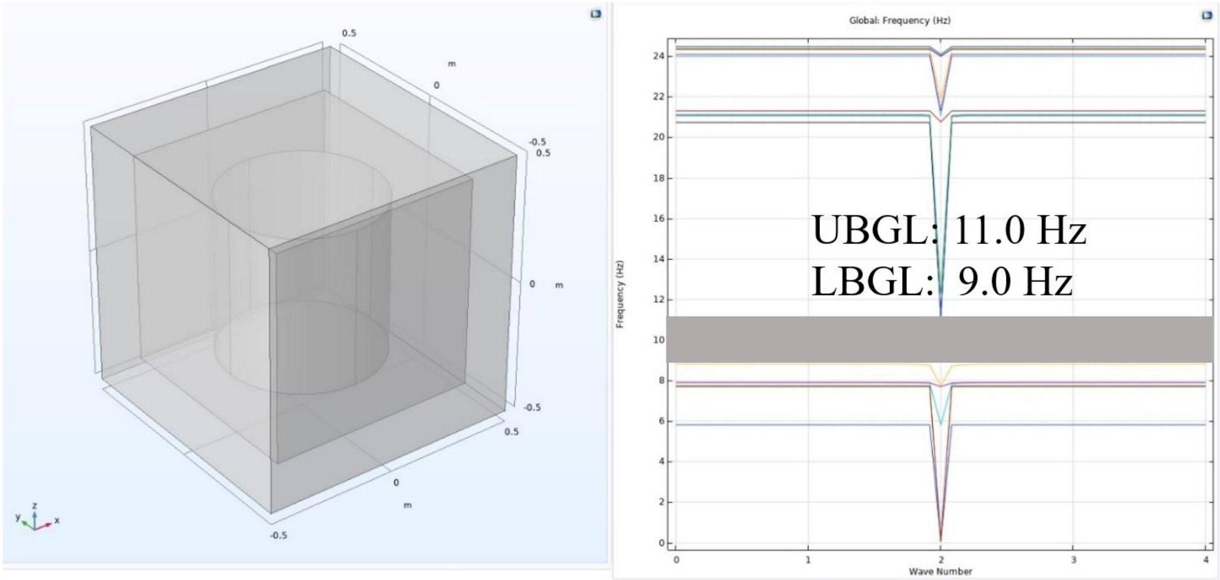

Figure A- 20: Cubical concrete matrix (1 m), cubical rubber coating (0.8 m), and cylindrical steel core.

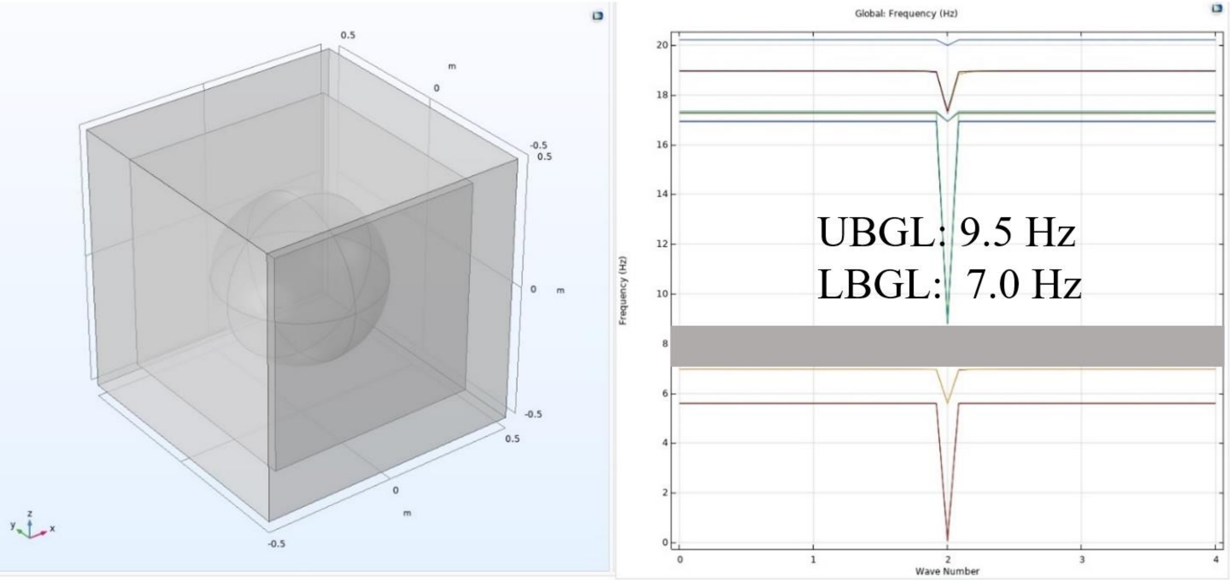

Figure A- 21: Cubical Concrete matrix (1 m), cubical rubber coating (0.8 m), and spherical steel core.

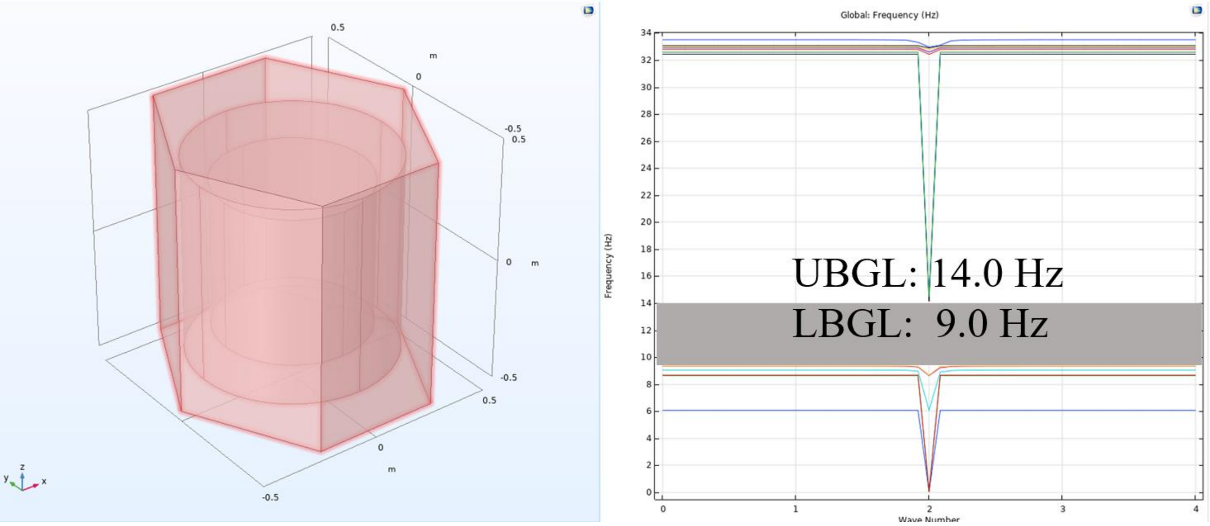

Figure A- 22: Hexagonal concrete core, cylindrical rubber coating, and cylindrical steel core.

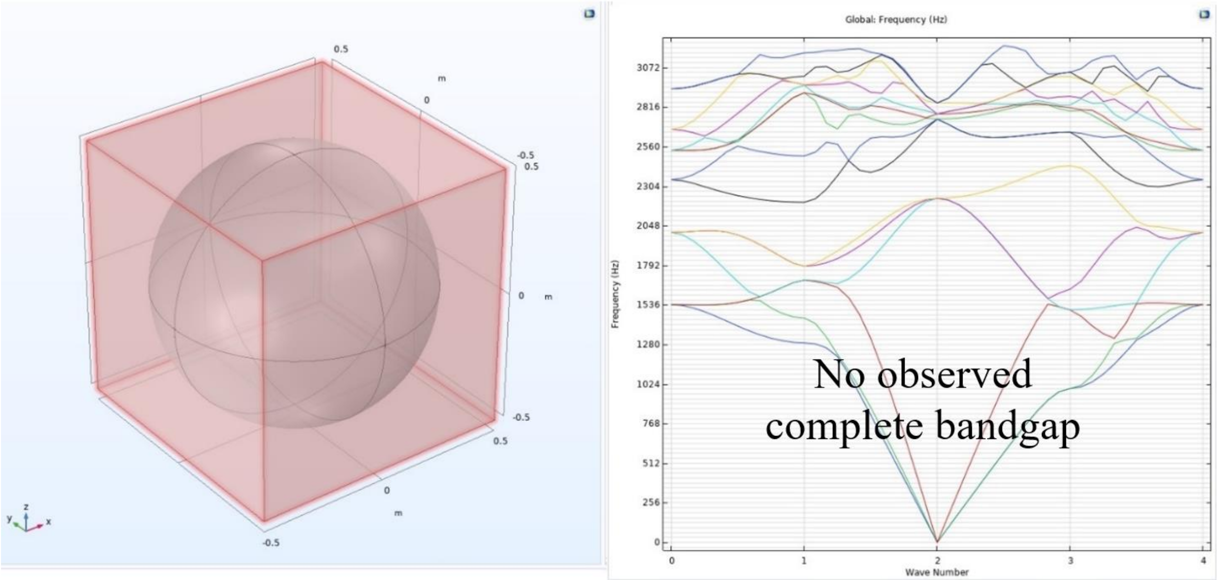

Figure A- 23: Cubical concrete matrix (1 m) and spherical steel core.

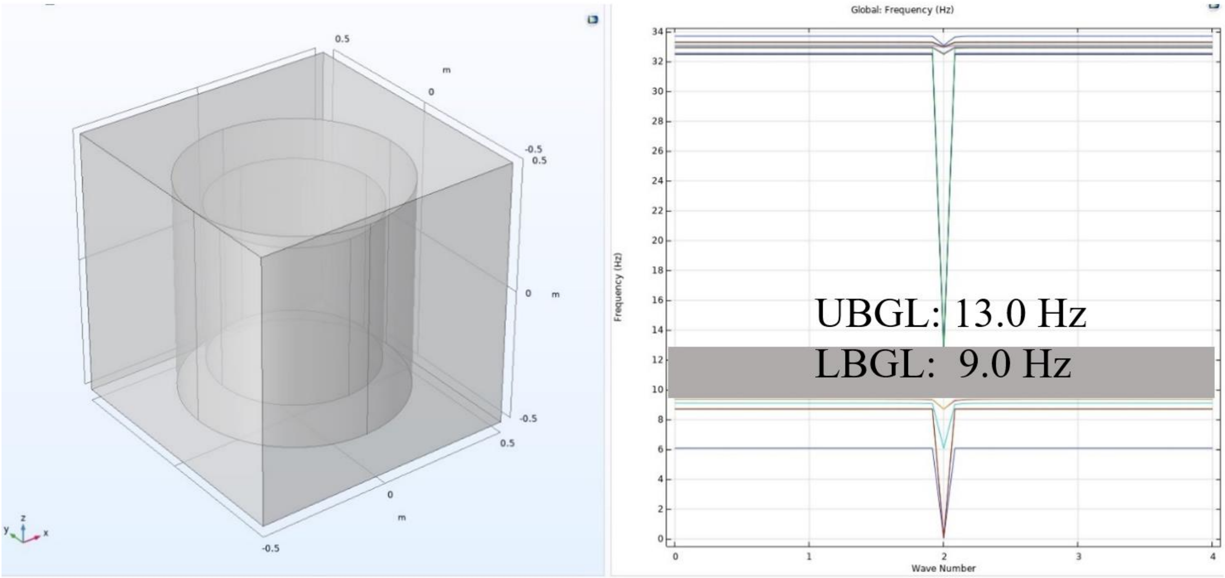

Figure A- 24: Cubical concrete matrix (1 m), cylindrical rubber coating, and cylindrical steel core.

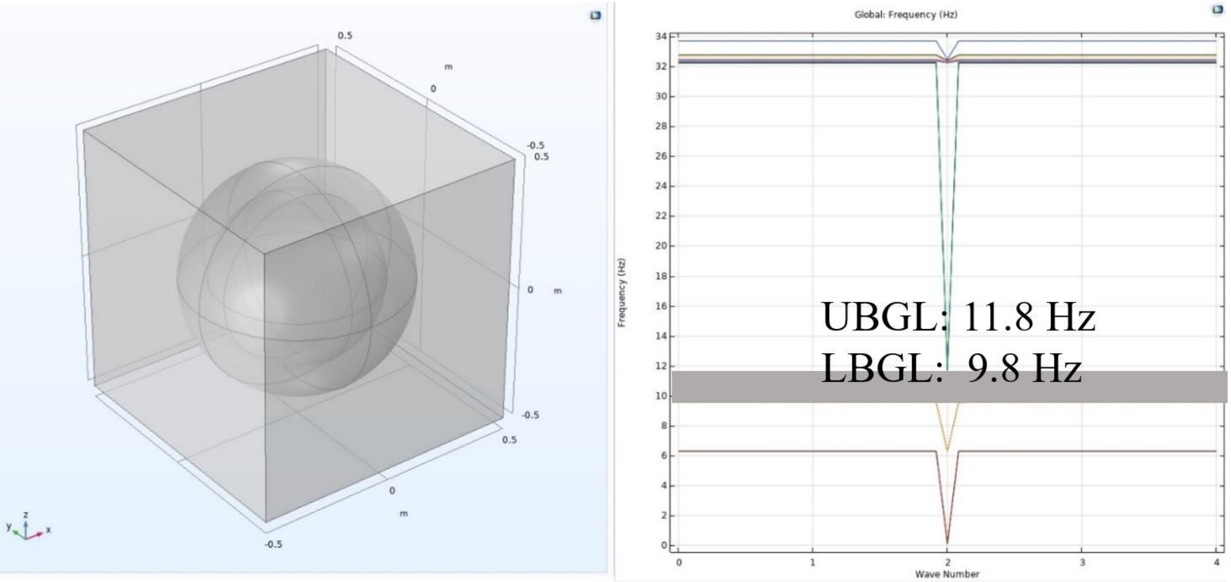

UBGL: 11.8 Hz
LBGL: 9.8 Hz

Figure A- 25: Cubical concrete core (1 m), spherical rubber coating, and spherical steel core.

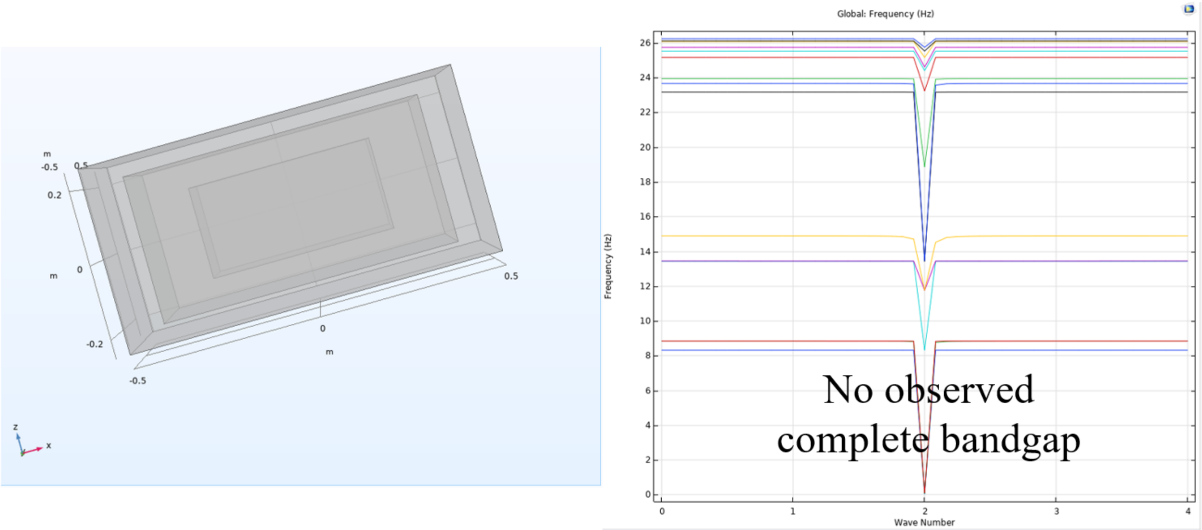

No observed
complete bandgap

Figure A- 26: Cuboid Concrete matrix, cuboid rubber coating, and cuboid steel core.

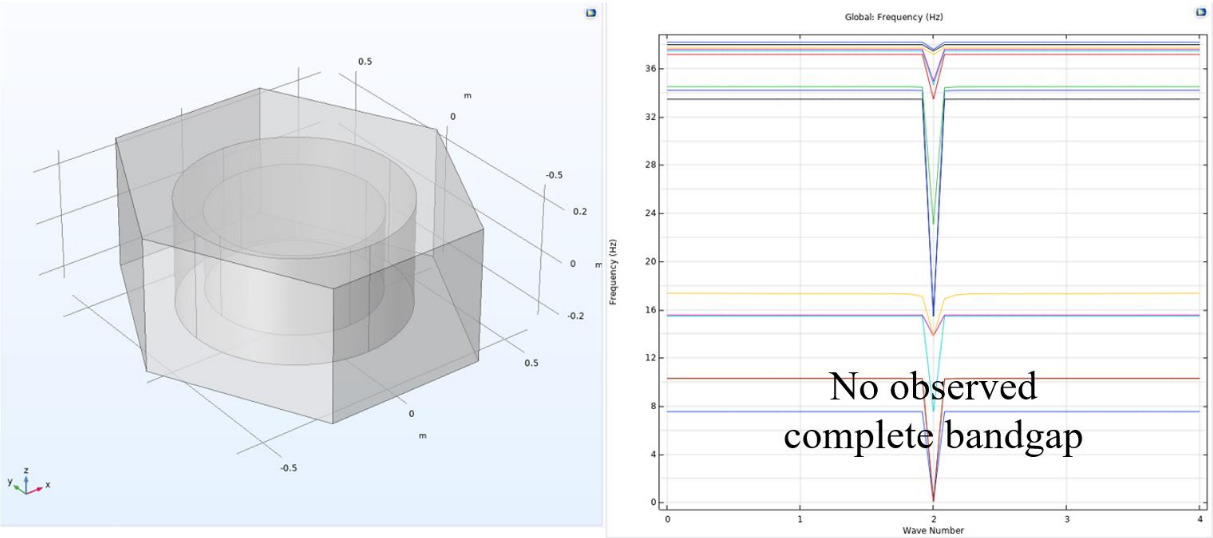

No observed complete bandgap

Figure A- 27: Hexagonal Concrete matrix, cylindrical rubber coating, and cylindrical steel core.

APPENDIX B. SUPPLEMENTAL PARAMETRIC STUDIES

This section presents additional parametric studies to cover the efficiencies of FEA different parameters, such as the required number of unit cells to achieve bandgap, the size of the soil medium, and the performance of the perfectly matched layers in preventing unnecessary wave reflection.

B.1. Minimum Number of Unit Cells in the Vertical Direction to Achieve Protection

As discussed in section 3.2. the unit cell is assumed to be periodically arranged (infinitely repeated) in one or more directions. However, such an assumption is unrealistic as the number of unit cells will be bound to the structure's surrounding area. Section 3.4. unit cell configuration will be embedded in the soil, and the selected unit cell has two-periodicity directions (X and Y). Those periodicity directions are achieved by arranging the unit cells back-to-back and applying periodic boundary conditions along the Y-axis of the model.

Moreover, the unit cells are stacked vertically to prevent the waves from traveling underneath the meta-barriers and to achieve the intended bandgap. This parametric study investigates the minimum number of unit cells required to prevent waves from traveling underneath the metabarriers. To this end, the FEA model, as shown in Figure 3-14, was used with different unit cell numbers (one to 16 rows) in the vertical direction (Rows).

Figure B-1 shows the transmission curve for 1, 4, and 8 rows of unit cells. The result shows that the configuration blocked the waves within the bandgap even with one row of stacked unit cells. However, the transmission increased with the number of unit cells decreased, and this was due to the waves traveling below the unit cells. Moreover, there was a slight difference between 4 and 8 stacked rows in terms of transmission.

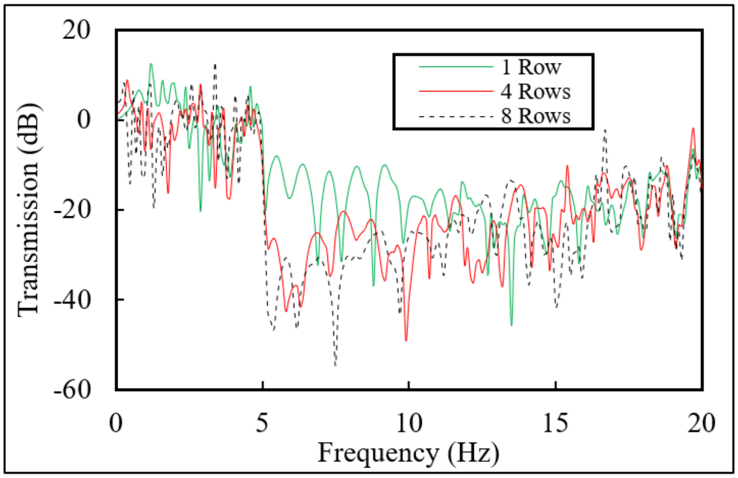

Figure B- 1: Transmission curve for unit cells with 1, 4, and 8 stacked rows of unit cells.

Figure B-2 shows the displacement after the unit cells, where a similar conclusion can be obtained. However, the observed displacement was higher when using four rows compared to 8 rows.

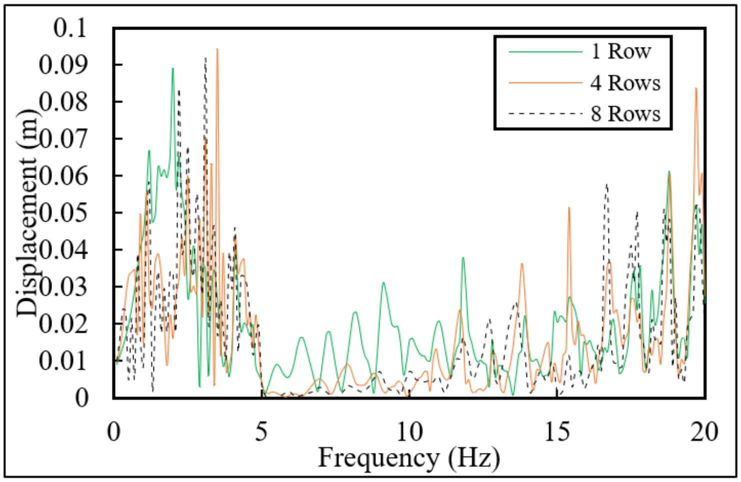

Figure B- 2: Displacement curve after the unit cells for unit cells with 1, 4, and 8 stacked rows of unit cells.

Figure B-3 shows the transmission comparison between 8, 12, and 16 stacked unit cells. The results show that transmission was the lowest with 16 rows (Unit cells are in contact with the bottom boundary of the soil medium). However, the transmission variance between using 8 and 16 rows was insignificant and nearly the same for 8, 12, and 16 rows of unit cells.

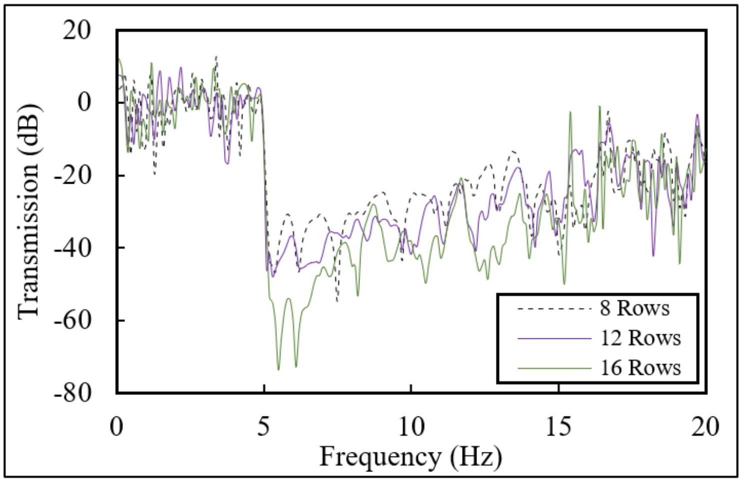

Figure B- 3: Transmission curve for unit cells with 8, 12, and 16 stacked rows of unit cells.

Finally, Figure B-4 shows the displacement after the unit cells, with a similar conclusion to Figure B-3. The displacement is nearly identical for eight or more rows of unit cells. Therefore, it is recommended to use eight rows of stacked unit cells to achieve the intended bandgap and reduce the FEA cost since adding additional rows (Beyond 8) did not add significant value to the transmission or the displacement. On the contrary, adding more rows of unit cells led to doubling the number of elements and therefore increase computational costs of the analysis.

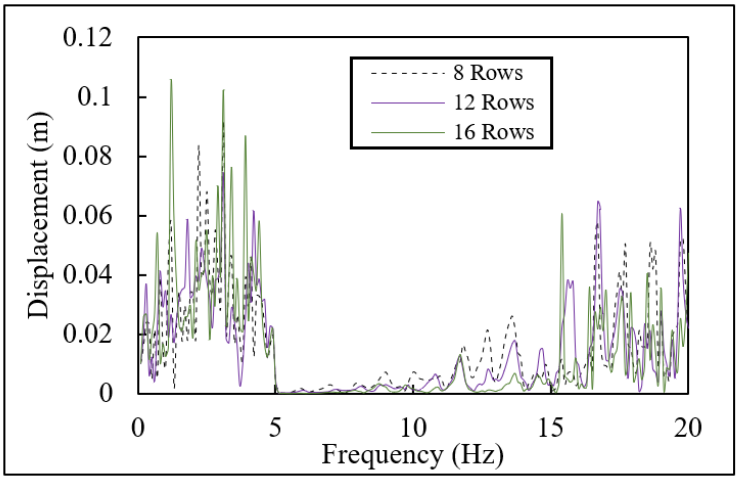

Figure B- 4: Displacement curve after the unit cells for unit cells with 8, 12, and 16 stacked rows of unit cells.

B.2. Effects of Soil Medium Length on Wave Propagation

This section is intended to optimize the wave propagation FEA by studying the effects of the homogenous soil on wave amplitude in the propagation direction. To this end, Figure B-5 shows the developed model for this study, where an SDOF structure was placed in a soil medium, and LRB was applied to the boundary of the soil medium. Moreover, the distance between the wave source and the SDOF (35a in Figure B-5) is investigated while maintaining the same model height. The selected sizes are 25a, 50a, 75a, 100a, 200a, 400a, and 700a, where a is unit cell lattice constant. The displacement at the top of the SDOF is recorded, and only one of the comparisons is shown in this section, while the remaining are shown in Figures B-11 to B-25 of this dissertation. Figure B-6 shows the displacement at the top of the SDOF when the distance between the wave source and the structure is 50a against 400a. The result shows that all soil sizes will yield the same displacement pattern and peak amplitudes at the same peak resonance frequency with negligible variations in amplitudes. This variation is due to the wavelength of the frequency. For instance, at a frequency of 1 Hz, the wavelength (λ) is 64.5 m. Therefore, to obtain the peak amplitude at 1 Hz, the SDOF must be placed precisely at 64.5 m away from the source or exactly at $\lambda/2$. Hence, the wave amplitude varies by the location of the SDOF from the wave source. Therefore, the investigated sizes of the soil do not play a significant role in frequency domain wave propagation analysis in this study.

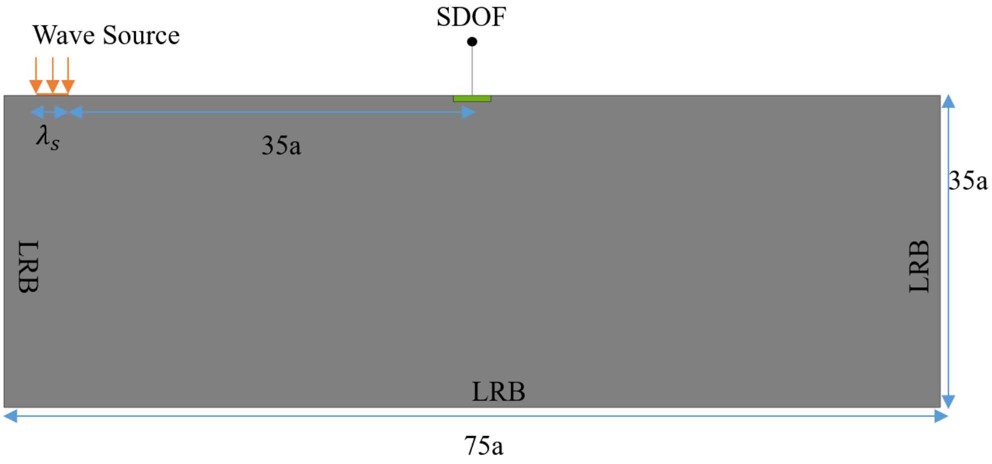

Figure B- 5: Size of homogenous soil to optimize wave propagation FEA.

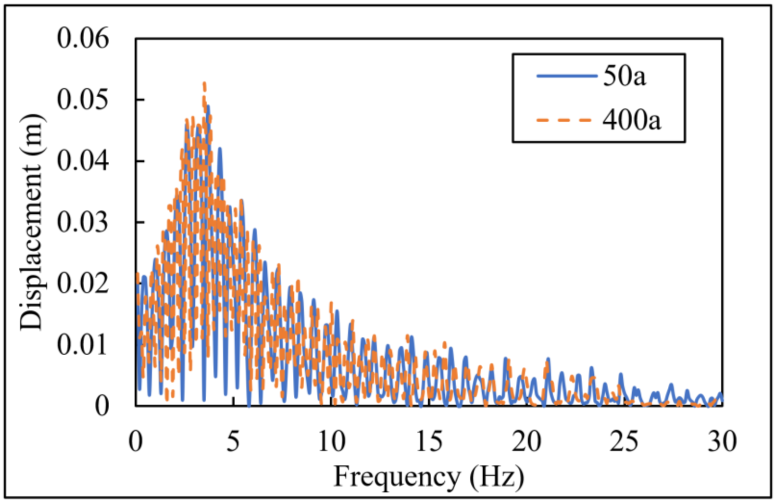

Figure B- 6: Displacement magnitude at the top of SDOF structure comparison between soil size of 50a versus 400a.

B.3. Evaluation of Perfectly Matched Layers in Absorbing All Incoming Waves

This study aims to confirm that the perfectly matched layers (PML) can absorb all incoming waves without unnecessary reflections from the medium boundaries. To this end, the results of the double-graded array, as shown in Figure B-7, were used to plot the displacement along the top line of the soil medium.

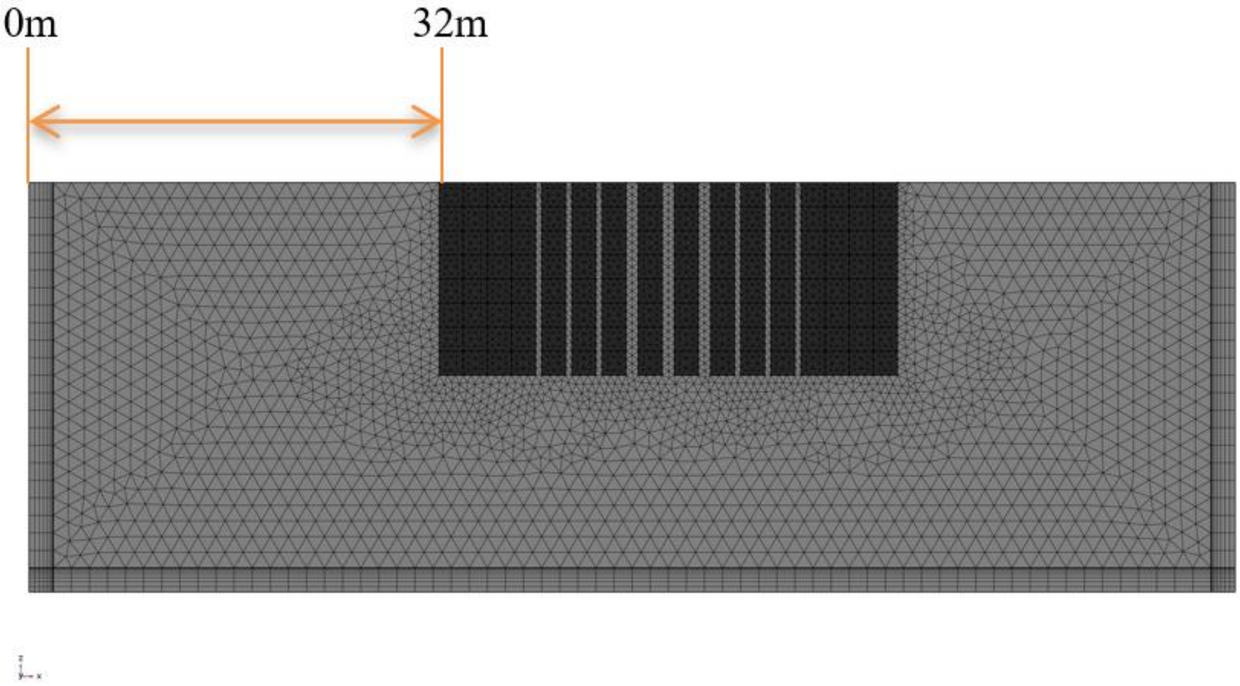

Figure B- 7: The FEM model to obtain PML capabilities.

The displacement along a line from 0 m (edge of the model) and up to 32 m (immediately before the unit cells) was recorded and the results for different frequencies are shown in Figures B-8, B-9, and B-10 for frequencies of 0.1 Hz, 8.7 Hz, and 22.8 Hz respectively. The Figures show that once the wave leaves the source point and enters the PML (marked in grey shaded area), it immediately starts decaying until it reaches 0 amplitude. Moreover, the PML can be seen absorbing all the incoming frequencies (Ultra-low 0.1 Hz or high frequency 22.8 Hz) without reflecting anything to the soil medium. It is worth mentioning that the PML stretching factor used in this research was constant in all the simulations and equal to the longest wavelength (at 0.1 Hz, wavelength = 700 m), and the physical width is 1 m.

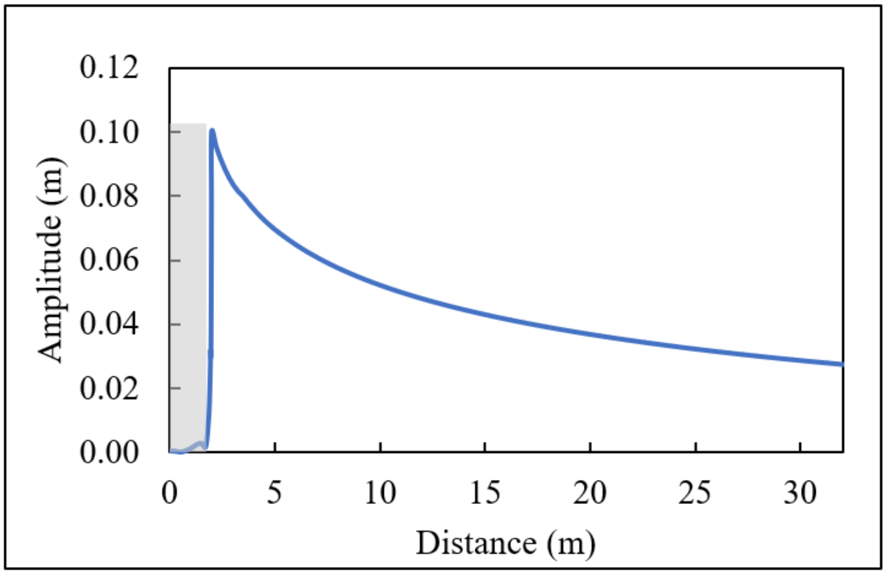

Figure B- 8: Displacement amplitude at a line along the surface of the soil medium for 0.1 Hz.

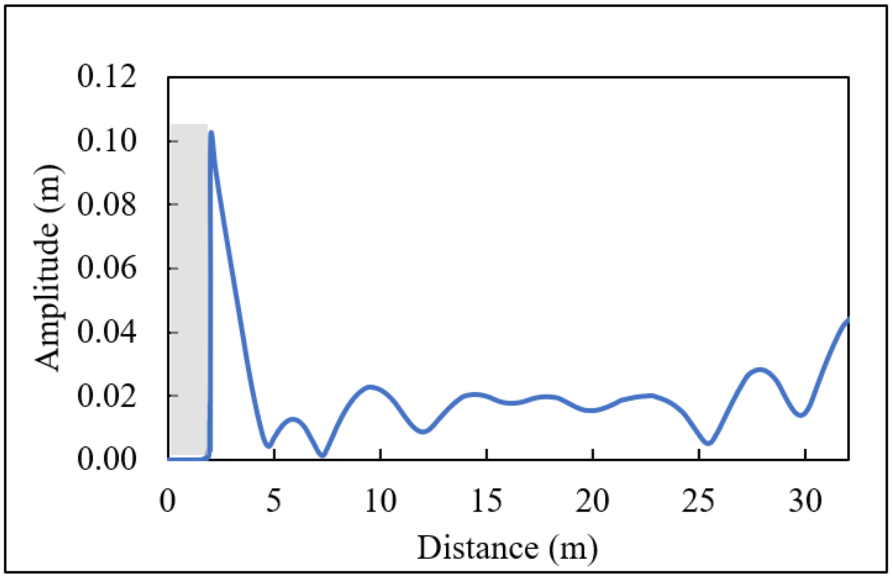

Figure B- 9: Displacement amplitude at a line along the surface of the soil medium for 8.7 Hz.

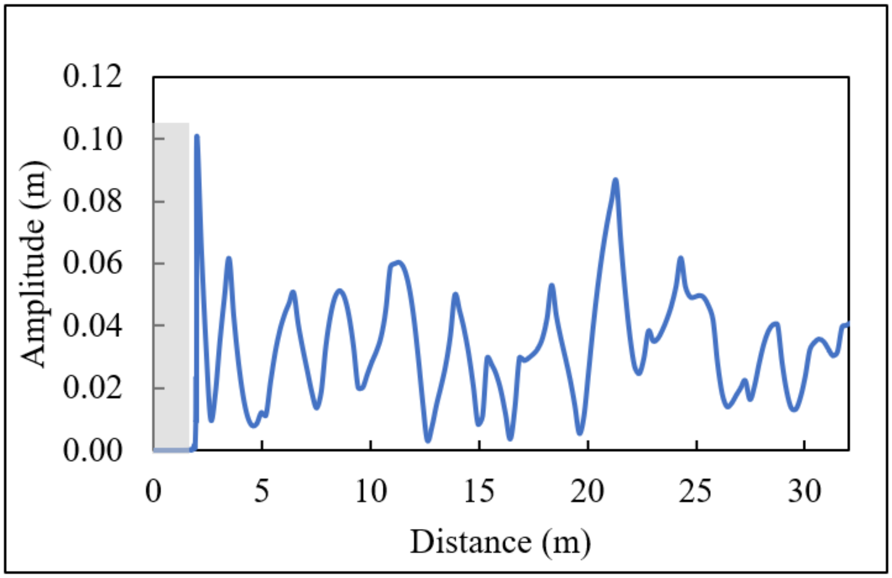

Figure B- 10: Displacement amplitude at a line along the surface of the soil medium for 22.8 Hz.

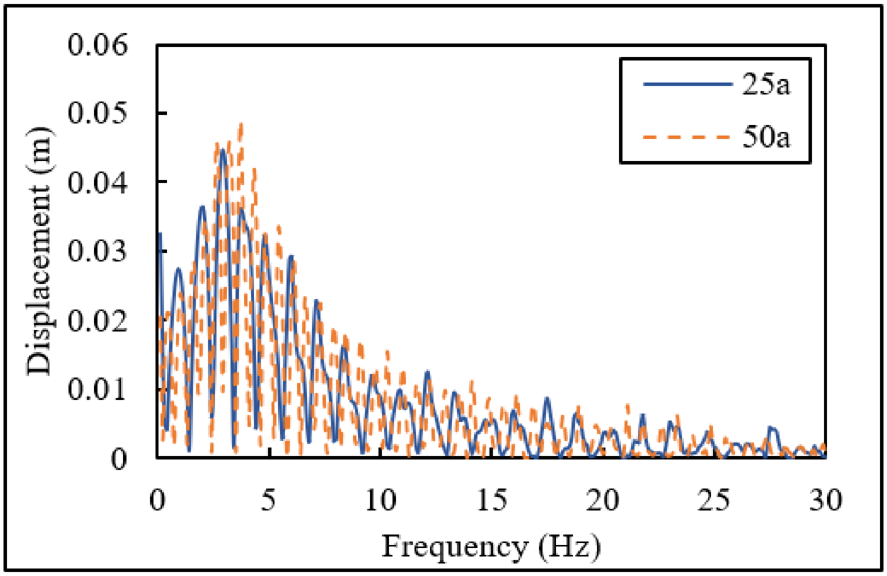

Figure B- 11: Displacement magnitude at the top of SDOF structure comparison between soil size of 25a versus 50a.

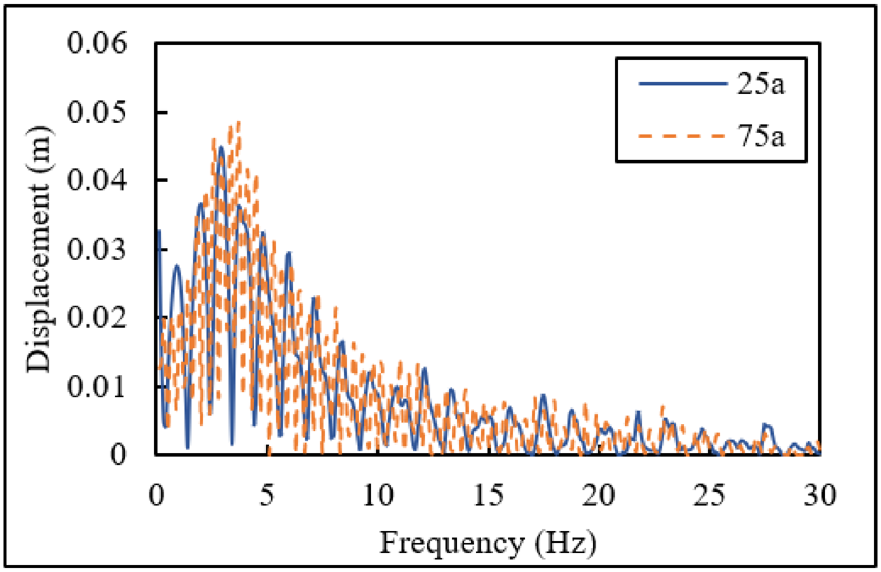

Figure B- 12: Displacement magnitude at the top of SDOF structure comparison between soil size of 25a versus 75a.

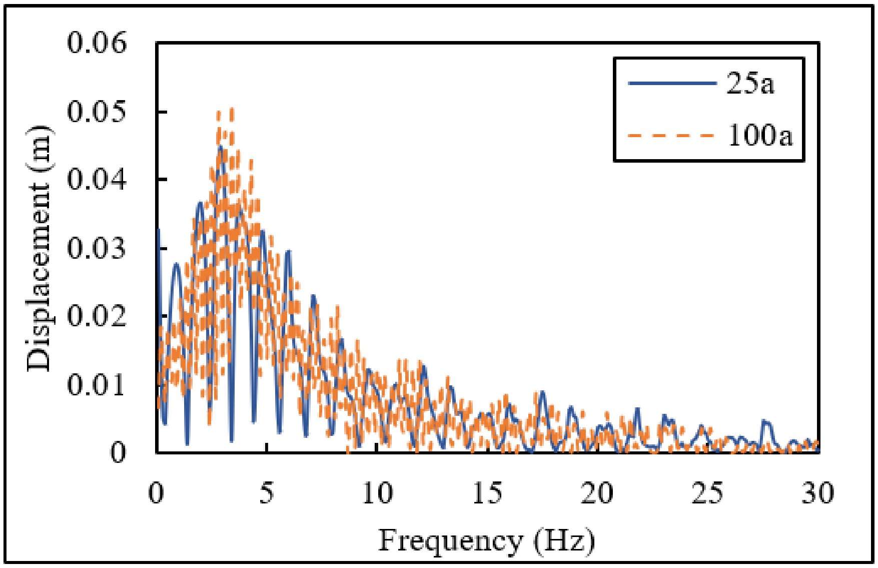

Figure B- 13: Displacement magnitude at the top of SDOF structure comparison between soil size of 25a versus 100a.

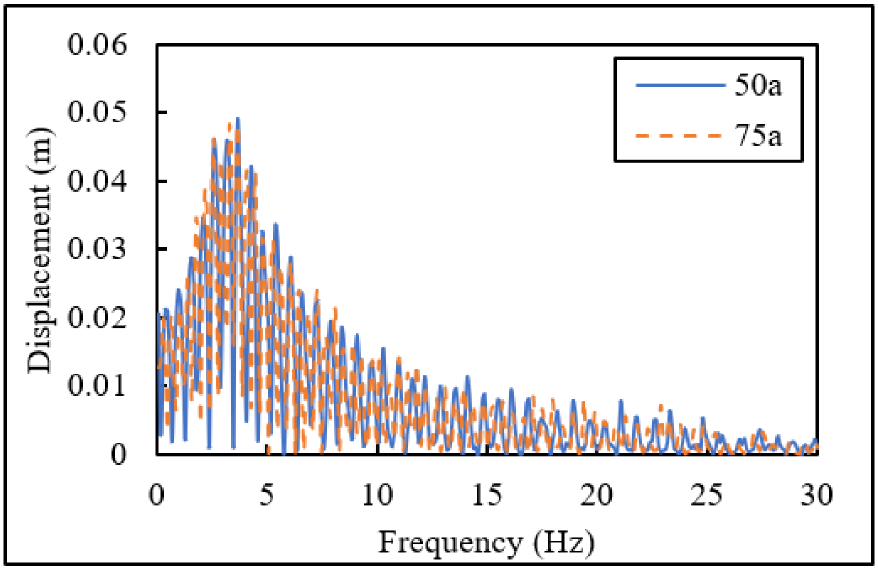

Figure B- 14: Displacement magnitude at the top of SDOF structure comparison between soil size of 50a versus 75a.

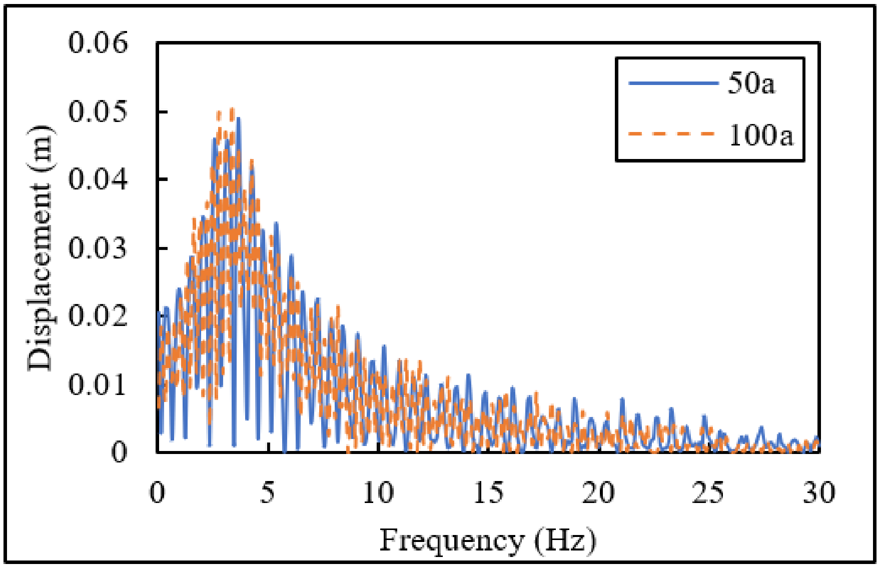

Figure B- 15: Displacement magnitude at the top of SDOF structure comparison between soil size of 50a versus 100a.

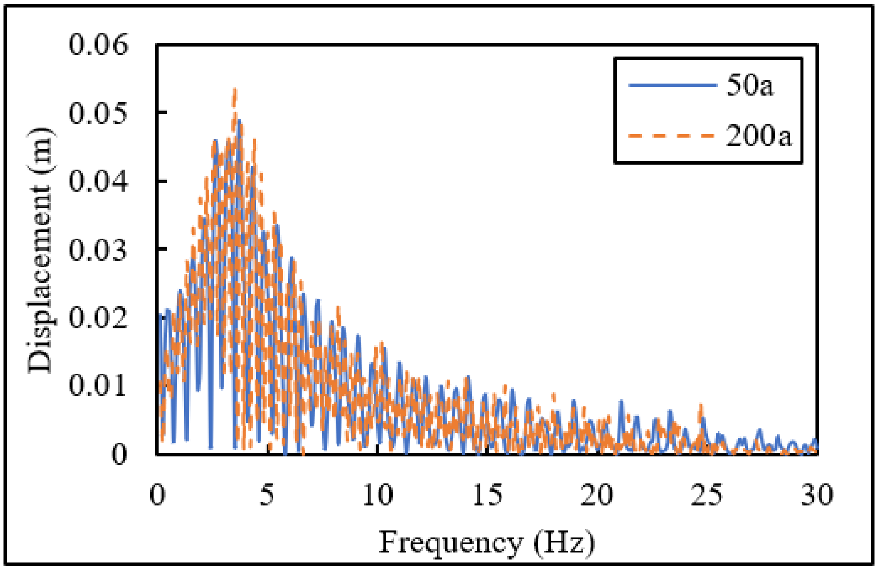

Figure B- 16: Displacement magnitude at the top of SDOF structure comparison between soil size of 50a versus 200a.

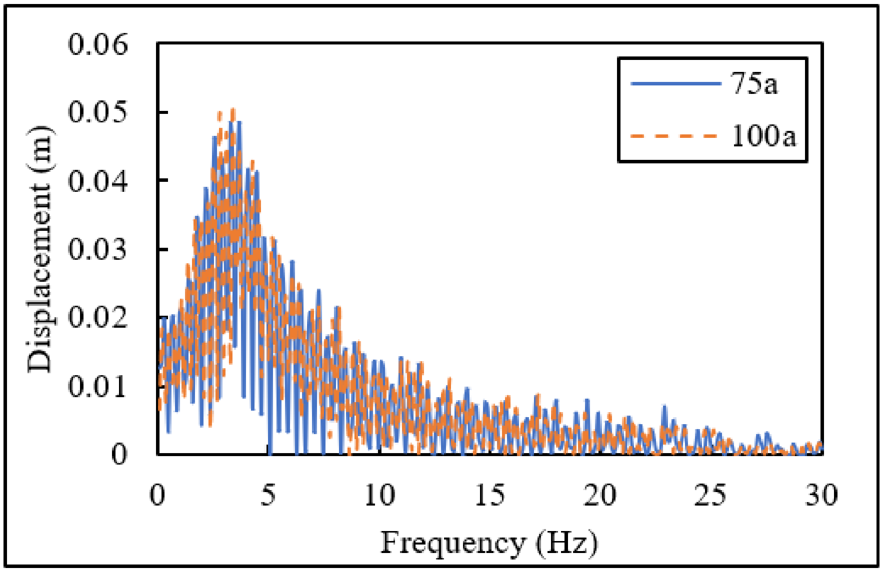

Figure B- 17: Displacement magnitude at the top of SDOF structure comparison between soil size of 75a versus 100a.

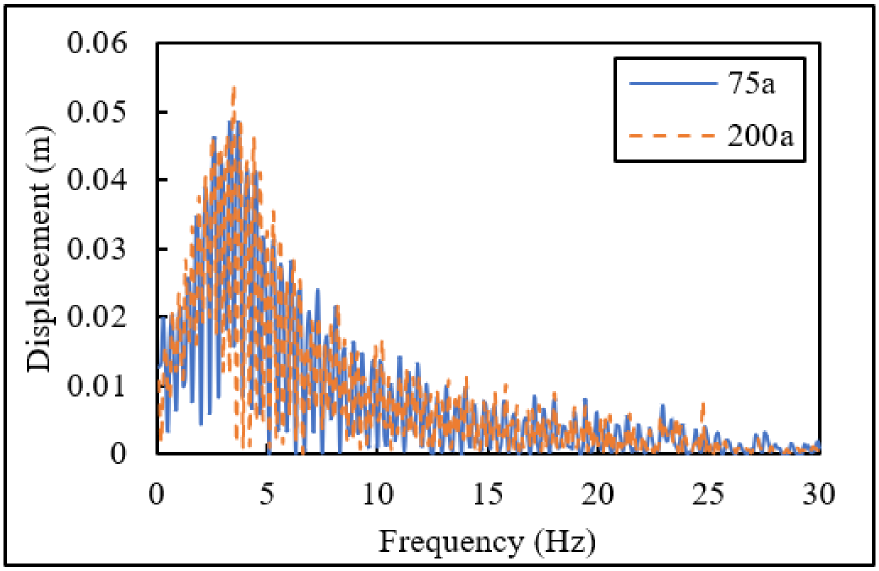

Figure B- 18: Displacement magnitude at the top of SDOF structure comparison between soil size of 75a versus 200a.

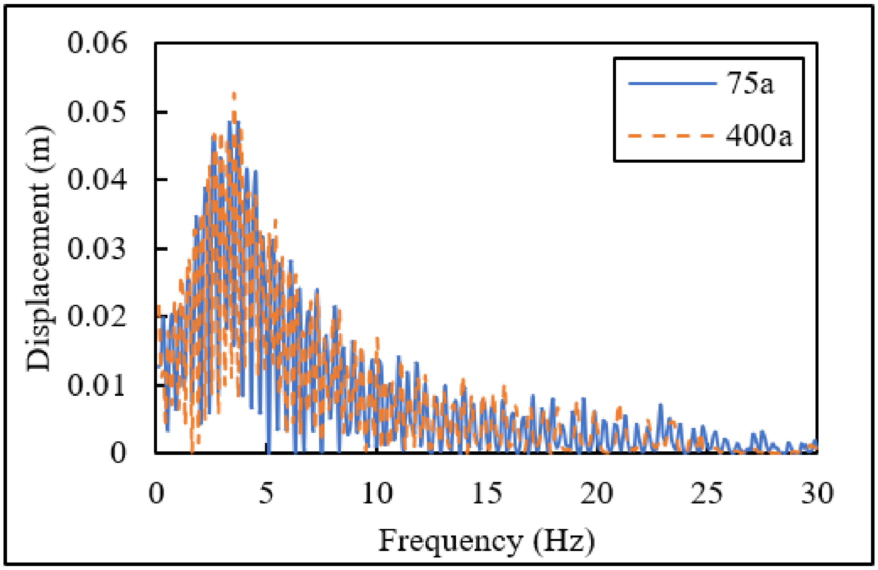

Figure B- 19: Displacement magnitude at the top of SDOF structure comparison between soil size of 75a versus 400a.

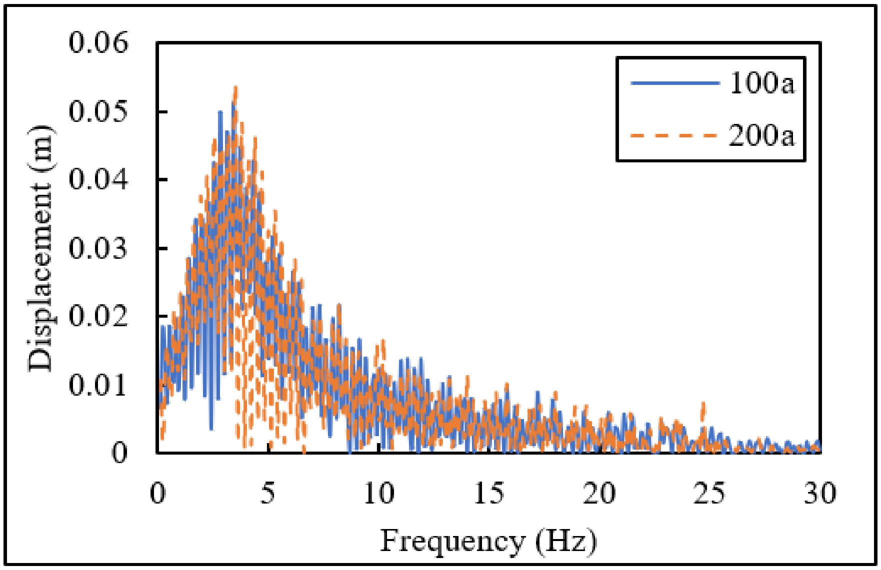

Figure B- 20: Displacement magnitude at the top of SDOF structure comparison between soil size of 100a versus 200a.

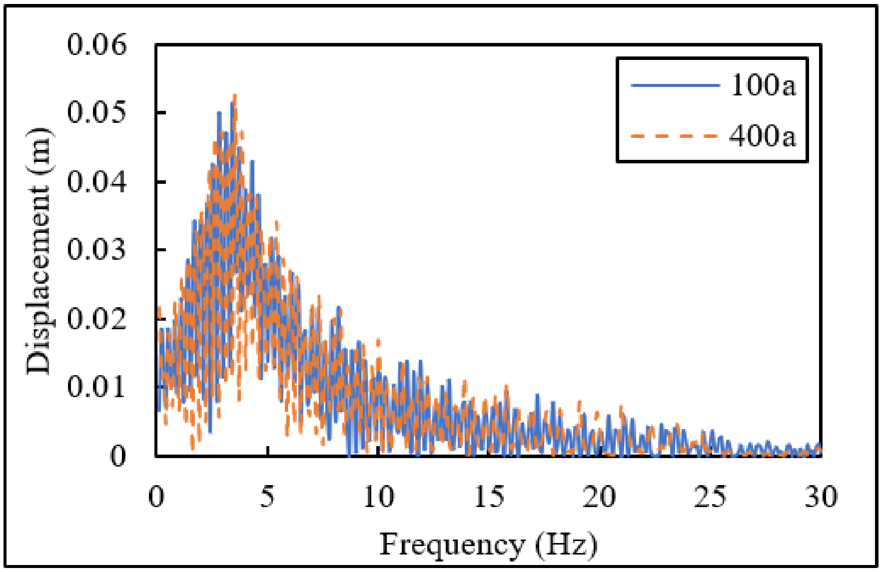

Figure B- 21: Displacement magnitude at the top of SDOF structure comparison between soil size of 100a versus 400a.

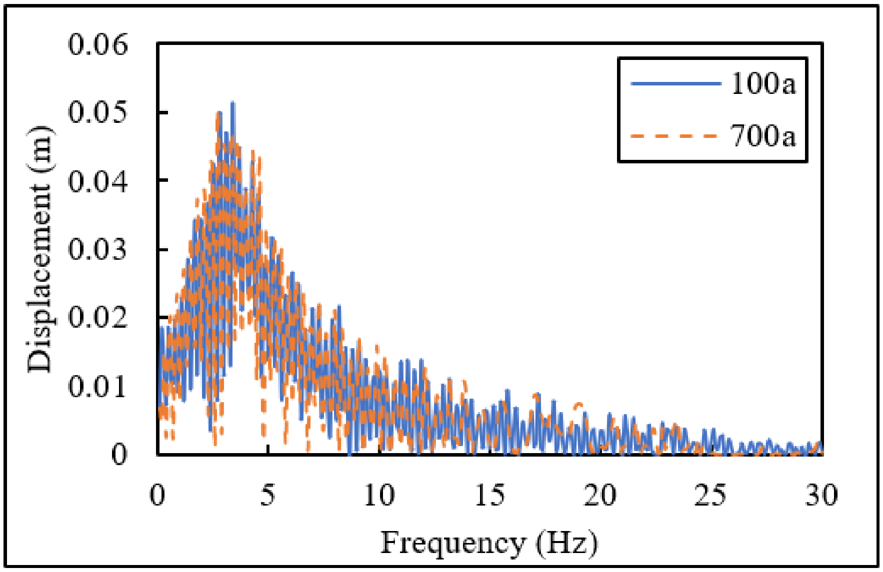

Figure B- 22: Displacement magnitude at the top of SDOF structure comparison between soil size of 100a versus 700a.

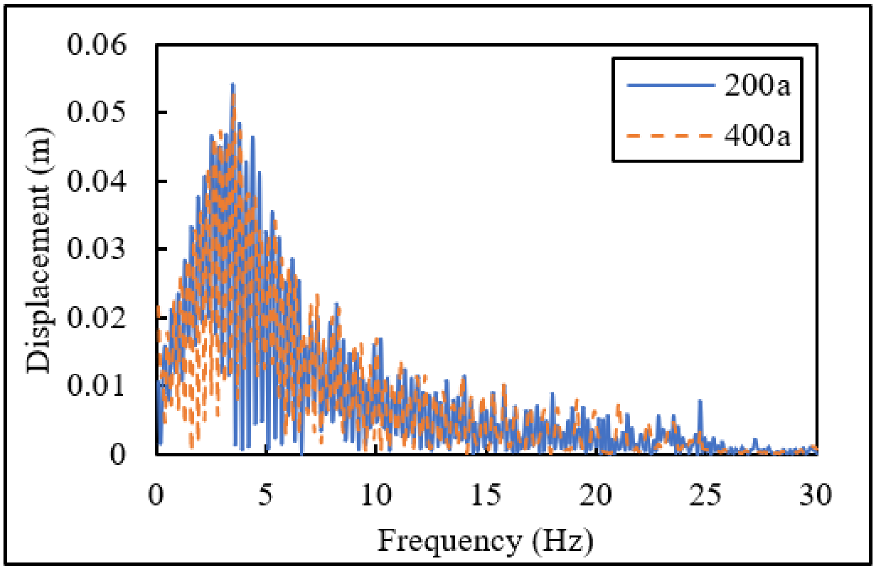

Figure B- 23: Displacement magnitude at the top of SDOF structure comparison between soil size of 200a versus 400a.

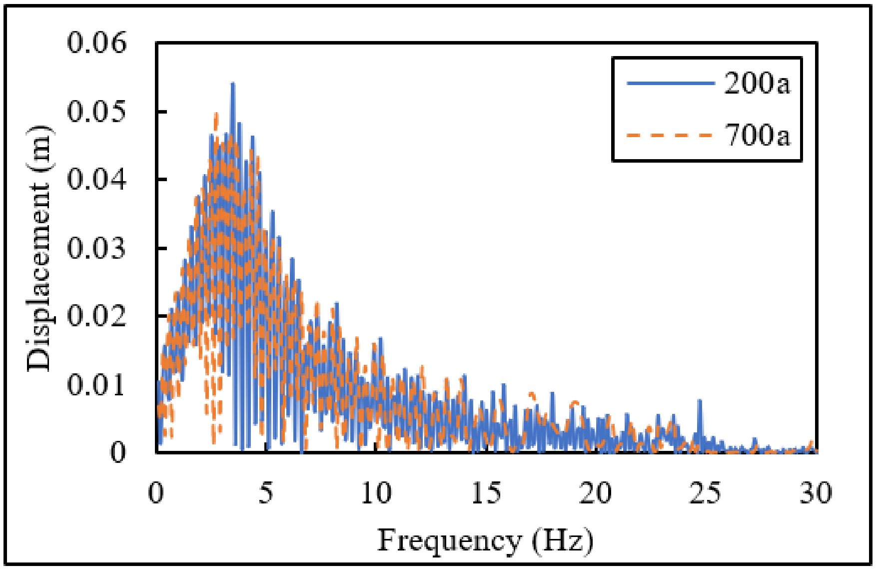

Figure B- 24: Displacement magnitude at the top of SDOF structure comparison between soil size of 200a versus 700a.

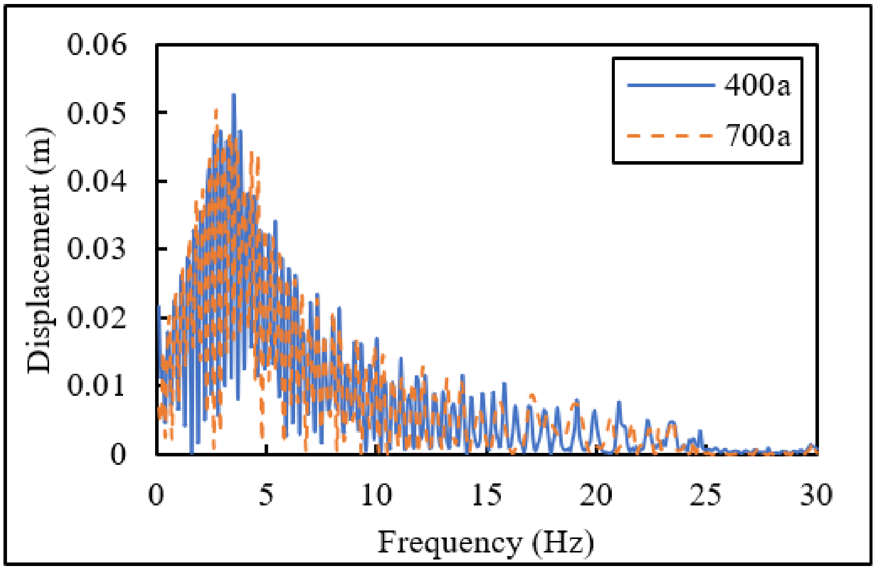

Figure B- 25: Displacement magnitude at the top of SDOF structure comparison between soil size of 400a versus 700a.